Department of Precision and Microsystems Engineering

Component Mode Synthesis for geometrically nonlinear structures

F. Wenneker

Report no	:	EM 2013.029
Coach	:	dr. ir. P. Tiso
Professor	:	prof. dr. ir. A. van Keulen
Specialisation	:	Engineering Mechanics
Type of report	:	MSc. thesis
Date	:	November 11, 2013

TU Delft Delft University of Technology

Abstract

In the field of computational physics and engineering, the introduction of computers opened a world of possibilities. The finite element (FE) method was developed in order to solve complex problems numerically. Over time, the method matured and structures in the field of engineering became more and more complex, resulting in large degree of freedom (DOF) systems. Finite element analyses on large systems can be a computationally heavy and expensive task, which led to the development of Component Mode Synthesis (CMS) techniques. These techniques generally consist of a combination of two other techniques: substructuring and Model Order Reduction (MOR). Substructuring is used to obtain the structural behaviour of large and/or complex structures by dividing them into several smaller and simpler substructures of which the structural behaviour is easier to determine. The global system is then obtained by assembly of the substructures. Using MOR, a full order model is approximated by a system of lower dimension by expressing the displacement field in terms of a set of reduced coordinates. In linear statics and dynamics problems, MOR is widely used. For nonlinear problems however, the same methods cannot be used.

The focus of this thesis is developing a Component Mode Synthesis technique that is able to accurately describe nonlinear dynamic responses of structures. A special type of nonlinearities is considered; geometrical nonlinearities. The internal force of a geometrically nonlinear problem may consist of linear and nonlinear contributions. The nonlinear terms are dependent on the deformed state of the model and couples the equations of motion. This makes the evaluation of nonlinear systems computationally expensive. Hence, a nonlinear CMS technique is highly welcomed.

Two reduction methods that are widely used in linear mechanics are the Craig-Bampton and Rubin method. Both techniques use sets of component modes, either static or dynamic modes, to approximate the full order displacement field. In this work, the methods are extended such that the reduced models will also be able to describe geometrical nonlinearities. This is done by adding additional component modes; modal derivatives (MDs). A modal derivative describes second-order nonlinear contributions of a vibration mode, when it is perturbed with the shape of another vibration mode. They can be systematically and cheaply computed once a reduction basis is formed for the linearised problem. Also, a criterion to select the most important MDs out of a set of linearised vibration modes is developed.

An efficient nonlinear time integration scheme, originally proposed by Bathe in [3], has been extended for the application to reduced models. This scheme condenses all degrees of freedom corresponding to linear elements in a finite element model prior to the expensive equilibrium equations that are required to solve nonlinear equations of motion.

The presented methods are tested on three small test problems to gain insight in the performance and limitations. It was found that both methods work as long as none of the substructures undergo large rotations. If large rotations are present, the extended Craig-Bampton method does not work due to the lack of component modes that describe this type of motion. The extended Rubin method worked in all cases, as rigid body modes and the corresponding MDs are present in the reduction basis. Also, a larger FE model of a Joined

Wing (JW) structure is analysed using the nonlinear CMS methods. This is a nonconventional airplane wing arrangement, showing promising aerodynamic characteristics that could positively impact the fuel consumption and the maneuverability of the aircraft. While maintaining an accurate model of the geometrically nonlinear dynamics, the number of degrees of freedom of the JW model was reduced from 2190 to 296 and 440 for the Craig-Bampton and Rubin methods, respectively. For a nonlinear response analysis on the JW model, the computation time is reduced by half to 15 min. Considering the smaller test models as well, time savings between 78% and 33% were obtained.

Several challenges still exist when using the presented nonlinear CMS technqiues. The Craig-Bampton method should be extended with additional modes that describe large rotations of substructures. Also, the number of modal derivatives that can be computed is quadratic with respect to the number of chosen linearised vibration modes and thus quickly making the dimension of the reduction basis large. A proper mode selection criterion should be developed, which can be used to select only the important MDs per substructure without introducing additional error.

Contents

Notation

Symbols

General meaning of often used symbols, unless otherwise stated in context:

b_{ij}	Mode selection coefficient of modes i and j
$\mathbf{B}$	Signed boolean matrix
$\mathbf{B}_L$	Linear strain matrix
$\mathbf{B}_{NL}$	Nonlinear strain matrix
$\mathbf{C}$	Damping matrix
D	Flexural rigidity
E	Young's modulus
$\mathbf{f}$	Internal force vector
$\mathbf{g}$	Connection or interface force vector
$\mathbf{G}$	Flexibility matrix
h	Thickness
$\mathbf{H}$	Hookean matrix
$\mathbf{K}$	(Linear) stiffness matrix
$\mathbf{L}$	Localisation matrix (boolean)
M	Number of vibration modes in reduction basis
$\mathbf{M}$	Mass matrix
$\mathbf{p}$	External load vector
P	Number of modal derivatives
$\mathbf{q}$	Modal displacement field
$\mathbf{r}$	Residual vector
R	Maximum number of modal derivatives
$\mathbf{R}$	Reduction basis
$\mathbf{S}$	Effective stiffness (or Jacobian) matrix
S_i	Substructure i
t	Time
$\mathbf{u}$	Physical displacement field

Greek symbols:

γ_k	Modal stiffness of mode k
η	Modal coordinate of vibration mode
$\boldsymbol{\theta}$	Modal derivative of modes i and j
$\boldsymbol{\Theta}$	Collection of modal derivatives
λ	Load factor
μ_k	Modal mass of mode k
ν	Possion's ratio
ξ	Modal coordinate of modal derivative
ρ	Density
$\boldsymbol{\Phi}$	Collection of vibration modes
$\boldsymbol{\phi}_k$	Vibration mode k
$\boldsymbol{\Psi}_c$	Collection of constraint modes
$\boldsymbol{\Psi}_r$	Collection of residual attachement modes
ω	Circular frequency or eigenfrequency
∇	Nabla operator

Subscripts and superscripts:

$(\bullet)_b$	Corresponding to boundary node	$(\bullet)^+$	Generalised inverse
$(\bullet)_i$	Corresponding to internal node	$\dot{(\bullet)}$	First time derivative
$(\bullet)^k$	Iteration k	$\ddot{(\bullet)}$	Second time derivative
$(\bullet)^{(k)}$	Component of substructure S_k	$\tilde{(\bullet)}$	Pertaining to reduced system
$(\bullet)_n$	Time step n	$\bar{(\bullet)}$	Pertaining to assembled system
$(\bullet)^{nl}$	Nonlinear component		

Abbreviations

Description of often used abbreviations in this thesis:

AM	Attachment mode	MD	Modal derivative
CB	Craig-Bampton	MOR	Model Order Reduction
CM	Constraint mode	NR	Newton-Raphson
CMD	Constraint modal derivative	RAM	Residual attachment mode
CMS	Component Mode Synthesis	RBM	Rigid body mode
DOF	Degree of freedom	RBD	Rigid body derivative
FE	Finite element	SVD	Singular value decomposition
FVM	Free vibration mode		
IVM	Internal vibration mode		

1 Introduction

1.1 Research context and motivation

Named after the co-founder of chipmaker Intel, Moore's law states that computer speed and memory capacity doubles every 18 months. Even though this prediction from 1965 has proven to be incredibly accurate, the need for computer speed and storage in engineering environments grows even faster. During the early development of procedures for evaluating the static and dynamic responses of structures, linear finite element (FE) models were used. The constantly increasing power and storage capabilities of computers made it possible to analyse more complicated systems, which in its turn led to the demand for faster computers and larger storage capacities.

The structural systems analysed in modern engineering are often required to be lighter, have a more complex geometry or operate at high speeds in order to enhance performance. With these design specifications, the structure's response may become nonlinear and nonlinear models need to be formulated in order to mathematically describe this response. The finite element method has the disadvantage that large, complex structures lead to models with a large amount of degrees of freedom (DOFs). The computational effort of an FE analysis is proportional to the cubic of the size of a problem [29]. Computational techniques that reduce the order of models thus greatly decrease storage and computation time. This is one of the motivations why Model Order Reduction (MOR) techniques are widely welcomed.

1.1.1 Model Order Reduction

A MOR technique uses a set of displacement shapes, also called *component modes*, to approximate the response of a structure. Computational savings are gained when this set of modes is considerably smaller than the set of physical DOFs of the FE model; the order of the system that needs to be solved will than be reduced greatly. Such techniques are widely used in linear analyses. Nonlinear systems impose difficulties which leads to insufficient performance of the usual MOR techniques (elaborated in chapter 4). With increasingly complex structures, the need for nonlinear finite element models also grows. For example, the rise of lightweight and highly deformable materials in aircraft and aerospace industry results in analyses that can no longer be done with the theory of linear elasticity. Nonlinearities need to be taken into account as well. However, nonlinear dynamic analysis is computationally heavy and therefore it is necessary to develop efficient methods to come up with the solution. This is the reason why MOR techniques for nonlinear systems is a research field that is gaining more and more interest.

1.1.2 Substructuring

Large and complex structures can often consist of distinguishable parts and can therefore be decomposed into an assemblage of relatively simple subsystems. Parts of complex structures may come from different contractors or design teams and may be built in different software packages. In such cases it is convenient to develop a dynamic model for the global structure by taking advantage of the dynamic properties of the substructures. In linear dynamics, a widely used technique is Component Mode Synthesis (CMS). With this technique, in literature also referred to as *dynamic substructuring*, a reduced order model of the global structure is formed by assembling the reduced models of the substructures.

In numerous cases of nonlinear systems having a large numbers of DOFs, the actual nonlinear components are spatially localised. For example, an airplane model could be modelled with a relatively stiff fuselage (linear) and more flexible wings (nonlinear). Applications of local nonlinearities are also present in the uprising world of microelectromechanical systems (MEMS), where capacitors of accelerometers are mounted on springs that are able to handle large deflection. A more close-by example can be found in sports: a tennis racket consists of a relatively stiff frame across which a network of highly deformable strings is spanned. In the FE modelling of such cases, CMS can be used to isolate the nonlinear components. Then, only the substructures containing nonlinear components need to be subjected to computationally heavy nonlinear analysis.

1.2 Thesis outline

In this thesis, two CMS techniques that are able to handle geometrical nonlinearities will be presented. Also, a time integration scheme will be modified such that only the nonlinear components of a reduced model are treated accordingly. The goal is to develop a CMS technique that is able to capture response of geometrically nonlinear systems in a time-efficient way without introducing significant errors.

The contents of the thesis may be divided into two parts: theory and application. The first starts with a brief introduction to geometrical nonlinearities (chapter 2), in which it is explained why nonlinear analyses are computationally more expensive. In chapter 3, the principles of Component Mode Synthesis are explained. This chapter summarises existing knowledge, that is extensively applied to linear dynamics problems. Chapter 4 presents two newly developed techniques that are suitable for geometrically nonlinear problems as well. In this chapter, the existing linear Craig-Bampton and Rubin reduction bases are augmented with additional component modes; modal derivatives. This enables the bases to capture second-order nonlinear effects. Methods to obtain dynamic responses of linear and nonlinear systems are elaborated in chapter 5. An efficient response analysis scheme for systems having only localised nonlinearities is also presented in this chapter. Next, all techniques are implemented in an FE environment in MATLAB. Prior to the application, the FE code is validated in chapter 6.

After the validation, the presented method are applied and tested on three relatively small test problems in section 7.1. This is done to gain insight in the advantages and possible drawbacks of the techniques. Finally in section 7.2, both methods are applied to a large FE model of a Joined Wing; a non-conventional airplane wing structure.

2 Introduction to geometrical nonlinearity

"To identify behavior as nonlinear is only to say what the behavior is not."

— Robert D. Cook in [6]

The main scope of this thesis is Component Mode Synthesis, or dynamic substructuring, for nonlinear systems. To narrow down the research scope, only geometric nonlinearities are considered. In this chapter, a brief introduction of this effect is given in order to give the reader a reasonable understanding.

Geometric nonlinearities are defined as the internal effects in a structure due to the changing geometry as it deflects. The stiffness of such a system is thus depending on the displacements, whereas the stiffness of a linear system is constant. In reality, nonlinear effects are always present, but often sufficiently small to ignore. Therefore most systems are classically considered to be geometrically linear. The assumption of linear kinematics leads to simplified equations of motion, which are depended on the undeformed configuration of the structure only. Linear kinematic assumptions limit the analysis to small displacements, rotations and strains. If these assumptions no longer hold, nonlinear analysis needs to be performed. For example, consider a plate or beam that is fully clamped on its boundaries and loaded with a uniform lateral pressure. If the out-of-plane deflection is more than about half the thickness, membrane stretching forces will be developed, which introduce a significant increase in stiffness. This means that in order to double the the deflection δ, the load p must be increased more than double:

$$p(2\delta) \neq 2p(\delta) \tag{2.1}$$

In finite element (FE) models, the engineer must therefore use an element that includes not only bending but also membrane stiffness. If only bending stiffness is included, the element is only usable for linear problems. As soon as nonlinear effects become important, this element will always over-estimate the actual deflection.

As a final remark, it is stressed that geometric nonlinearity does not explicitly means *large* deformations. It only means that the equilibrium equations are written in terms of the deformed geometry, which is not known in advance. Following [4], consider a rigid element of unit length that is rotated by an angle θ and hinged on one side as illustrated in fig. 2.1. Note that the beam in this example is only showing rigid body motion and thus no internal strains should exist during the motion. The displacements in x and y directions are:

$$u_x = X(\cos\theta - 1) - Y\sin\theta \qquad u_y = X\sin\theta + Y(\cos\theta - 1) \tag{2.2}$$

From these expressions, the linear (or infinitesimal) strain can be computed:

$$\varepsilon_x = \frac{\partial u_x}{\partial X} = \cos\theta - 1 \qquad \varepsilon_y = \frac{\partial u_y}{\partial Y} = \cos\theta - 1 \tag{2.3}$$

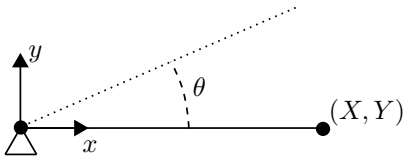

Figure 2.1: *Rigid element undergoing a rotation θ.*

Hence, if θ becomes large the linear strains do not vanish and thus a nonlinear strain description is needed for this type of problems. This example illustrates that geometrical nonlinearities also exist in the case of small (or no) strains combined with large rotations.

2.1 Equilibrium equations of geometrically nonlinear systems

For a FE model, the dynamic linear equilibrium equations are often written in a form that includes inertia, damping, stiffness forces and external loads:

$$\mathbf{M}\ddot{\mathbf{u}}(t) + \mathbf{C}\dot{\mathbf{u}}(t) + \mathbf{K}\mathbf{u}(t) = \mathbf{p}(t) \tag{2.4}$$

where the left hand side includes all internal forces. The system matrices in this expression, namely the mass $\mathbf{M}$, damping $\mathbf{C}$ and stiffness $\mathbf{K}$ matrices, depend on the undeformed state of the system. Hence, in a linear FE analysis the system matrices are formed during the element assembly process and then remain unchanged throughout the search for a solution. In nonlinear FE analysis, this is not the case (see eq. (2.1)). Due to the displacement dependent strain in a nonlinear FE element, the internal forces become a function of the deformation. The *geometric* nonlinear equations of motion are therefore written as

$$\mathbf{M}\ddot{\mathbf{u}}(t) + \mathbf{C}\dot{\mathbf{u}}(t) + \mathbf{f}(\mathbf{u}, t) = \mathbf{p}(t) \tag{2.5}$$

where $\mathbf{f}$ represents the internal elastic force vector, which is a function of the nodal displacements $\mathbf{u}$. For simplicity's sake, damping is considered to be displacement independent.

The shell element that is used in the FE models for this research are governed by von Kármán nonlinearities, meaning that the tangential stiffness matrix (i.e. the derivative of $\mathbf{f}$ with respect to the displacements $\mathbf{u}$) contains components that are either quadratic, linear or constant with respect to the displacements. The internal forces may therefore be split in a linear and a nonlinear component[1]:

$$\mathbf{f}(\mathbf{u}, t) = \mathbf{K}\mathbf{u}(t) + \mathbf{f}^{nl}(\mathbf{u}, t) \tag{2.6}$$

Decomposition as done in eq. (2.6) will prove useful in this research. This is because for systems where the nonlinearities are spatially localised, not all substructures contain the nonlinear force vector $\mathbf{f}^{nl}$. For the case where this nonlinear force is zero, we have $\mathbf{f} = \mathbf{K}\mathbf{u}$ and the nonlinear dynamic equilibrium in eq. (2.5) will be equal to that of a linear system (eq. (2.4)).

[1] Von Kármán nonlinearities and its effect on the internal forces, see eq. (2.6), do not hold in cases where the internal forces also depend on the load history, e.g. in plasticity problems. However, in general every nonlinear function f^{nl} can be decomposed in a linear (f^l) and nonlinear part ($f^{nl} - f^l$)

3 Component Mode Synthesis

In early design stages, static analyses on finite element models are performed in order to find stress concentrations in structures. These models often consist of very fine meshes and thus a large number of degrees of freedom (DOFs). Efficient solvers exist for static analysis. Using the same refined model for dynamic problems, such as computing vibration modes, harmonic and transient responses, results in unacceptably long computation times. For most dynamical problems such refined meshes are not needed and a coarser mesh would also suffice. However building two models of the same system, or remeshing the model, could be costly and takes up a significant amount of time. A method that reduces the size the dynamic problem without modifying the mesh would be very useful. Such methods are called *reduction methods* and similar to modal superposition, the full set of DOFs is approximated by a set of possible displacement shapes and corresponding amplitudes called the generalised DOFs:

$$\mathbf{u} \approx \mathbf{R}\mathbf{q} \tag{3.1}$$

For a system with n degrees of freedom, $\mathbf{R} \in \mathbb{R}^{n \times m}$, $m < n$. An efficient reduction would mean $m \ll n$. *Component Mode Synthesis* (CMS) extends this idea to systems consisting of multiple substructures. Generally, this technique involves four major steps as illustrated in fig. 3.1. First, a large model is divided into multiple components or substructures. Then the finite element method or a similar scheme is utilised in order to form discretizated components. Reduction similar to eq. (3.1) is applied to the substructures, such that the resulting set of DOFs now consists of a mixture between physical and generalised DOFs (only the internal DOFs are reduced). Finally, the global model is obtained by assembling the smaller substructures. The reduction of substructures is elaborated in section 3.1 and the assembly process is described more thoroughly in section 3.6. The first two steps in fig. 3.1 will not be discussed in this thesis; the division of substructures is a purely geometric operation and for FE discretisation the reader is referred to [15]. Due to the reduction step, this assembled model will be smaller in size than the global model directly obtained from the FE discretisation. All computations

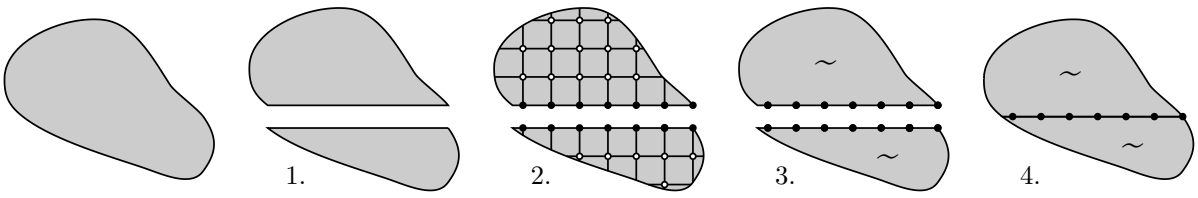

Figure 3.1: *Four major steps of the Component Mode Synthesis process on a random model: (1) substructuring, (2) discretisation, (3) reduction and (4) assembly.*

are performed on the reduced model and the obtained responses may be transformed back to the physical domain by use of eq. (3.1).

This approach has several advantages:

1. Large problems can be divided into several small problems; computer effort and storage can be significantly reduced.

2. In the context of large projects (e.g. spacecraft design), different design groups and/or contractors are able to work on on different substructures, at different places and on different times.

3. In case of a local design change, only the corresponding subsystem needs to be modified. When a structure contains a repeating pattern of components, e.g. the wings of an airplane, the model of one can be used for the remaining identical parts. This all saves valuable computation time.

4. The method allows implementation of *hybrid modelling*, where numerical models are combined with experimental setups.

Many CMS techniques exist and a review of them is given in [9]. A technique may be classified as a fixed-interface or free-interface method, depending upon whether the generalised coordinates are obtained with boundary DOFs fixed or free. A combination between the two is also possible. Hurty was the first to develop a fixed-interface method [20, 19]. Later, Craig and Bampton simplified this method [8]. Nowadays the Craig-Bampton method and its refinements, e.g. [31], are widely used because the procedure is straightforward and typically produces accurate models with few component modes. Other popular methods are developed by Rubin [33] and MacNeal [26]. For an extensive overview of the most popular model reduction methods, see [38, Ch.2]. In this research, both the Craig-Bampton (fixed-interface) and Rubin (free-interface) method are extended for geometrically nonlinear problems.

3.1 Reduction methods in general

In order to explain the principles of Component Mode Synthesis let us assume a finite element model defined on a domain Ω, which is divided into N_s non-overlapping substructures that each span a subdomain $\Omega^{(s)}$. The undamped equations of motion of each component, derived from eqs. (2.5) and (2.6), can be written as

$$\mathbf{M}^{(s)}\ddot{\mathbf{u}}^{(s)}(t) + \mathbf{K}^{(s)}\mathbf{u}^{(s)}(t) + \mathbf{f}^{nl(s)}(\mathbf{u}^{(s)}(t)) = \mathbf{p}^{(s)}(t) + \mathbf{g}^{(s)}(t) \qquad \text{for } s = 1, \ldots, N_s \tag{3.2}$$

where the superscript $^{(s)}$ is the label of the particular substructure[1]. Externally applied forces are represented by $\mathbf{p}^{(s)}$ and connecting forces from neighbouring substructures by $\mathbf{g}^{(s)}$.

The reduction method applied in this research involves transforming the physical coordinates into a (smaller) set of generalised coordinates. For a system having n degrees of freedom, eq. (3.2) can be reduced by substitution of eq. (3.1):

$$\mathbf{M}^{(s)}\mathbf{R}^{(s)}\ddot{\mathbf{q}}^{(s)} + \mathbf{K}^{(s)}\mathbf{R}^{(s)}\mathbf{q}^{(s)} + \mathbf{f}^{nl(s)} = \mathbf{p}^{(s)} + \mathbf{g}^{(s)} + \mathbf{r}^{(s)} \tag{3.3}$$

[1] From here on, time dependence will be omitted in notation, e.g. $\mathbf{u}(t) = \mathbf{u}$.

where $\mathbf{r}$ is the error or residual load due to the approximation in eq. (3.1). This residual represents the part of the equation that lies outside the subspace spanned by the reduction basis. Hence, the inner product of $\mathbf{r}$ with *any* set of vectors that span the subspace of $\mathbf{R}$ will be zero. In mechanical terminology, this states that $\mathbf{r}$ produces no work on the subspace of $\mathbf{R}$, i.e. $\mathbf{R}^T\mathbf{r} = \mathbf{0}$. Premultiplying eq. (3.3) with $\mathbf{R}^T$ leads to the reduced equations of motion:

$$\tilde{\mathbf{M}}^{(s)}\ddot{\mathbf{q}}^{(s)} + \tilde{\mathbf{K}}^{(s)}\mathbf{q}^{(s)} + \tilde{\mathbf{f}}^{nl(s)} = \tilde{\mathbf{p}}^{(s)} + \tilde{\mathbf{g}}^{(s)} \tag{3.4}$$

where

$$\begin{gathered}\tilde{\mathbf{M}}^{(s)} = {\mathbf{R}^{(s)}}^T\mathbf{M}^{(s)}\mathbf{R}^{(s)}, \qquad \tilde{\mathbf{K}}^{(s)} = {\mathbf{R}^{(s)}}^T\mathbf{K}^{(s)}\mathbf{R}^{(s)}, \qquad \tilde{\mathbf{f}}^{nl(s)} = {\mathbf{R}^{(s)}}^T\mathbf{f}^{nl(s)} \\ \tilde{\mathbf{p}}^{(s)} = {\mathbf{R}^{(s)}}^T\mathbf{p}^{(s)}, \qquad \tilde{\mathbf{g}}^{(s)} = {\mathbf{R}^{(s)}}^T\mathbf{g}^{(s)}\end{gathered} \tag{3.5}$$

The principle discussed here is also known as *reduction by projection*. The substructure labels will be discarded in the rest of the chapter unless they are needed in order to avoid confusion, e.g. $\mathbf{M}^{(s)} = \mathbf{M}$. Also the reduced matrices as in eq. (3.4) will be denoted without a tilde to minimise notational clutter. To avoid confusion it will be explicitly mentioned when the full matrix is considered, which may also be seen by the fact that it operates on $\mathbf{u}$ instead of $\mathbf{q}$.

3.1.1 Reduction basis

The reduction basis $\mathbf{R}$ is an operator transforming a set of physical DOFs into a set of generalised DOFs, see eq. (3.1). However, coupling of substructures using the generalised coordinates $\mathbf{q}$ is a rather difficult task and is generally never done in CMS procedures. Instead, the DOFs on the substructure boundaries are not reduced. Distinguishing boundary and internal DOFs lead to the following form of the generalised coordinates $\mathbf{q}$ and the connecting forces $\mathbf{g}$:

$$\mathbf{q} = \begin{bmatrix}\mathbf{q}_b \\ \mathbf{q}_i\end{bmatrix}, \qquad \mathbf{g} = \begin{bmatrix}\mathbf{g}_b \\ \mathbf{0}\end{bmatrix} \tag{3.6}$$

where generally we have $\mathbf{q}_b = \mathbf{u}_b$. The reduction basis thus operates on all DOFs, but only the internal physical ones $\mathbf{u}_i$ are reduced to a generalised set $\mathbf{q}_i$. A reduction basis consists of *component modes* that cause this transformation. Two types of components modes are generally present in a reduction basis: *dynamic modes* and *static modes*. The first accounts for the dynamic behaviour of the substructure, whereas the latter is used to represent the interaction with neighbouring substructures. Generally, we can write:

$$\mathbf{u}_i = \mathbf{u}_{i,stat} + \mathbf{u}_{i,dyn} \tag{3.7}$$

The following two sections will describe respectively the static and dynamic component modes used in present research.

3.2 Static component modes

The static contribution in eq. (3.7) comes from the inclusion of static component modes in the reduction basis. This essential mode type accounts for the interaction between neighbouring substructures and ensures that compatibility conditions after assembly are met (see section 3.6). Static modes also ensure that the model response is statically correct. The number of static

(a) *Constraint mode*

(b) *Residual attachment mode*

Figure 3.2: *Two types of static component modes. The undeformed geometry is shown with dashed lines and boundary nodes, in undeformed state, are indicated by black dots.*

modes in the reduction basis is equal to the number of boundary DOFs; no reduction is obtainable with these modes[2]. In the next sections two types of static component modes are described, namely *constraint modes* and *(residual) attachment modes*. An impression of these modes for a square plate is given in fig. 3.2.

3.2.1 Constraint modes

Constraint modes (CMs) represent the static deformation caused by neighbouring substructures. They are defined as a unit displacement on one boundary DOF with all other boundary DOFs fixed. Since this is a static mode type, the derivation will start with the linear static equilibrium obtained when neglecting dynamic effects in eq. (2.4):

$$\mathbf{K}\mathbf{u} = \mathbf{p} + \mathbf{g} \tag{3.8}$$

This system of equations can be partitioned by distinguishing boundary DOFs $\mathbf{u}_b$ and internal DOFs $\mathbf{u}_i$. By assuming no forces act on the internal DOFs, we can write

$$\begin{bmatrix} \mathbf{K}_{bb} & \mathbf{K}_{bi} \\ \mathbf{K}_{ib} & \mathbf{K}_{ii} \end{bmatrix} \begin{bmatrix} \mathbf{u}_b \\ \mathbf{u}_i \end{bmatrix} = \begin{bmatrix} \mathbf{p}_b \\ \mathbf{0} \end{bmatrix} + \begin{bmatrix} \mathbf{g}_b \\ \mathbf{0} \end{bmatrix} \tag{3.9}$$

In order to determine how the internal DOFs displace due to displacements of the boundary DOFs, one can statically condense the internal DOF set onto the boundary:

$$\mathbf{u}_i = -\mathbf{K}_{ii}^{-1}\mathbf{K}_{ib}\mathbf{u}_b \tag{3.10}$$

where $\mathbf{K}_{ii}$ is assumed to be non-singular. The term $\mathbf{K}_{ii}^{-1}$ may be interpreted as the flexibility (inverse stiffness) of the internal DOFs. This term acts on $\mathbf{K}_{ib}\mathbf{u}_b$, which represents the internal force in $\mathbf{u}_i$ coming from displacements in $\mathbf{u}_b$. The entire right-hand side of eq. (3.10) therefore represents a displacement of the internal DOFs due to the boundary DOFs, also called *attached displacement*. Combining this with the unit displacements on the boundary DOFs, one can write:

$$\mathbf{u} = \begin{bmatrix} \mathbf{u}_b \\ \mathbf{u}_i \end{bmatrix} = \begin{bmatrix} \mathbf{I} \\ -\mathbf{K}_{ii}^{-1}\mathbf{K}_{ib} \end{bmatrix} \mathbf{u}_b = \mathbf{\Psi}_c \mathbf{u}_b \tag{3.11}$$

[2] Interface reduction methods exist [32, 38], but are not treated within the scope of this research.

where the columns of $\mathbf{\Psi}_c$ contain the individual CMs. The number of CMs is equal to the amount of boundary DOFs. Physically, every ith column of $\mathbf{\Psi}_c$ can be interpreted as the static displacement of the structure when the ith boundary DOF has unit displacement, while all other boundary DOFs have zeros displacement. A typical CM is illustrated in fig. 3.2a.

Corresponding to the derivation of the CMs, a few remarks can be made:

- The fundamental equation for computing CMs is the static equilibrium in eq. (3.8). Due to the linear nature of this equilibrium, CMs are only able to accurately describe the linear static response of structures. Nonlinear effects are not taken into account in the derivation and therefore CMs will not be able to describe nonlinear interface behaviour.
- The condensation technique of eliminating unwanted DOFs for the system of equations, see eq. (3.10), was originally proposed by Guyan [18] and Irons [23] in 1965. Because dynamic effects are ignored it is often referred to as *static condensation*, but also *Guyan reduction* is a common name.

3.2.2 Attachment and residual attachment modes

Whereas constraint modes are defined by specifying a unit displacement at one boundary DOF while fixing the others, attachment modes (AMs) are defined by specifying a unit force at one boundary DOF while letting the others free (as shown in fig. 3.2b). Therefore, AMs are easily obtained from experiments. As will follow from this section, AMs are hardly used in numerical CMS methods due to the more advantageous properties of *residual* attachment modes (RAMs). However, in order to compute the latter, AMs are needed first. Attachment modes are defined by

$$\mathbf{\Psi}_a = \mathbf{K}^{+}\mathbf{F} = \mathbf{G}\mathbf{F} \tag{3.12}$$

where the columns of matrix $\mathbf{\Psi}_a$ contain individual AMs and $\mathbf{K}^{+}$ denotes the generalised or pseudo-inverse of the stiffness matrix, which is by definition the flexibility matrix $\mathbf{G}$. The columns of $\mathbf{F}$ impose a unit force on one boundary DOF:

$$\mathbf{F} = \begin{bmatrix} \mathbf{I} & \mathbf{0} \end{bmatrix}^T \tag{3.13}$$

where $\mathbf{I}$ is the identity matrix acting on $\mathbf{u}_b$ and $\mathbf{0}$ the null-matrix acting on $\mathbf{u}_i$. If the considered substructure is fully constrained by globally imposed boundary conditions, we have $\mathbf{K}^{+} = \mathbf{K}^{-1} = \mathbf{G}$ and the AMs are straightforwardly obtained from eq. (3.12). In the general case where the substructure is not fully constrained, the stiffness matrix is singular and a special procedure is needed to compute the attachment modes:

1. First, the generalised inverse of the singular $\mathbf{K}$ needs to be determined. This is done by imposing imaginary constraints, also called isostatic constraints or temporary links, on some DOFs $\mathbf{u}_c$. A scheme for computing the optimal set $\mathbf{u}_c$ is described in [37]. It is important that the resulting reaction forces coming from the imposed constraints are minimised, as this gives the best estimate for the system's static deformation due to unit boundary forces. By fixing $\mathbf{u}_c$ and letting the remaining $\mathbf{u}_r$ free, we obtain

$$\mathbf{K}^{+} = \begin{bmatrix} \mathbf{0} & \mathbf{0} \\ \mathbf{0} & \mathbf{K}_{rr}^{-1} \end{bmatrix} = \begin{bmatrix} \mathbf{0} & \mathbf{0} \\ \mathbf{0} & \mathbf{G}_{rr} \end{bmatrix} = \mathbf{G}_c \tag{3.14}$$

   where $\mathbf{G}_c$ is the constrained flexibility matrix.

2. The second step is to find a set of self-equilibrating forces $\mathbf{F}_{eq}$, needed to prevent the system from undergoing infinite accelerations and undetermined deformations. These forces can be interpreted as reaction forces keeping the body in places when subjected to unit boundary loads. The process of applying a self-equilibrating force to a system is called *inertia-relief* [11]. The self-equilibrating force is found by equilibrating the d'Alembert inertia forces ($-\mathbf{M}\ddot{\mathbf{u}}_r$) with the force vector in eq. (3.13). Using the mode superposition principle, we can write

$$\mathbf{F}_{eq} = \mathbf{F} - \mathbf{M}\boldsymbol{\Phi}_r\ddot{\boldsymbol{\eta}}_r \tag{3.15}$$

where the rigid body modes[3] are denoted by the subscripts r. In order to find the second term in the right-hand side of eq. (3.15), the mode superposition principle is used. The system's response $\mathbf{u}$ can be separated in a rigid and a flexible body response:

$$\mathbf{u} = \mathbf{u}_r + \mathbf{u}_f = \boldsymbol{\Phi}_r\boldsymbol{\eta}_r + \boldsymbol{\Phi}_f\boldsymbol{\eta}_f \tag{3.16}$$

Substituting this in the equations of motion in eq. (2.5) gives

$$\mathbf{M}\boldsymbol{\Phi}_r\ddot{\boldsymbol{\eta}}_r + \mathbf{M}\boldsymbol{\Phi}_f\ddot{\boldsymbol{\eta}}_f + \mathbf{f}(\boldsymbol{\Phi}_r\boldsymbol{\eta}_r) + \mathbf{f}(\boldsymbol{\Phi}_f\boldsymbol{\eta}_f) = \mathbf{F} \tag{3.17}$$

Exploiting the mode orthogonality principle and the fact that rigid body motion does not introduce any deformation and thus no internal elastic forces, we can premultiply the expression above by $\boldsymbol{\Phi}_r^T$:

$$\boldsymbol{\Phi}_r^T\mathbf{M}\boldsymbol{\Phi}_r\ddot{\boldsymbol{\eta}}_r = \boldsymbol{\Phi}_r^T\mathbf{F} \tag{3.18}$$

Solving for $\ddot{\boldsymbol{\eta}}_r$ and substituting into eq. (3.15) results in the following expression for the self-equilibrating force:

$$\mathbf{F}_{eq} = \left(\mathbf{I} - \mathbf{M}\boldsymbol{\Phi}_r\left(\boldsymbol{\Phi}_r^T\mathbf{M}\boldsymbol{\Phi}_r\right)^{-1}\boldsymbol{\Phi}_r^T\right)\mathbf{F} = \mathbf{P}\mathbf{F} \tag{3.19}$$

where $\mathbf{P}$ is a projection matrix with the property of self-equilibrating any force vector that is projected on it. In eq. (3.19), the matrix projects the original force vector onto a space outside the space of the rigid body modes such that these modes are not excited by the obtained force $\mathbf{F}_{eq}$. By replacing the force vector in eq. (3.12), a solution for the attachment modes can be found:

$$\tilde{\boldsymbol{\Psi}}_a = \mathbf{K}^+\mathbf{F}_{eq} = \mathbf{G}_c\mathbf{F}_{eq} \tag{3.20}$$

3. To ensure that the AMs eq. (3.20) do not contain any rigid body contributions and only describe a static deformation, the last step that is required to obtain the attachment modes is to mass-orthogonalise $\tilde{\boldsymbol{\Psi}}_a$ with respect to the rigid body modes. By its definition, this is done by premultiplying the AMs with $\mathbf{P}^T$:

$$\boldsymbol{\Psi}_a = \mathbf{P}^T\tilde{\boldsymbol{\Psi}}_a = \mathbf{P}^T\mathbf{G}_c\mathbf{P}\mathbf{F} = \mathbf{G}_f\mathbf{F} \tag{3.21}$$

where $\mathbf{G}_f$ denotes the elastic flexibility matrix.

[3] Rigid body modes are elaborated in section 3.3.3.

Residual attachment modes

From eqs. (3.13) and (3.21) it follows that the columns of the elastic flexibility matrix store the attachment modes. For an unconstrained system having n DOFs and n_r rigid body modes, the spectral expansion of $\mathbf{G}_f$ is written as [16]:

$$\mathbf{G}_f = \sum_{j=n_r+1}^{n} \frac{\boldsymbol{\phi}_{f,j}\boldsymbol{\phi}_{f,j}^T}{\omega_{f,j}^2} \tag{3.22}$$

In numerical free-interface CMS methods, where the static response of the reduced DOFs is determined by attachment modes instead of the constraint modes discussed in section 3.2.1, the (linear) dynamic response is approximated by free vibration modes $\boldsymbol{\phi}_{f,j}$ (see section 3.3.1). However, from the spectral expansion in eq. (3.22) it can be seen that the flexibility of the free vibration modes will then be accounted for twice. This is disadvantageous for convergence reasons. Therefore, *residual attachment modes* (RAMs) are introduced, defined by the columns of the residual flexibility matrix $\mathbf{G}_r$:

$$\mathbf{G}_r = \mathbf{G}_f - \sum_{j=n_r+1}^{n_f} \frac{\boldsymbol{\phi}_{f,j}\boldsymbol{\phi}_{f,j}^T}{\omega_{f,j}^2} \tag{3.23}$$

where n_f denotes the number of included free vibration modes in the reduction basis. Hence, $\mathbf{G}_r$ stores flexibility information on the $n_d = n - n_f$ discarded modes only. As a final remark it should be noted that RAMs can only be calculated after the number of n_f free vibration modes are computed. In practice, first the attachment modes are computed. Once the vibration modes are computed, the RAMs are obtained from eq. (3.23).

3.3 Dynamic component modes

Next the to static contribution, the dynamic contribution to the displacements in eq. (3.7) is accounted for by dynamic component modes. The actual order reduction is achieved with these type of modes. The response of a system having n DOFs may be represented exact by the sum of all vibration modes with a certain modal amplitude:

$$\mathbf{u}(t) = \sum_{k=1}^{n} \eta_k \boldsymbol{\phi}_k(t) \tag{3.24}$$

However, the fundamental dynamic behaviour of a system is often dominated only by a limited number of modes m. Hence, by applying *modal truncation* the displacements can be approximated as

$$\mathbf{u}(t) \approx \sum_{k=1}^{m} \eta_k \boldsymbol{\phi}_k(t) \qquad\qquad m \ll n \tag{3.25}$$

By only including $m \ll n$ modes in the reduction basis, the physical set of DOFs $\mathbf{u}$ can be approximated accurately by $\mathbf{q}$ according to eq. (3.1). Similar to the static modes, different types of dynamic component modes exist. As illustrated in fig. 3.3, the next sections will describe three commonly used vibration modes; free vibration modes, internal vibration modes and rigid body modes.

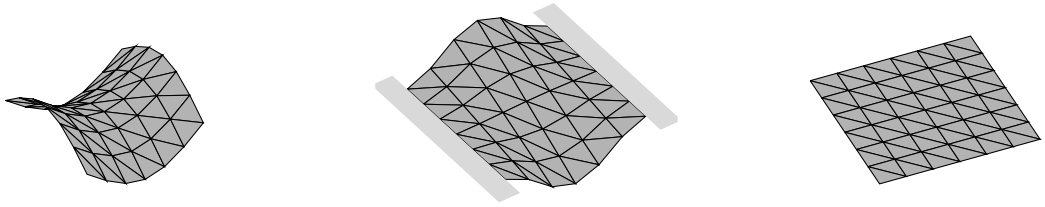

(a) *Free vibration mode* **(b)** *Internal vibration mode* **(c)** *Rigid body mode*

Figure 3.3: *Three types of vibration component modes*

3.3.1 Free vibration modes

Free vibration modes (FVMs) are used in so-called CMS methods. These are the vibration modes of the free floating structure, without rigid body modes which will be present due to this property. Recall the linear, undamped, free vibration problem[4]:

$$\mathbf{M}\ddot{\mathbf{u}} + \mathbf{K}\mathbf{u} = \mathbf{0} \tag{3.26}$$

The classical eigenvalue problem corresponding to this expression is

$$\left(\mathbf{K} - \omega_{f,j}^2 \mathbf{M}\right) \boldsymbol{\phi}_{f,j} = \mathbf{0} \tag{3.27}$$

where $\omega_{f,j}$ is the jth eigenfrequency and $\boldsymbol{\phi}_{f,j}$ its associated (free) eigenmode. All computed FVMs may be stored in columns of matrix $\boldsymbol{\Phi}_f$.

Free vibration modes act on both internal and boundary degrees of freedom. In order to retain the physical boundary DOFs, a second coordinate transformation is needed when these modes are included in the reduction basis. This is done in the Rubin reduction method described in section 3.5. An impression of a free vibration mode is given in fig. 3.3a.

3.3.2 Internal vibration modes

The interpretation and derivation of internal vibration modes (IVMs), also called *fixed interface modes*, is similar to that of FVMs (section 3.3.1). IVMs can be seen as the vibration modes when the system's boundary DOFs are fixed. These modes are found by solving the eigenvalue problem of the substructure fixed on its boundary, i.e. $\mathbf{q}_b = \mathbf{0}$. Analogue to eq. (3.27), this writes:

$$\left(\mathbf{K}_{ii} - \omega_{i,j}^2 \mathbf{M}_{ii}\right) \boldsymbol{\phi}_{i,j} = \mathbf{0} \tag{3.28}$$

where $\omega_{i,j}$ is the jth eigenfrequency and $\boldsymbol{\phi}_{i,j}$ its associated (fixed) eigenmode. Again, the order reduction is achieved by including only $m \ll n$ internal vibration modes in the reduction basis. The modes are stored in matrix $\boldsymbol{\Phi}_i$

[4]For the derivation of FVMs, boundary and internal DOFs need not be separated.

As opposed to the free vibration modes presented in section 3.3.1, internal vibration mode do not act on the boundary DOFs. Therefore no second coordinate reduction is required for a reduction basis including these modes, since we have $\mathbf{u}_b = \mathbf{0}$:

$$\mathbf{u} = \begin{bmatrix} \mathbf{u}_b \\ \mathbf{u}_i \end{bmatrix} = \begin{bmatrix} \mathbf{0} \\ \mathbf{\Phi}_i \end{bmatrix} \begin{bmatrix} \mathbf{u}_b \\ \boldsymbol{\eta}_i \end{bmatrix} \tag{3.29}$$

where $\boldsymbol{\eta}_i$ represents the modal amplitudes corresponding to the modeshapes in $\mathbf{\Phi}_i$. An internal vibration mode is illustrated in fig. 3.3b.

3.3.3 Rigid body modes

A body in space that is not fully constrained is able to displace without causing internal deformations, i.e. no internal elastic forces:

$$\mathbf{K}\mathbf{\Phi}_r = \mathbf{0} \tag{3.30}$$

These displacements are called rigid body modes (RBMs), or zero energy modes. The columns of $\mathbf{\Phi}_r$ contain individual RBMs denoted by $\boldsymbol{\phi}_r$. A body in three-dimensional space contains at most six rigid body modes: three rotations and three translations[5]. An illustration of a rigid body mode is given in fig. 3.3c.

From eq. (3.30) it follows that the rigid body modes represent the nullspace of the stiffness matrix. However, computing the nullspace of a generally large matrix is inefficient. A better and more convenient way would be to use an eigensolver to compute the free-floating problem in eq. (3.27) and subtract the RBMs from the obtained free-interface vibration modes. However, this is still inefficient and therefore RBMs are mostly computed geometrically ([14, 17]). Consider an arbitrary node P of the system, containing six DOFs stored in a set r. Each DOF in r can be associated to a rigid body motion by imposing a displacement while keeping the other five DOFs constrained. Let us also consider the set ℓ, containing all DOFs outside r. The static problem in eq. (3.30) can then be partitioned as follows:

$$\begin{bmatrix} \mathbf{K}_{rr} & \mathbf{K}_{r\ell} \\ \mathbf{K}_{\ell r} & \mathbf{K}_{\ell\ell} \end{bmatrix} \begin{bmatrix} \mathbf{\Phi}_{r,r} \\ \mathbf{\Phi}_{r,\ell} \end{bmatrix} = \begin{bmatrix} \mathbf{0} \\ \mathbf{0} \end{bmatrix} \tag{3.31}$$

Considering unit displacements on the DOFs in set r, i.e. $\mathbf{\Phi}_{r,r} = \mathbf{I}$, the second line in eq. (3.31) gives

$$\mathbf{\Phi}_{r,\ell} = -\mathbf{K}_{\ell\ell}^{-1}\mathbf{K}_{\ell r} \tag{3.32}$$

Rigid body modes obtained from the stiffness matrix as shown above may be referred to as static rigid body modes.

3.4 Craig-Bampton reduction

The Craig-Bampton CMS technique, presented in 1968 [8], is the most commonly used method and will also be used in this research. In section 4.5 the Craig-Bampton (CB) reduction basis

[5] Mechanisms, e.g. motion of structures that contain hinges, may be treated as RBMs since they allow parts of the structure to displace without deforming. Although mechanisms satisfy eq. (3.30), they are not treated in this thesis. Hence, $\mathbf{\Phi}_r \in \mathbb{R}^{n \times n_r}$ where $n_r \leq 6$.

will be extended to account for geometrically nonlinear effects. The original reduction basis includes constraint modes (CMs) and internal vibration modes (IVMs), covered in section 3.2.1 and section 3.3.2 respectively. Once the component modes are obtained, implementation of the Craig-Bampton method is straight-forward. This is because a CMS technique requires the boundary DOFs $\mathbf{u}_b$ to be retained (non-reduced) and both CMs and IVMs satisfy this requirement by definition, as can be seen from eqs. (3.11) and (3.29).

Applying modal truncation to the set of IVMs, i.e. only including a few modes, and combining this with the CMs results in the following approximation of the internal displacement field

$$\mathbf{u}_i \approx \boldsymbol{\Psi}_c \mathbf{u}_b + \boldsymbol{\Phi}_i \boldsymbol{\eta}_i \tag{3.33}$$

By including the non-reduced boundary DOFs in this expression and following eq. (3.1), the Craig-Bampton reduction basis can be described as

$$\begin{bmatrix} \mathbf{u}_b \\ \mathbf{u}_i \end{bmatrix} \approx \begin{bmatrix} \mathbf{I} & \mathbf{0} \\ \boldsymbol{\Psi}_c & \boldsymbol{\Phi}_i \end{bmatrix} \begin{bmatrix} \mathbf{u}_b \\ \boldsymbol{\eta}_i \end{bmatrix} = \mathbf{R}\mathbf{q} \tag{3.34}$$

As a final remark it is stressed that rigid body motions can be described by a superposition of CMs. Hence, rigid body modes are present in the CB reduction basis.

3.5 Rubin reduction

In contrast to the CB reduction procedure, where internal vibration modes are used, one could also include vibration modes of the free floating structure; free vibration modes (FVMs). For experimental dynamics, this is convenient as FVMs are directly obtained during measurements. MacNeal [26] introduced a method including these FVMS in 1971 and later an improved method was developed by Rubin in 1975 [33]. Rubin originally claimed his method was not of the general form discussed in section 3.1 (a Rayleigh-Ritz procedure), but later Craig and Chang proved it was [10].

Similar to CB, Rubin's reduction starts by separating the response in a static and dynamic part:

$$\mathbf{u} \approx \mathbf{u}_{stat} + \mathbf{u}_{dyn} = \boldsymbol{\Psi}_r \mathbf{g}_b + \boldsymbol{\Phi}_r \boldsymbol{\eta}_r + \boldsymbol{\Phi}_f \boldsymbol{\eta}_f \tag{3.35}$$

Computation and interpretation of the residual attachment modes $\boldsymbol{\Psi}_r$, rigid body modes $\boldsymbol{\Phi}_r$ and free vibration modes $\boldsymbol{\Phi}_f$ are given in section 3.2.2, section 3.3.3 and section 3.3.1 respectively. From eq. (3.35) a reduction basis of the following form can be constructed:

$$\mathbf{u} \approx \begin{bmatrix} \boldsymbol{\Psi}_r & \boldsymbol{\Phi}_r & \boldsymbol{\Phi}_f \end{bmatrix} \begin{bmatrix} \mathbf{g}_b \\ \boldsymbol{\eta}_r \\ \boldsymbol{\eta}_f \end{bmatrix} = \mathbf{R}\mathbf{q} \tag{3.36}$$

This leads to a *dual* system of equations, i.e. displacement and force DOFs are combined in one set. In contrast to the CB method, the component modes act on the full set of DOFs rather than on the internal DOFs only. It is required to obtain a *primal* system (displacement DOFs only), where the boundary DOFs are not reduced. Therefore, the expression in eq. (3.36) needs

to be mathematically manipulated. Let us first partition the system of equations as:

$$\begin{bmatrix}\mathbf{u}_b\\ \mathbf{u}_i\end{bmatrix} \approx \begin{bmatrix}\boldsymbol{\Psi}_{r,b} & \boldsymbol{\Phi}_{r,b} & \boldsymbol{\Phi}_{f,b}\\ \boldsymbol{\Psi}_{r,i} & \boldsymbol{\Phi}_{r,i} & \boldsymbol{\Phi}_{f,i}\end{bmatrix} \begin{bmatrix}\mathbf{g}_b\\ \boldsymbol{\eta}_r\\ \boldsymbol{\eta}_f\end{bmatrix} \tag{3.37}$$

where the introduced subscripts denote whether the partitioned modes act on boundary or internal DOFs. Solving the first row in this expression for the boundary connection forces $\mathbf{g}_b$ gives

$$\mathbf{g}_b \approx \boldsymbol{\Psi}_{r,b}^{-1}\left(\mathbf{u}_b - \boldsymbol{\Phi}_{r,b}\boldsymbol{\eta}_r - \boldsymbol{\Phi}_{f,b}\boldsymbol{\eta}_f\right) \tag{3.38}$$

From this expression a second coordinate transformation can be defined as:

$$\begin{bmatrix}\mathbf{g}_b\\ \boldsymbol{\eta}_r\\ \boldsymbol{\eta}_f\end{bmatrix} \approx \begin{bmatrix}\boldsymbol{\Psi}_{r,b}^{-1} & -\boldsymbol{\Psi}_{r,b}^{-1}\boldsymbol{\Phi}_{r,b} & -\boldsymbol{\Psi}_{r,b}^{-1}\boldsymbol{\Phi}_{f,b}\\ \mathbf{0} & \mathbf{I} & \mathbf{0}\\ \mathbf{0} & \mathbf{0} & \mathbf{I}\end{bmatrix} \begin{bmatrix}\mathbf{u}_b\\ \boldsymbol{\eta}_r\\ \boldsymbol{\eta}_f\end{bmatrix} = \mathbf{R}_2\mathbf{q}_2 \tag{3.39}$$

The total coordinate transformation that is done to obtain an approximation of the displacement field $\mathbf{u}$, while retaining the boundary DOFs is now found by multiplying eqs. (3.36) and (3.39):

$$\begin{bmatrix}\mathbf{u}_b\\ \mathbf{u}_i\end{bmatrix} \approx \mathbf{R}\mathbf{R}_2\mathbf{q}_2 = \begin{bmatrix}\mathbf{I} & \mathbf{0} & \mathbf{0}\\ \boldsymbol{\Psi}_{r,i}\boldsymbol{\Psi}_{r,b}^{-1} & \boldsymbol{\Phi}_{r,i} - \boldsymbol{\Psi}_{r,i}\boldsymbol{\Psi}_{r,b}^{-1}\boldsymbol{\Phi}_{r,b} & \boldsymbol{\Phi}_{f,i} - \boldsymbol{\Psi}_{r,i}\boldsymbol{\Psi}_{r,b}^{-1}\boldsymbol{\Phi}_{f,b}\end{bmatrix} \begin{bmatrix}\mathbf{u}_b\\ \boldsymbol{\eta}_r\\ \boldsymbol{\eta}_f\end{bmatrix} \tag{3.40}$$

3.6 Substructure assembly

Coupling of substructures is the final step in the CMS process and can be done in three domains: the physical, modal and frequency domain. Only substructure coupling in the modal domain will be discussed in this section, which is the last step described by fig. 3.1. The other two domains are outside the interest of this research, but it can be shown that the methodology of coupling in the physical domain is similar to modal domain coupling.

Neighbouring substructures interact with each other after assembly. Regardless of the domain in which the coupling process takes place, two conditions need to be satisfied:

1. Compatibility; the interface displacement fields $\mathbf{q}_b^{(s)}$ of connecting substructure interfaces must be identical.

2. Equilibrium; the connection forces $\mathbf{g}_b^{(s)}$ between neighbouring substructures must be equal in magnitude and opposite in direction.

Substructure coupling is extensively explained in [11] and later by [24]. However, both references limit their framework to linear systems. Although a similar methodology can be followed as described in the cited references, coupling of nonlinear substructures will be discussed here. The process is started by coupling the nonlinear equations of motion of n_s substructures in one block diagonal form. For the sake of simplicity, damping will be neglected and the notation of time dependencies will be omitted. According to eq. (2.6), the internal forces will be split in a linear and a nonlinear component:

$$\mathbf{M}\ddot{\mathbf{q}} + \mathbf{K}\mathbf{q} + \mathbf{f}^{nl}(\mathbf{q}) = \mathbf{p} + \mathbf{g} \tag{3.41}$$

where

$$\mathbf{M} = \text{diag}\left(\mathbf{M}^{(1)}, \ldots, \mathbf{M}^{(n_s)}\right) = \begin{bmatrix} \mathbf{M}^{(1)} & \mathbf{0} & \mathbf{0} \\ \vdots & \ddots & \vdots \\ \mathbf{0} & \mathbf{0} & \mathbf{M}^{(n_s)} \end{bmatrix}, \qquad \mathbf{K} = \text{diag}\left(\mathbf{K}^{(1)}, \ldots, \mathbf{K}^{(n_s)}\right)$$

$$\mathbf{q} = \begin{bmatrix} \mathbf{q}^{(1)} \\ \vdots \\ \mathbf{q}^{(n_s)} \end{bmatrix}, \qquad \mathbf{f}^{nl} = \begin{bmatrix} \mathbf{f}^{nl(1)} \\ \cdots \\ \mathbf{f}^{nl(n_s)} \end{bmatrix}, \qquad \mathbf{f} = \begin{bmatrix} \mathbf{f}^{(1)} \\ \vdots \\ \mathbf{f}^{(n_s)} \end{bmatrix}, \qquad \mathbf{g} = \begin{bmatrix} \mathbf{g}^{(1)} \\ \vdots \\ \mathbf{g}^{(n_s)} \end{bmatrix}$$

Note that the components of the DOF vector corresponding to the n substructures are generally partitioned into a set of non-reduced boundary DOFs and a set of generalised coordinates. This also states that the subcomponents in this expression are represented in the modal domain and are defined as written in eq. (3.4). The connecting forces $\mathbf{g}$ can be interpreted as constraining forces corresponding to the compatibility conditions. These compatibility conditions can be combined in matrix form as follows:

$$\mathbf{Bq} = \mathbf{0} \tag{3.42}$$

where $\mathbf{B}$ is a signed boolean matrix operating on the interface DOFs of the substructures[6]. The rows in $\mathbf{B}$ state that any pair of interface DOFs $q^{(k)}$ and $q^{(l)}$ must have the same displacement, i.e. $q^{(k)} - q^{(l)} = 0$. The number of linear independent rows in $\mathbf{B}$ is equal to the number of unique compatibility conditions that can be found in the system.

The second condition that needs to be satisfied in substructure coupling is force equilibrium. Similar to eq. (3.42), these conditions can be combined in matrix form:

$$\mathbf{L}^T\mathbf{g} = \mathbf{0} \tag{3.43}$$

where $\mathbf{L}$ is the boolean localisation matrix. This operator states that any pair of interface connecting forces $g^{(k)}$ and $g^{(l)}$ must be in equilibrium, i.e. $g^{(k)} + g^{(l)} = 0$. The total system, consisting of the assembled n_s substructures is now described by eqs. (3.41) to (3.43):

$$\begin{cases} \mathbf{M}\ddot{\mathbf{q}} + \mathbf{Kq} + \mathbf{f}^{nl}(\mathbf{q}) = \mathbf{p} + \mathbf{g} \\ \mathbf{Bq} = \mathbf{0} \\ \mathbf{L}^T\mathbf{g} = \mathbf{0} \end{cases} \tag{3.44}$$

Although no proof will be given in this thesis, the two boolean matrices $\mathbf{B}$ and $\mathbf{L}$ are in each others null space. This leads to the relations:

$$\mathbf{L} = \text{null}\left(\mathbf{B}\right), \qquad \mathbf{B}^T = \text{null}\left(\mathbf{L}^T\right) \tag{3.45}$$

This is a useful property since the generation of $\mathbf{B}$ is more intuitive than that of $\mathbf{L}$. However, it should be noted that computing the nullspace of a large matrix takes a considerable amount of time. In the appendix of [24], a method is proposed to obtain $\mathbf{L}$ from $\mathbf{B}$ without computing its nullspace. Only the number of linearly independent rows in $\mathbf{B}$ matter; any additional (linearly dependent) information will not influence $\mathbf{L}$ due to the relation eq. (3.45).

[6]The matrix $\mathbf{B}$ is not boolean for nonconforming meshes, but these are not considered in this research.

Coupling substructures, i.e. satisfying the compatibility and equilibrium conditions, can be done in two ways; *primal* and *dual* assembly. The first results in a set of unique interface DOFs, whereas the latter retains the full set of global DOFs. In this research primal assembly is considered. This assembly method is intuitive in application, but has the limitation that assembled interfaces must have conforming meshes. Interface DOFs of one substructure will be eliminated such that two assembled components share the same set of interface DOFs.

The unique set of degrees of freedom that is retained after primal assembly will be denoted by $\bar{\mathbf{q}}$. Primal assembly only works for matching interface meshes and therefore it does not matter which displacement field is retained and which is eliminated. The unique set of DOFs is obtained as follows:

$$\mathbf{q} = \mathbf{L}\bar{\mathbf{q}} \tag{3.46}$$

Substituting this expression into the compatibility condition of eq. (3.42) gives

$$\mathbf{B}\mathbf{q} = \mathbf{B}\mathbf{L}\bar{\mathbf{q}} = \mathbf{0} \tag{3.47}$$

The compatibility condition is now satisfied *a priori* by the choice of DOFs in $\bar{\mathbf{q}}$. The system is now described by

$$\begin{cases} \mathbf{M}\mathbf{L}\ddot{\bar{\mathbf{q}}} + \mathbf{K}\mathbf{L}\bar{\mathbf{q}} + \mathbf{f}^{nl}(\mathbf{L}\bar{\mathbf{q}}) = \mathbf{p} + \mathbf{g} \\ \mathbf{L}^T\mathbf{g} = \mathbf{0} \end{cases} \tag{3.48}$$

Premultiplying the resulting equations of motion by $\mathbf{L}^T$ eliminates the connecting forces and gives the final equations of the primal assembled system:

$$\bar{\mathbf{M}}\ddot{\bar{\mathbf{q}}} + \bar{\mathbf{K}}\mathbf{L}\bar{\mathbf{q}} + \bar{\mathbf{f}}^{nl}(\mathbf{L}\bar{\mathbf{q}}) = \bar{\mathbf{p}} \tag{3.49}$$

where

$$\bar{\mathbf{M}} = \mathbf{L}^T\mathbf{M}\mathbf{L}, \qquad \bar{\mathbf{K}} = \mathbf{L}^T\mathbf{K}\mathbf{L}, \qquad \bar{\mathbf{f}}^{nl} = \mathbf{L}^T\mathbf{f}^{nl}, \qquad \bar{\mathbf{p}} = \mathbf{L}^T\mathbf{p}$$

Regarding the presented primal assembly process, a number of general remarks can be made:

- In practice, since $\mathbf{f}^{nl}$ is displacement-dependent, the vector $\bar{\mathbf{f}}^{nl}$ is never computed. During the assembly routine in a FE program, the constant properties ($\bar{\mathbf{M}}$, $\bar{\mathbf{K}}$, $\bar{\mathbf{p}}$) are computed once for all. The nonlinear forces are assembled element-wise during the response analysis on the FE model.
- The method explained in this section describes the coupling of substructures in the modal domain. It was already mentioned that coupling in the physical domain is done in a similar fashion. In fact, when no reduction is applied and the system is this described in the physical domain, a reduction basis would be equal to the identity matrix $\mathbf{I} \in \mathbb{R}^{n\times n}$. If so, eq. (3.1) describes $\mathbf{u} = \mathbf{I}\mathbf{q} = \mathbf{q}$ for the mass matrix and similar for the other system properties. Knowing this, the same procedure as described in this section may be followed, apart from some notational differences.

4 Nonlinear Model Order Reduction

An introduction to geometric nonlinearities is given in chapter 2. There, it is stated that solving the nonlinear equilibrium equations requires an iterative algorithm such as the Newton-Raphson method. Even with the constantly growing capacities of computers, nonlinear analyses often still require significantly large computation times. Hence, when nonlinear behaviour of structures is required to be investigated, reduction methods to decrease computation time are of great interest. Reduction methods for linear dynamics problems, such as the Craig-Bampton and Rubin methods (sections 3.4 and 3.5 respectively), are widely used. The idea behind these methods, and other related reduction techniques, is that most of the energy of a system in motion can be related to only a few eigenmodes. By projecting the equations of motion on a basis that is spanned by these few eigenmodes, the equations are reduced in order and this decreases the time needed to solve them. For nonlinear analysis however, eigenmodes are a function of the deformed configuration and thus change over time. The cost of recomputing the eigenvalue problem eq. (3.28) at every time step would not make the reduction method more efficient than solving the full set of equations. Hence, a reduction basis that is able to capture (geometrically) nonlinear effects without the need for updating the basis is widely welcomed. In this thesis, *modal derivatives* (MDs) will be used to extend the existing linear reduction bases defined by Craig and Bampton and Rubin such that a suitable basis for nonlinear dynamic analysis can be formed.

4.1 Theory of modal derivatives

The reduction bases presented in the previous chapter are not able to predict nonlinear dynamic response, because the underlying principle of the free vibration problem that is solved to obtain the internal vibration modes assumes small displacements (the linearised eigenproblem is solved). However when the deformations in a system become larger, geometric effects cause the eigenfrequencies to become dependent on the amplitude of vibration. This introduces the softening or hardening effect illustrated in fig. 4.1. Information on the curvature of the frequency-amplitude relation needs to be stored in the reduction basis in order to capture geometric nonlinearities in the reduced model. In order to describe these higher order effects with a basis similar to CB or Rubin, the concept of *modal derivatives* (MDs) was introduced by Idelsohn and Cardona in 1985 [22]. Later, similar research was done and reported in [34]. Modal derivatives are used to describe the second-order effects that occur when considering (geometrical) nonlinearities. Including MDs in nonlinear Model Order Reduction already led to reduced systems that were able to accurately describe nonlinear dynamic behaviour [22, 34, 36]. No research is found where this technique is combined with CMS. The advantage of this would be the inclusion of local second-order effects.

In order to mathematically explain the concept of modal derivatives, consider a system with

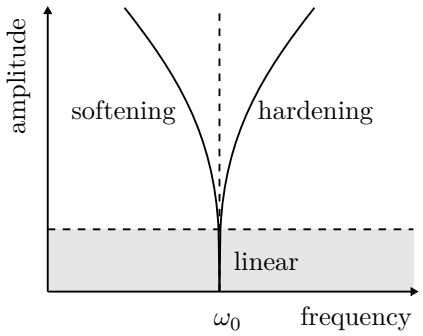

Figure 4.1: *Frequency-amplitude relation for a nonlinear system; once the amplitude of vibration becomes sufficiently large, the system's eigenfrequency either decreases (softening) or increases (hardening) as a function of the vibration amplitude.*

n degrees of freedom. These DOFs may be approximated according to the mode superposition principle:

$$\mathbf{u} \approx \boldsymbol{\Phi}\boldsymbol{\eta} = \sum_{j=1}^{M} \boldsymbol{\phi}_j \eta_j \tag{4.1}$$

where $M \ll n$, i.e. mode truncation is already applied in eq. (4.1). The modal coordinate corresponding to the mode $\boldsymbol{\phi}_j$ is denoted by η_j. For nonlinear systems, the modes are deformation dependent and a description of the physical coordinates $\mathbf{u}$ as done in eq. (4.1) will no longer hold. This can interpreted by noting that a cantilever beam which is deforming largely in the direction of the first bending mode, will also shorten in length due to bending-stretching coupling. These second-order effects are not described by the linear modes[1]. To include second-order terms as well, a Taylor series expansion around working point $\mathbf{u}_{eq} = \mathbf{0}$ is performed:

$$\mathbf{u} \approx \sum_{j=1}^{M} \left.\frac{\partial \mathbf{u}}{\partial \eta_j}\right|_{\mathbf{u}_{eq}} \eta_j + \frac{1}{2} \sum_{j=1}^{M} \sum_{k=1}^{M} \left.\frac{\partial^2 \mathbf{u}}{\partial \eta_j \partial \eta_k}\right|_{\mathbf{u}_{eq}} \eta_k \eta_j \tag{4.2}$$

The derivatives in this expression can be rewritten according to eq. (4.1):

$$\frac{\partial \mathbf{u}}{\partial \eta_j} = \boldsymbol{\phi}_j + \sum_{k=1}^{M} \frac{\partial \boldsymbol{\phi}_k}{\partial \eta_j} \eta_k \tag{4.3}$$

$$\frac{\partial^2 \mathbf{u}}{\partial \eta_j \partial \eta_k} = \frac{\partial \boldsymbol{\phi}_j}{\partial \eta_k} + \frac{\partial \boldsymbol{\phi}_k}{\partial \eta_j} + \sum_{\ell=1}^{M} \frac{\partial^2 \boldsymbol{\phi}_\ell}{\partial \eta_j \partial \eta_k} \eta_\ell \tag{4.4}$$

In the reference configuration $\mathbf{u}_{eq} = \mathbf{0}$, the modal amplitudes are zero by definition. This

[1] In theory, including compression modes will in this case be sufficient, but in practice this involves including a large number of linear modes to account for all second-order effects. The size of the reduced basis will then grow such that the computational cost of solving the linear eigenvalue problem together with the nonlinear analysis on the larger reduced basis results in an inefficient analysis.

changes the derivatives to

$$\frac{\partial \mathbf{u}}{\partial \eta_j} = \boldsymbol{\phi}_j \tag{4.5}$$

$$\frac{\partial^2 \mathbf{u}}{\partial \eta_j \partial \eta_k} = \frac{\partial \boldsymbol{\phi}_j}{\partial \eta_k} + \frac{\partial \boldsymbol{\phi}_k}{\partial \eta_j} = 2\frac{\partial \boldsymbol{\phi}_j}{\partial \eta_k} \tag{4.6}$$

It can be shown that the MDs are symmetric, i.e. $\frac{\partial \boldsymbol{\phi}_j}{\partial \eta_k} = \frac{\partial \boldsymbol{\phi}_k}{\partial \eta_j}$ as exploited in eq. (4.6). Substituting the expressions above into eq. (4.2) and taking the symmetry into account gives

$$\mathbf{u} \approx \sum_{j=1}^{M} \boldsymbol{\phi}_j \eta_j + \sum_{j=1}^{M} \sum_{k=1}^{M} \frac{\partial \boldsymbol{\phi}_j}{\partial \eta_k} \eta_k \eta_j = \boldsymbol{\Phi}\boldsymbol{\eta} + \boldsymbol{\Theta}\boldsymbol{\xi} \tag{4.7}$$

For implementation convenience, a new modal coordinate $\xi_\ell = \eta_k \eta_j,\ \ell = 1, \ldots, kj$ will be introduced and linked to the modal derivatives, included in matrix $\boldsymbol{\Theta}$. The superposition in eq. (4.7) describes second-order nonlinearities.

4.2 Computation of modal derivatives

Modal derivatives can both be computed analytically and numerically (see [22, 34]). A numerical approach uses the finite difference method. An analytical computation is preferable due to accuracy reasons and in the case of geometric nonlinearities, such an approach is possible. Following [36], let us linearise the undamped nonlinear equilibrium equations around the working point $\mathbf{u}_{eq}$ and assuming any motion $\Delta\mathbf{u}$ around $\mathbf{u}_{eq}$ is small, i.e. $\mathbf{u} = \mathbf{u}_{eq} + \Delta\mathbf{u}$, $\ddot{\mathbf{u}} = \Delta\ddot{\mathbf{u}}$:

$$\mathbf{M}\Delta\ddot{\mathbf{u}} + \mathbf{K}_{eq}\Delta\mathbf{u} = \mathbf{0} \tag{4.8}$$

where the tangent stiffness matrix[2] is defined as

$$\mathbf{K}_{eq} = \left.\frac{\partial \mathbf{f}}{\partial \mathbf{u}}\right|_{\mathbf{u}=\mathbf{u}_{eq}} \tag{4.9}$$

The eigenvalue problem corresponding to eq. (4.8) can be written as

$$\left(\mathbf{K}_{eq} - \omega_i^2 \mathbf{M}\right) \boldsymbol{\phi}_i = \mathbf{0} \qquad i = 1, 2, \ldots, N \tag{4.10}$$

This expression can be differentiated with respect to the modal coordinate η_j. This results in

$$\left(\frac{\partial \mathbf{K}_{eq}}{\partial \eta_j} - \frac{\partial \omega_i^2}{\partial \eta_j}\mathbf{M}\right) \boldsymbol{\phi}_i + \left(\mathbf{K}_{eq} - \omega_i^2 \mathbf{M}\right) \boldsymbol{\theta}_{ij} = \mathbf{0} \tag{4.11}$$

where

$$\boldsymbol{\theta}_{ij} = \frac{\partial \boldsymbol{\phi}_i}{\partial \eta_j}$$

[2] Note that in the presented derivation, the stiffness matrix is not split in a linear and nonlinear part

The eigenfrequency ω_i of a system is not a function of the modal amplitude and therefore its partial derivative vanishes. Inertia terms in this expression will be ignored, since it can be shown that changing the system's mass only scales the amplitudes of the MDs and not their shapes; numerical studies by both Idelsohn and Cardona [22, 21] and Slaats et al. [34] have confirmed this. Hence, modal derivatives may be interpreted as a static correction of the selected vibration modes. Equation (4.11) may thus be simplified to

$$\mathbf{K}_{eq}\boldsymbol{\theta}_{ij} = -\frac{\partial \mathbf{K}_{eq}}{\partial \eta_j}\boldsymbol{\phi}_i \tag{4.12}$$

The right-hand side of this equation represents a pseudo-force that is caused by the displacement field $\boldsymbol{\theta}_{ij}$. Note that taking the derivative of the static problem ($\mathbf{K}\boldsymbol{\phi} = \mathbf{0}$) with respect to the modal coordinate results in the same expression, which verifies the interpretation of MDs as static corrections. For a constrained problem, the stiffness matrix is invertible, such that the definition of a modal derivative may be written as

$$\boldsymbol{\theta}_{ij} = -\mathbf{K}_{eq}^{-1}\frac{\partial \mathbf{K}_{eq}}{\partial \eta_j}\boldsymbol{\phi}_i \tag{4.13}$$

Given M selected vibration modes, $R = M(M+1)/2$ modal derivatives exist due to the earlier mentioned symmetry. The symmetry is also illustrated in appendix B.

4.3 Finite element implementation

The central problem of computing modal derivatives, eq. (4.13), includes the derivative of the stiffness matrix. This term needs to be computed at element level and in order to do this correctly, the finite element formulation should be consulted. For the shell element used in this study, an overview of this formulation is given in appendix A.

Starting from the virtual work balance, we can write down the equilibrium between internal and external virtual work:

$$\boldsymbol{\sigma}\delta\boldsymbol{\varepsilon} = \mathbf{f}\delta\mathbf{u} \tag{4.14}$$

Following eq. (A.11), the strain-displacement relation in variational form is written as

$$\delta\boldsymbol{\varepsilon} = \mathbf{B}_L\delta\mathbf{u} + \frac{1}{2}\delta\mathbf{B}_{NL}(\mathbf{u})\mathbf{u} + \frac{1}{2}\mathbf{B}_{NL}(\mathbf{u})\delta\mathbf{u} \tag{4.15}$$

This expression can be simplified by noting the definition of the nonlinear strain matrix $\mathbf{B}_{NL}$ in eq. (A.17). From that expression it follows that $\delta\mathbf{B}_{NL}(\mathbf{u})\mathbf{u} = \mathbf{B}_{NL}(\mathbf{u})\delta\mathbf{u}$ and therefore eq. (4.15) may be rewritten as follows:

$$\delta\boldsymbol{\varepsilon} = \left(\mathbf{B}_L + \mathbf{B}_{NL}(\mathbf{u})\right)\delta\mathbf{u} \tag{4.16}$$

Now, the elastic constitutive relation is found by substituting eq. (A.11) into eq. (A.22):

$$\boldsymbol{\sigma} = \mathbf{H}\boldsymbol{\varepsilon} = \mathbf{H}\left(\mathbf{B}_L\mathbf{u} + \frac{1}{2}\mathbf{B}_{NL}(\mathbf{u})\mathbf{u}\right) \tag{4.17}$$

From now on, dependencies between brackets will be omitted for clarity reasons. Combining eqs. (4.16) and (4.17), the internal virtual work may be written as

$$\boldsymbol{\sigma}\delta\boldsymbol{\varepsilon} = \delta\mathbf{u}^T \left[\left(\mathbf{B}_L^T + \mathbf{B}_{NL}^T \right) \mathbf{H} \left(\mathbf{B}_L\mathbf{u} + \frac{1}{2}\mathbf{B}_{NL}\mathbf{u} \right) \right] \tag{4.18}$$

$$= \delta\mathbf{u}^T \left[\mathbf{B}_L^T\mathbf{H}\mathbf{B}_L\mathbf{u} + \frac{1}{2}\mathbf{B}_L^T\mathbf{H}\mathbf{B}_{NL}\mathbf{u} + \mathbf{B}_{NL}^T\mathbf{H}\mathbf{B}_L\mathbf{u} + \frac{1}{2}\mathbf{B}_{NL}^T\mathbf{H}\mathbf{B}_{NL}\mathbf{u} \right] \tag{4.19}$$

The internal forces inside an element now follow from eq. (4.14):

$$\mathbf{f}_e = \mathbf{B}_L^T\mathbf{H}\mathbf{B}_L\mathbf{u} + \frac{1}{2}\mathbf{B}_L^T\mathbf{H}\mathbf{B}_{NL}\mathbf{u} + \mathbf{B}_{NL}^T\mathbf{H}\mathbf{B}_L\mathbf{u} + \frac{1}{2}\mathbf{B}_{NL}^T\mathbf{H}\mathbf{B}_{NL}\mathbf{u} \tag{4.20}$$

The internal forces $\mathbf{f}_e \in \mathbb{R}^{18\times 1}$ are computed on element level and then assembled. The elemental tangent stiffness matrix representing the total stiffness is found by differentiating the internal force vector with respect to $\mathbf{u}$:

$$\begin{aligned}\mathbf{K}_e = \frac{\partial \mathbf{f}_e}{\partial \mathbf{u}} = {} & \mathbf{B}_L^T\mathbf{H}\mathbf{B}_L + \frac{1}{2}\mathbf{B}_L^T\mathbf{H}\mathbf{B}'_{NL}\mathbf{u} + \frac{1}{2}\mathbf{B}_L^T\mathbf{H}\mathbf{B}_{NL} + \mathbf{B}'^T_{NL}\mathbf{H}\mathbf{B}_L\mathbf{u} + \mathbf{B}_{NL}^T\mathbf{H}\mathbf{B}_L \\ & + \frac{1}{2}\mathbf{B}'^T_{NL}\mathbf{H}\mathbf{B}_{NL}\mathbf{u} + \frac{1}{2}\mathbf{B}_{NL}^T\mathbf{H}\mathbf{B}'_{NL}\mathbf{u} + \frac{1}{2}\mathbf{B}_{NL}^T\mathbf{H}\mathbf{B}_{NL}\end{aligned} \tag{4.21}$$

where

$$\mathbf{B}'_{NL} = \frac{\partial \mathbf{B}_{NL}}{\partial \mathbf{u}} = \begin{bmatrix} \mathbf{K}_{xx} & \mathbf{K}_{yy} & \mathbf{K}_{xy} \end{bmatrix}^T \tag{4.22}$$

The terms in the expression above, given in eq. (A.18), should not be confused with the stiffness matrix. Hence, multiplying eq. (4.22) by $\mathbf{u}$ again gives the original expression for $\mathbf{B}_{NL}$ (given in eq. (A.17)). This simplifies the expression in eq. (4.21), which can be rewritten after rearranging the terms:

$$\mathbf{K}_e = \mathbf{B}_L^T\mathbf{H}\mathbf{B}_L + \mathbf{B}_L^T\mathbf{H}\mathbf{B}_{NL} + \mathbf{B}_{NL}^T\mathbf{H}\mathbf{B}_L + \mathbf{B}_{NL}^T\mathbf{H}\mathbf{B}_{NL} + \mathbf{B}'^T_{NL}\mathbf{H}(\mathbf{B}_L + \frac{1}{2}\mathbf{B}_{NL})\mathbf{u} \tag{4.23}$$

Note that by definition $\mathbf{K}_e \in \mathbb{R}^{18\times 18}$ for a three dimensional, three noded shell element. However, the expression in eq. (4.22) has dimensions 54×18 and is multiplied by $\mathbf{H}(\mathbf{B}_L + \frac{1}{2}\mathbf{B}_{NL})\mathbf{u} \in \mathbb{R}^{3\times 1}$ (see the last term on the right-hand side of eq. (4.21)). In order to multiply successfully and output a term of size 18×18, the derivative in eq. (4.22) is taken element-wise[3].

Taking the derivative of the stiffness matrix with respect to the displacements vector is required for the computation of the modal derivative, according to the fundamental expression in eq. (4.13). However, as this derivative would lead to a third-order tensor, computations will become inefficient and any physical interpretation will be lost. In practice, the expression is evaluated at element level and then assembled, so the third-order tensor is never explicitly

[3] The multiplication of the last term on the right-hand side of eq. (4.21) is then performed as

$$\mathbf{K}_{xx}\left(\mathbf{b}_1\mathbf{H}(\mathbf{B}_L + \frac{1}{2}\mathbf{B}_{NL})\mathbf{u}\right) + \mathbf{K}_{yy}\left(\mathbf{b}_2\mathbf{H}(\mathbf{B}_L + \frac{1}{2}\mathbf{B}_{NL})\mathbf{u}\right)\mathbf{K}_{xy}\left(\mathbf{b}_3\mathbf{H}(\mathbf{B}_L + \frac{1}{2}\mathbf{B}_{NL})\mathbf{u}\right)$$

where three boolean operators for element selection are introduced:

$$\mathbf{b}_1 = \begin{bmatrix}1 & 0 & 0\end{bmatrix}, \qquad \mathbf{b}_2 = \begin{bmatrix}0 & 1 & 0\end{bmatrix}, \qquad \mathbf{b}_3 = \begin{bmatrix}0 & 0 & 1\end{bmatrix}$$

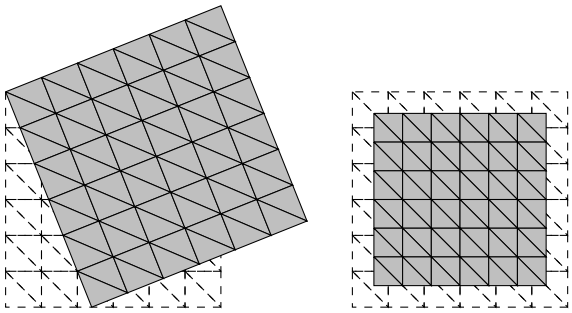

(a) *Rigid body mode* **(b)** *Rigid body derivative*

Figure 4.2: *Rectangular plate undergoing a rigid body rotation around its y-axis, described by a linear and a nonlinear representation. The undeformed geometry is shown in dashed lines.*

computed and the involved computational cost is of the same order as evaluating the stiffness matrix times a vibration mode $\boldsymbol{\phi}_k$ [22]. The derivative of the stiffness matrix times a vibration mode is computed component-wise. Using the chain rule, every component K_{ij} of the stiffness matrix is derived as follows:

$$\frac{\partial K_{ij}}{\partial u_\ell}\frac{\partial u_\ell}{\partial \eta_k} = \frac{\partial K_{ij}}{\partial u_\ell}\phi_k \tag{4.24}$$

This expression can be substituted in eq. (4.13) and the modal derivative is found by multiplying this with the second mode and pre-multiplying it with the inverse of the stiffness matrix.

4.4 Rigid body derivatives

A special type of modal derivatives that are used in this thesis are modal derivatives of rigid body modes, called *rigid body derivatives* (RBDs). This type of second-order modes are used for the extension of the Rubin method, described in section 4.6. The computation of RBDs is the same as the computation of MDs from free vibration modes.

Rigid body derivatives corresponding to translational RBMs do not lead to new and unique modes and therefore do not add additional information to the reduction basis. If a translational RBM is multiplied by a large modal amplitude, the shape of the FE model will not change. Hence, including MDs of translational RBMs leads to a singular system. However, the same does not hold for RBDs corresponding to rotational RBMs. Figure 4.2 illustrates the response of a (linear) rotational rigid body mode (about the z-axis). The area of the structure grows compared to the undeformed geometry, which is not physically correct. In order to correct for this growth, the rigid body derivative shown in fig. 4.2b is needed. When simulating the response of the same RBM, combined with its RBD, the shape of the system remains the same; it is rotated about z but remains undeformed. Therefore, without loss of accuracy, only MDs of rotational RBMs should be included. More RBDs, as well as their interaction with MDs of free vibration modes, are illustrated in appendix B.

4.5 Extension of Craig-Bampton method for nonlinear dynamics

The Craig-Bampton reduction basis, given in eq. (3.34), can be extended such that it will be able to capture second-order nonlinearities as well. Let us therefore note that the system's response in a CMS technique is divided into a static and a dynamic part, see eq. (3.33) for the CB method. Now, by replacing the dynamic part of that equation by eq. (4.7), the internal DOFs may be approximated as

$$\mathbf{u}_i \approx \mathbf{\Psi}_c \mathbf{u}_b + \mathbf{\Phi}_i \boldsymbol{\eta}_i + \mathbf{\Theta}_i \boldsymbol{\xi}_i \tag{4.25}$$

where the subscripts i indicate properties corresponding to internal DOFs, since CB does not reduce the boundary DOFs. Hence, the modal derivatives in $\mathbf{\Theta}_i$ are found from following section 4.1 and imposing $\mathbf{u}_b = \mathbf{0}$. By including the boundary DOFs as well, the reduction basis of the Craig-Bampton method (eq. (3.34)) can be extended to include second-order effects:

$$\begin{bmatrix} \mathbf{u}_b \\ \mathbf{u}_i \end{bmatrix} \approx \begin{bmatrix} \mathbf{I} & \mathbf{0} & \mathbf{0} \\ \mathbf{\Psi}_c & \mathbf{\Phi} & \mathbf{\Theta} \end{bmatrix} \begin{bmatrix} \mathbf{u}_b \\ \boldsymbol{\eta} \\ \boldsymbol{\xi} \end{bmatrix} = \mathbf{R}\mathbf{q} \tag{4.26}$$

4.6 Extension of Rubin method for nonlinear dynamics

After two coordinate transformations, the Rubin reduction basis is found in eq. (3.40). In order to extend this bases such that nonlinearities can be captured, the same analogy as for the CB method in section 4.5 can be followed.

First, let us separate the approximated response in a static and a dynamic part as in eq. (3.35). The dynamic part can be extended according to eq. (4.7). This gives

$$\mathbf{u} \approx \mathbf{\Psi}_r \mathbf{g}_b + \mathbf{\Phi}_r \boldsymbol{\eta}_r + \mathbf{\Phi}_f \boldsymbol{\eta}_f + \mathbf{\Theta}_f \boldsymbol{\xi}_f \tag{4.27}$$

Since boundary and internal DOFs are not distinguished in this expression, while it is required to retain the boundary DOFs, a second coordinate transformation is needed. This is similar to the steps described in section 3.5. The resulting Rubin reduction basis for nonlinear dynamics is then found to be

$$\begin{bmatrix} \mathbf{u}_b \\ \mathbf{u}_i \end{bmatrix} \approx \begin{bmatrix} \mathbf{I} & \mathbf{0} & \mathbf{0} & \mathbf{0} \\ \mathbf{\Psi}_{r,i}\mathbf{\Psi}_{r,b}^{-1} & \mathbf{\Phi}_{r,i} - \mathbf{\Psi}_{r,i}\mathbf{\Psi}_{r,b}^{-1}\mathbf{\Phi}_{r,b} & \mathbf{\Phi}_{f,i} - \mathbf{\Psi}_{r,i}\mathbf{\Psi}_{r,b}^{-1}\mathbf{\Phi}_{f,b} & \mathbf{\Theta}_{f,i} - \mathbf{\Psi}_{r,i}\mathbf{\Psi}_{r,b}^{-1}\mathbf{\Theta}_{f,b} \end{bmatrix} \begin{bmatrix} \mathbf{u}_b \\ \boldsymbol{\eta}_r \\ \boldsymbol{\eta}_f \\ \boldsymbol{\xi}_f \end{bmatrix} \tag{4.28}$$

where subscripts i and b respectively indicate correspondence to internal and boundary DOFs. Corresponding to the presented extension of the Rubin reduction technique, some remarks should be made:

- Rigid body modes are included in the Rubin reduction method for linear dynamics, see eq. (3.35). The modal derivatives stored in $\mathbf{\Theta}_f$ come from both the free vibration modes and the rotational rigid body modes (see section 4.4).

- Since the Rubin method is a free interface method, the stiffness matrix in eq. (4.13) is unconstrained and thus not invertible. In order to compute the MDs, a pseudo-inverse of the stiffness matrix should be taken [16]. This can be interpreted as temporarily constraining a set of DOFs to obtain an invertible stiffness matrix.

4.7 Mode selection criterion

The complete set of R modal derivatives that can be computed from M linearised modes is quadratic with respect to M; $R = M^2$. However, due to the symmetry of modal derivatives, $R = M(M+1)/2$ unique modal derivatives can be computed. Hence, including MDs to capture the geometrical nonlinear effects leads to a quickly growing reduction basis, lowering the order difference between the physical and generalised coordinates. It is therefore desired to develop a selection criterion to find an optimal set of $P < R$ MDs.

In this section, a selection criterion on substructure level is presented to select the dominant modal derivatives prior to their computation. This is done with information from a linear response analysis, which is computationally cheap. The selection criterion is partly based on the criterion introduced by Tiso in [36], but adjusted for substructuring methods. The selection criterion makes use of the truncated set of *linear normal equations*; the frequency content and shape of the loading must therefore be accurately described by the set of M considered linearised modes.

Recall that the physical displacement field of every substructure can be approximated by a truncated set of $M < n$ modes and their amplitudes:

$$\mathbf{u}^{(s)} \approx \sum_{k=1}^{M} \boldsymbol{\phi}_k^{(s)} \eta_k^{(s)}(t) = \boldsymbol{\Phi}^{(s)} \boldsymbol{\eta}^{(s)} \tag{4.29}$$

The discussion will be proceeded at substructure level and to simplify the notation, substructure indicators will be omitted. The approximated displacement field in eq. (4.29) can be substituted into the linear equations of motion. After premultiplication by $\boldsymbol{\Phi}^T$, these equations can be written as

$$\boldsymbol{\Phi}^T \mathbf{M} \boldsymbol{\Phi} \boldsymbol{\eta} + \boldsymbol{\Phi}^T \mathbf{K} \boldsymbol{\Phi} \boldsymbol{\eta} = \boldsymbol{\Phi}^T \mathbf{p}(t) \tag{4.30}$$

These equations can be uncoupled by exploiting the following properties deduced from the mode orthogonality principle [16]:

$$\boldsymbol{\phi}_k^T \mathbf{M} \boldsymbol{\phi}_k = \mu_k \qquad \boldsymbol{\phi}_k^T \mathbf{K} \boldsymbol{\phi}_k = \gamma_k \qquad \frac{\gamma_k}{\mu_k} = \omega_k^2 \tag{4.31}$$

Substitution in eq. (4.30) leads to a set of M uncoupled *normal equations*:

$$\ddot{\eta}_k(t) + \omega_k^2 \eta_k(t) = \frac{\boldsymbol{\phi}_k^T \mathbf{p}(t)}{\mu_k} \tag{4.32}$$

where the right-hand side denotes the modal participation factor, describing how well the loading is represented in the space of mode $\boldsymbol{\phi}_k$. The linear equations of motion can thus be decoupled completely and solved efficiently. For a system of M DOFs, the normal equations in eq. (4.32) can be interpreted as M linear single DOF oscillators that are all contributing to the response of the global system. When nonlinearities are considered, the normal equations will no

longer be uncoupled. Assuming the nonlinear contribution is only mild, the nonlinearities can be treated as a second-order effect (higher orders are neglected). A second-order, geometrically nonlinear effect is here represented by the combination of modal amplitudes of two vibration modes:

$$b_{ij} = \texttt{max}\,|\eta_i| \cdot \texttt{max}\,|\eta_j| \tag{4.33}$$

Note that a modal derivative $\boldsymbol{\theta}_{ij}$ can be interpreted as the way a vibration mode $\boldsymbol{\phi}_j$ is perturbed by the displacement field described by $\boldsymbol{\phi}_i$. Hence, the most dominant modal derivatives can be selected from the highest values of b_{ij} in eq. (4.33).

4.7.1 Accuracy of mode selection criterion

The coefficients b_{ij} will sort the most dominant modal derivatives $\boldsymbol{\theta}_{ij}$ that can be computed from the set of M vibration modes. Therefore it must be ensured that this set is accurately describing the linear response of the system; if dominant vibration modes are neglected, their corresponding dominant modal derivatives are excluded in the reduction basis as well. Therefore, the convergence properties of the underlying linear problem is studied next.

A solution for the M second-order differential equations in eq. (4.32) can be found in the form of a homogeneous and a particular solution:

$$\eta_k = \eta_k^H + \eta_k^P \tag{4.34}$$

Generally, a solution for this equation cannot be found unless rest initial conditions are assumed. By assuming the system is initially at rest, the homogenous solution η_k^H becomes zero and the general form of a particular solution that satisfies the initial conditions is given by Duhamel's integral:

$$\eta_k = \eta_k^P = \frac{1}{\omega_k} \int_0^t \frac{\boldsymbol{\phi}_k^T \mathbf{p}(\tau)}{\mu_k} \sin \omega_k (t-\tau) d\tau \tag{4.35}$$

The external force vector can also be split in a static load contribution $\boldsymbol{\lambda}$ and a temporal function $\varphi(t)$:

$$\mathbf{p}(t) = \boldsymbol{\lambda} \varphi(t) \tag{4.36}$$

This allows to rewrite the solution for the modal amplitudes:

$$\eta_k = \frac{1}{\omega_k} \frac{\boldsymbol{\phi}_k^T \boldsymbol{\lambda}}{\mu_k} \int_0^t \varphi(\tau) \sin \omega_k (t-\tau) d\tau \tag{4.37}$$

The approximated response is then found by substituting this expression into eq. (4.29). Based on the obtained expression, remarks can be made regarding the accuracy of the approximated response and thus regarding the mode selection coefficients in eq. (4.33):

- The spatial term $\boldsymbol{\phi}_k^T \boldsymbol{\lambda}$ must be small for the $n - M$ neglected modes, i.e. for $k > M$. This means that the shape of $\boldsymbol{\lambda}$ must be well approximated by the set $\boldsymbol{\Phi}$.
- The temporal term $\frac{1}{\omega_k} \int_0^t \varphi(\tau) \sin \omega_k (t-\tau) d\tau$ must be small for $k > M$, which depends on the frequency content of the system and the applied load. It is required that the convolution product converges to zero for increasing frequencies.

Hence, the approximated linear response by the M modes in eq. (4.29) must be accurately describing the exact solution. It is therefore required to confirm this prior to the nonlinear analysis where a optimal set of P MDs, chosen from the highest values in eq. (4.33), is added to the reduction basis. This confirmation is done by comparing the approximated linear response with the exact linear response. Both analysis are computationally cheap (see section 5.2).

5 Response analysis

One of the many tasks of an engineer is finding the response of a structure when it is subjected to a load of which both the spatial and temporal distribution is known. In FE analysis, one is often interested in the displacements, velocities and accelerations of DOFs as a function of time. These are obtained by solving the dynamic equilibrium equations; eq. (2.4) for linear dynamics and eq. (2.5) for nonlinear dynamics. Although standard procedures exist to obtain the solution to these kind of equations, solving the system of equations becomes expensive if the order of the system is large. The solution methods used in this research are categorised under the *direction integration methods*. After elaborating the fundamentals of direct integration, we present a method where nonlinear time integration is performed only on the corresponding nonlinear components.

5.1 Principles of direct integration methods

The dynamic equilibrium at time $t = t_n$ for a geometrically nonlinear system can be written as:

$$\mathbf{M}\ddot{\mathbf{q}}_n + \mathbf{C}\dot{\mathbf{q}}_n + \mathbf{f}(\mathbf{q}_n) = \mathbf{p}_n \tag{5.1}$$

For a system having N degrees of freedom, eq. (5.1) describes a set of N second-order differential equations with $3N$ unknowns. In direct time integration techniques, the remaining $2N$ equations that are needed to solve eq. (5.1) follow from the finite difference principle:

$$\dot{\mathbf{q}}_n = \lim_{h\to 0} \frac{\mathbf{q}_n - \mathbf{q}(t_n \mp h)}{\pm h} \qquad\qquad \ddot{\mathbf{q}}_n = \lim_{h\to 0} \frac{\dot{\mathbf{q}}_n - \dot{\mathbf{q}}(t_n \mp h)}{\pm h} \tag{5.2}$$

Integration schemes consist of approximating the two expressions in eq. (5.2) in order to find two more relations between $\mathbf{q}_n$, $\dot{\mathbf{q}}_n$ and $\ddot{\mathbf{q}}_n$. The initial boundary conditions, i.e. the displacements and velocities ($\mathbf{q}_0$, $\dot{\mathbf{q}}_0$) at time $t = 0$, are usually known. Summarizing, direct integration methods compute conditions at time t_{n+1} from the equations of motion, finite difference equations and known conditions at preceding time steps. Algorithms can be classified as *explicit* or *implicit* [6]. An explicit integration algorithm uses only historical information, i.e. response data from previous time steps. For an implicit algorithm, the state vector at time t_{n+1} is a function of its own time derivatives. Implicit schemes can be unconditionally stable, but the cost per time step is higher than for explicit algorithms. For conventional structural vibration problems, such as the problems considered in this thesis, implicit schemes are used.

5.2 The Newmark method for linear dynamics

The single-step algorithm proposed by Newmark in 1959 is commonly used in structural analysis [27]. Let us first write down the Taylor series expansion of a function f at time $t_{n+1} = t_n + h$

[16]:

$$f(t_n + h) = f(t_n) + h\dot{f}(t_n) + \frac{h^2}{2}\ddot{f}(t_n) + \frac{h^3}{6}\dddot{f}(t_n) + \dots \tag{5.3}$$

Using this expansion, conditions at time t_{n+1} are deduced from known information at time t_n. Newmark expressed the displacement and velocity vectors at time t_{n+1} in this form and truncated higher order terms:

$$\begin{aligned} \mathbf{q}_{n+1} &= \mathbf{q}_n + h\dot{\mathbf{q}}_n + \frac{h^2}{2}\ddot{\mathbf{q}}_n + \beta h^3 \dddot{\mathbf{q}}_n \\ \dot{\mathbf{q}}_{n+1} &= \dot{\mathbf{q}}_n + h\ddot{\mathbf{q}}_n + \gamma h^2 \dddot{\mathbf{q}}_n \end{aligned} \tag{5.4}$$

These expressions are no longer exact, as all fourth-order terms are ignored. Newmark also introduced the intergration constants β and γ. The rate of change of accelerations, also called jerk, is an uncommon term in eq. (5.4). Newmark approximated this by assuming linear acceleration within a time step interval $\tau = [t_n, t_{n+1}]$. Similar to eq. (5.2), this writes:

$$\dddot{\mathbf{q}}_n = \frac{\ddot{\mathbf{q}}_{n+1} - \ddot{\mathbf{q}}_n}{h} \tag{5.5}$$

Substitution of eq. (5.5) into eq. (5.4) produces the Newmark relations that form the basis of all Newmark integration schemes:

$$\begin{aligned} \mathbf{q}_{n+1} &= \mathbf{q}_n + h\dot{\mathbf{q}}_n + (\frac{1}{2} - \beta)h^2\ddot{\mathbf{q}}_n + \beta h^2 \ddot{\mathbf{q}}_{n+1} = \mathbf{q}^*_{n+1} + \beta h^2 \ddot{\mathbf{q}}_{n+1} \\ \dot{\mathbf{q}}_{n+1} &= \dot{\mathbf{q}}_n + (1 - \gamma)h\ddot{\mathbf{q}}_n + \gamma h \ddot{\mathbf{q}}_{n+1} = \dot{\mathbf{q}}^*_{n+1} + \gamma h \ddot{\mathbf{q}}_{n+1} \end{aligned} \tag{5.6}$$

where the vectors denoted with an asterisk are called *predictors*, which can be computed with information from previous time steps only. Hence at time t_{n+1}, the predictor values are known and can be used to start the integration for the current time step. The expressions in eq. (5.6) are substituted into the equations of motion, eq. (5.1), written at time t_{n+1} and solved for $\ddot{\mathbf{q}}_{n+1}$:

$$\mathbf{S}\ddot{\mathbf{q}}_{n+1} = \mathbf{p}_{n+1} - \mathbf{C}\dot{\mathbf{q}}^*_{n+1} - \mathbf{K}\mathbf{q}^*_{n+1} \tag{5.7}$$

where the effective stiffness matrix $\mathbf{S}$ is defined as follows:

$$\mathbf{S} = \mathbf{M} + \gamma h \mathbf{C} + \beta h^2 \mathbf{K} \tag{5.8}$$

By using a constant time step, $\mathbf{S}$ is constant and thus needs to be factorised only once. In order to start the iteration scheme, initial conditions need to be specified. Usually, one knows the boundary conditions at time t_0; $\mathbf{q}_0$ and $\dot{\mathbf{q}}_0$. The initial accelerations are then calculated from eq. (5.1) at the initial time.

5.3 The Newmark method for nonlinear dynamics

The basics of direct integration method for nonlinear problems are the same as for linear problems (see section 5.2). This research copes with geometric nonlinearities, but the Newmark scheme derived in this section can be used for systems with material nonlinearities as well. Let

us rewrite the nonlinear equilibrium equations in terms of displacements, at time $t = t_{n+1}$. Introducing the residual vector $\mathbf{r}$ gives

$$\mathbf{r}(\mathbf{q}_{n+1}) = \mathbf{M}\ddot{\mathbf{q}}_{n+1} + \mathbf{C}\dot{\mathbf{q}}_{n+1} + \mathbf{f}(\mathbf{q}_{n+1}) - \mathbf{p}_{n+1} = \mathbf{0} \tag{5.9}$$

The principle of Newmark's nonlinear time integration scheme is iteratively satisfying this expression, i.e. vanishing the residual. The integration relations that were introduced for linear analysis in eq. (5.6) may be rewritten as follows:

$$\begin{aligned} \ddot{\mathbf{q}}_{n+1} &= \frac{1}{\beta h^2}(\mathbf{q}_{n+1} - \mathbf{q}^*_{n+1}) \\ \dot{\mathbf{q}}_{n+1} &= \dot{\mathbf{q}}^*_{n+1} + \frac{\gamma}{\beta h}(\mathbf{q}_{n+1} - \mathbf{q}^*_{n+1}) \end{aligned} \tag{5.10}$$

where, by setting $\ddot{\mathbf{q}}_{n+1} = \mathbf{0}$, the predictors are

$$\begin{aligned} \mathbf{q}^*_{n+1} &= \mathbf{q}_n + h\dot{\mathbf{q}}_n + \beta h^2 \ddot{\mathbf{q}}_n \\ \dot{\mathbf{q}}^*_{n+1} &= \dot{\mathbf{q}}_n + \gamma h \ddot{\mathbf{q}}_n \end{aligned} \tag{5.11}$$

Substitution of eqs. (5.10) and (5.11) into eq. (5.9) results in an expression for the residual vector in terms of displacements only. This equilibrium problem is of nonlinear nature and finding a solution is often done in an iterative way by linearisation about a working point. Using an iterative algorithm to converge towards the solution, we use superscripts to denote the iteration number; $\mathbf{q}^k_{n+1}$ represents an approximation of the solution $\mathbf{q}_{n+1}$ at the end of iteration k. This nonlinear Newmark scheme makes use of Newton-Raphson iterations; an iteration scheme found by Newton and later generalised by Raphson. In the vicinity of the last known state $\mathbf{q}^k_{n+1}$, the residual equation can be approximated with enough accuracy by the linear expression:

$$\mathbf{r}_{lin}(\mathbf{q}^{k+1}_{n+1}) = \mathbf{r}_{lin}(\mathbf{q}^k_{n+1} + \Delta\mathbf{q}^k) \approx \mathbf{r}(\mathbf{q}^k_{n+1}) + \left[\frac{\partial \mathbf{r}}{\partial \mathbf{q}}\right]_{\mathbf{q}^k_{n+1}} \Delta\mathbf{q}^k \tag{5.12}$$

where the Jacobian or effective stiffness matrix is now a function of displacements:

$$\frac{\partial \mathbf{r}}{\partial \mathbf{q}} = \mathbf{S}(\mathbf{q}) = \mathbf{M}\frac{\partial \ddot{\mathbf{q}}}{\partial \mathbf{q}} + \mathbf{C}\frac{\partial \dot{\mathbf{q}}}{\partial \mathbf{q}} + \frac{\partial \mathbf{f}(\mathbf{q})}{\partial \mathbf{q}} - \frac{\partial \mathbf{p}(t)}{\partial \mathbf{q}} \tag{5.13}$$

Using the Newmark relations in eq. (5.10), the effective stiffness matrix can be written as

$$\mathbf{S}(\mathbf{q}) = \frac{1}{\beta h^2}\mathbf{M} + \frac{\gamma}{\beta h}\mathbf{C} + \mathbf{K}^t(\mathbf{q}) \tag{5.14}$$

where $\mathbf{K}^t$ is the tangent stiffness matrix, i.e. the variation of the internal forces of the nonlinear system with respect to the displacements. Note that the tangent stiffness matrix is no longer a constant, as was the case for the stiffness in the linear Newmark scheme. Hence, the effective stiffness matrix needs to be updated during the Newton-Raphson iterations. By rewriting eq. (5.12), the fundamentals of the Newton-Raphson iterations can be shown:

$$\mathbf{S}(\mathbf{q}^{\mathbf{k}}_{\mathbf{n+1}})\Delta\mathbf{q}^k = -\mathbf{r}(\mathbf{q}^k_{n+1}) \tag{5.15}$$

By solving for $\Delta\mathbf{q}^k$, the previously calculated displacements are corrected and become

$$\mathbf{q}_{n+1}^{k+1} = \mathbf{q}_{n+1}^{k} + \Delta\mathbf{q}^k \tag{5.16}$$

Then the correction of the velocities and accelerations can be found from Newmark's relations in eq. (5.10):

$$\begin{aligned} \dot{\mathbf{q}}_{n+1}^{k+1} &= \frac{\gamma}{\beta h}\dot{\mathbf{q}}_{n+1}^{k} \\ \ddot{\mathbf{q}}_{n+1}^{k+1} &= \frac{1}{\beta h^2}\ddot{\mathbf{q}}_{n+1}^{k} \end{aligned} \tag{5.17}$$

The correction calculations are continued until a certain convergence criterion is met. In structural mechanics, this criterion is mostly a measure of forces or displacements. In this research, we use

$$\varepsilon = \left\| \mathbf{r}(\mathbf{q}_{n+1}^{k}) \right\| / \left\| \mathbf{p}(t_{n+1}) \right\| \tag{5.18}$$

To start the integration process, initial displacements and velocities are assumed to be known. The initial accelerations are computed similarly to the linear Newmark scheme.

Two remarks on the implementation of nonlinear time integration schemes in present research should be made:

- The evaluation of the nonlinear stiffness and internal forces is done in the physical domain. The modal displacements $\mathbf{q}$ are first mapped back to the physical domain through the modal basis $\mathbf{R}$ (see eq. (3.1)). Then the nonlinear components are assembled in the physical domain, after which they are mapped to the modal domain by means of eq. (3.5). The evaluation of the nonlinear components can be done in the modal domain as well, which is described in [35]. This would be more efficient, as the model order would remain low even during the evaluation of the nonlinear components.

- The tangent stiffness matrix or tangent operator in eq. (5.14) does not have to be exact; an approximation can also converge to the solution but it may take more operations. When using the *modified Newton-Raphson method*, the initial tangent stiffness matrix is taken throughout the entire iteration procedure. This saves time on the assembly and factorization of the matrix, but the price to pay is slower convergence. It is up to the engineers expertise to chose the best method for the considered problem.

5.4 Direct integration using substructuring

Newton-Raphson iterations are needed to converge to a solution for the nonlinear DOFs, as discussed in section 5.3. For linear systems these iterations are not needed (see section 5.2); only one iteration is sufficient since the load-displacement relations are linear. Hence, applying a full nonlinear time integration scheme on a system where the nonlinearities are present only locally would be inefficient. In 1981, Bathe proposed a substructuring technique where the linear DOFs are condensed prior to the equilibrium iterations [3]. Then, the costly equilibrium iterations need only be performed on the nonlinear DOFs. In this research, this method is combined with Model Order Reduction to further decrease the order of the system on which equilibrium iterations are performed.

The stiffness matrix and internal force vector of a locally nonlinear system can be partitioned as follows:

$$\mathbf{K} = \begin{bmatrix} \mathbf{K}^l_{cc} & \mathbf{K}^l_{rc} \\ \mathbf{K}^l_{rc} & \mathbf{K}^l_{rr} \end{bmatrix} + \begin{bmatrix} \mathbf{0} & \mathbf{0} \\ \mathbf{0} & \mathbf{K}^{nl}(\mathbf{q}^k_{n+1}) \end{bmatrix} \qquad \mathbf{f} = \begin{bmatrix} \mathbf{K}^l_{cc} & \mathbf{K}^l_{rc} \\ \mathbf{K}^l_{rc} & \mathbf{K}^l_{rr} \end{bmatrix} \begin{bmatrix} \mathbf{q}_c \\ \mathbf{q}_r \end{bmatrix} + \begin{bmatrix} \mathbf{0} \\ \mathbf{f}^{nl}(\mathbf{q}^k_{n+1}) \end{bmatrix} \tag{5.19}$$

where $\mathbf{K}^l$ and $\mathbf{K}^{nl}$ denote the linear and nonlinear contributions to the stiffness matrix. The subscripts c and r denote condensed and retained DOFs, respectively. The condensed DOFs correspond to linear elements and the retained DOFs correspond to nonlinear elements[1]. For this substructuring technique, the Newmark scheme for full nonlinear analysis is used as a basis (see section 5.3). The Newmark integration relations introduced in eq. (5.10), together with the predictors given in eq. (5.11), will be used. The linear degrees of freedom are condensed prior to the integration. For successful implementation, the residual vector needs to be rewritten in terms of displacements only. This is done by substituting eq. (5.10) into eq. (5.9). After rearranging the terms, we obtain:

$$\mathbf{r}(\mathbf{q}^k_{n+1}) = \hat{\mathbf{f}}(\mathbf{q}^k_{n+1}) - \mathbf{r}^*(\mathbf{q}_n) - \mathbf{p}_{n+1} \tag{5.20}$$

where

$$\hat{\mathbf{f}}(\mathbf{q}^k_{n+1}) = \mathbf{f}^{nl}(\mathbf{q}^k_{n+1}) + \left(\frac{1}{\beta h^2}\mathbf{M} + \frac{\gamma}{\beta h}\mathbf{C} + \mathbf{K}^l \right) \mathbf{q}^k_{n+1} \tag{5.21}$$

$$\mathbf{r}^*(\mathbf{q}_n) = \frac{1}{\beta h^2}\mathbf{M}\mathbf{q}^*_{n+1} + \mathbf{C}\left(\frac{\gamma}{\beta h}\mathbf{q}^*_{n+1} - \dot{\mathbf{q}}^*_{n+1} \right) \tag{5.22}$$

In this expression $\hat{\mathbf{f}}$ can be interpreted as the *effective internal force vector*, depending merely on displacements $\mathbf{q}^k_{n+1}$. As the notation implies, $\mathbf{r}^*$ is the part of the residual that is a function of the predictor $\mathbf{q}^*_{n+1}$. The effective stiffness matrix is defined similar to eq. (5.14), namely the variation of the residual with respect to the displacements. Again using the fact that the stiffness matrix consists of a linear and a nonlinear part, we can write:

$$\left[\frac{\partial \mathbf{r}}{\partial \mathbf{q}} \right]_{\mathbf{q}^k_{n+1}} = \frac{1}{\beta h^2}\mathbf{M} + \frac{\gamma}{\beta h}\mathbf{C} + \mathbf{K}^l + \mathbf{K}^{nl}(\mathbf{q}^k_{n+1}) = \hat{\mathbf{S}} + \mathbf{K}^{nl}(\mathbf{q}^k_{n+1}) \tag{5.23}$$

The linear effective stiffness matrix $\hat{\mathbf{S}}$ is a constant matrix that only needs to be computed and factorised once prior to the time integration, given a constant time step h. Combining all gathered expressions in this section the fundamental equation of the Newton-Raphson iterations, eq. (5.15), can be rewritten

$$\left(\hat{\mathbf{S}} + \mathbf{K}^{nl}(\mathbf{q}^{\mathbf{k}}_{\mathbf{n+1}}) \right) \Delta \mathbf{q}^k = -\hat{\mathbf{f}}(\mathbf{q}^k_{n+1}) + \mathbf{r}^*(\mathbf{q}_n) + \mathbf{p}_{n+1} \tag{5.24}$$

From now on, dependencies between brackets will be omitted. In order to condense the linear DOFs we write eq. (5.24) in matrix form, where we distinguish components corresponding to linear and nonlinear DOFs similar to eq. (5.19):

$$\left(\begin{bmatrix} \hat{\mathbf{S}}_{cc} & \hat{\mathbf{S}}_{cr} \\ \hat{\mathbf{S}}_{rc} & \hat{\mathbf{S}}_{rr} \end{bmatrix} + \begin{bmatrix} \mathbf{0} & \mathbf{0} \\ \mathbf{0} & \mathbf{K}^{nl} \end{bmatrix} \right) \begin{bmatrix} \Delta \mathbf{q}^k_c \\ \Delta \mathbf{q}^k_r \end{bmatrix} = - \begin{bmatrix} \hat{\mathbf{f}}_c \\ \hat{\mathbf{f}}_r \end{bmatrix} + \begin{bmatrix} \mathbf{r}^*_c \\ \mathbf{r}^*_r \end{bmatrix} + \begin{bmatrix} \mathbf{p}_c \\ \mathbf{p}_r \end{bmatrix} \tag{5.25}$$

[1] If a DOF is part of a node that corresponds to both a linear and a nonlinear element, the DOF is treated as being nonlinear; it will be partitioned in the vector $\mathbf{q}_r$

Performing condensation on this system of equations involves solving the first rule in eq. (5.25) for $\Delta\mathbf{q}_c^k$ and substituting the result in the bottom line. This gives

$$\left(\hat{\mathbf{S}}_s + \mathbf{K}^{nl}\right)\Delta\mathbf{q}_r^k = \mathbf{r}_{cond}^* + \mathbf{p}_{cond} - \left(\hat{\mathbf{f}}_r - \hat{\mathbf{S}}_{rc}\hat{\mathbf{S}}_{cc}^{-1}\hat{\mathbf{f}}_c\right) \tag{5.26}$$

where

$$\mathbf{r}_{cond}^* = \mathbf{r}_r^* - \mathbf{S}_{rc}\mathbf{S}_{cc}^{-1}\mathbf{r}_c^* \tag{5.27}$$

$$\mathbf{p}_{cond} = \mathbf{p}_r - \mathbf{S}_{rc}\mathbf{S}_{cc}^{-1}\mathbf{p}_c \tag{5.28}$$

Here, $\hat{\mathbf{S}}_s$ represents the Schur complement[2] of the linear effective stiffness matrix $\hat{\mathbf{S}}$. In case of a constant time step h, $\hat{\mathbf{S}}_{cc}$ needs to be factorised only once prior to the integration. The term between brackets in the right-hand side of eq. (5.26) is interpreted as the effective internal force of the condensed system; $\hat{\mathbf{f}}_r$ represents the effective internal forces acting on the retained DOFs and $\hat{\mathbf{S}}_{rc}\hat{\mathbf{S}}_{cc}^{-1}\hat{\mathbf{f}}_c$ represent the forces from the condensed DOFs acting on the retained DOFs. The latter term still contains information about the condensed DOFs, namely the term $\hat{\mathbf{f}}_c$ which is a function of $\mathbf{q}_c$. Hence, in order to solve eq. (5.26) the full set of DOFs need to be evaluated and this is inefficient. In order to find a new expression for $\hat{\mathbf{f}}_c$, we perform condensation on its definition (eq. (5.21)). The internal forces due to element stresses originate from both the linear and the nonlinear properties of the model. Therefore, eq. (5.21) can also be written as

$$\begin{bmatrix}\hat{\mathbf{f}}_c \\ \hat{\mathbf{f}}_r\end{bmatrix} = \begin{bmatrix}\hat{\mathbf{S}}_{cc} & \hat{\mathbf{S}}_{cr} \\ \hat{\mathbf{S}}_{rc} & \hat{\mathbf{S}}_{rr}\end{bmatrix}\begin{bmatrix}\mathbf{q}_c \\ \mathbf{q}_r\end{bmatrix} + \begin{bmatrix}\mathbf{0} \\ \mathbf{f}_r^{nl}\end{bmatrix} \tag{5.29}$$

Static condensation of this expression gives

$$\hat{\mathbf{f}}_r - \hat{\mathbf{S}}_{rc}\hat{\mathbf{S}}_{cc}^{-1}\hat{\mathbf{f}}_c = \hat{\mathbf{S}}_s\mathbf{q}_r + \mathbf{f}_r^{nl} \tag{5.30}$$

Here, the left hand side is equal to the last term in eq. (5.26) and we can therefore substitute this into the equilibrium equations

$$\left(\hat{\mathbf{S}}_s + \mathbf{K}^{nl}\right)\Delta\mathbf{q}_r^k = \mathbf{r}_{cond}^* + \mathbf{p}_{cond} - \left(\hat{\mathbf{S}}_s\mathbf{q}_r + \mathbf{f}_r^{nl}\right) \tag{5.31}$$

From eq. (5.22) it follows that $\mathbf{r}_{cond}^*$ only needs to be computed once at the beginning of a time step, prior to the equilibrium equations. The external load is assumed to be known, such that $\mathbf{p}_{cond}$ also only needs to be computed once per time step. The solution for $\mathbf{q}_{n+1}^{k+1} = \mathbf{q}_{n+1}$ is found only for the retained degrees of freedom $\mathbf{q}_r$. Once the Newton-Raphson procedure has converged, we obtain the displacements of the linear DOFs $\mathbf{q}_c$ using the first set of equations in eq. (5.25) together with definitions eq. (5.21) and eq. (5.16):

$$\mathbf{q}_c = \hat{\mathbf{S}}_{cc}^{-1}\left(\mathbf{p}_c + \mathbf{r}_c^* - \hat{\mathbf{S}}_{cr}\mathbf{q}_r\right) \tag{5.32}$$

With the full displacement vector at time t_{n+1} known, the corresponding velocities and accelerations are calculated using the Newmark relations in eq. (5.10). The presented substructuring integration scheme is summarised in table 5.1.

[2]The Schur complement is defined as $\hat{\mathbf{S}}_s = \hat{\mathbf{S}}_{rr} - \hat{\mathbf{S}}_{rc}\hat{\mathbf{S}}_{cc}^{-1}\mathbf{S}_{cr}$

Table 5.1: *Implicit Newmark integration scheme using substructuring for analysis of systems with local nonlinearities.*

	Given $\mathbf{q}_0, \dot{\mathbf{q}}_0$
1	Compute initial accelerations: $\ddot{\mathbf{q}}_0 = \mathbf{M}^{-1}\left(\mathbf{p}_0 - \mathbf{K}^l\mathbf{q}_0 - \mathbf{f}^{nl}(\mathbf{q}_0) - \mathbf{C}\dot{\mathbf{q}}_0\right)$
2	Compute linear effective stiffness: $\hat{\mathbf{S}} = \frac{1}{\beta h^2}\mathbf{M} + \frac{\gamma}{\beta h}\mathbf{C} + \mathbf{K}^l$
3	Time incrementation: $t_{n+1} = t_n + h$
4	Set iteration counter $k = 0$
5	Prediction: $\mathbf{q}_{n+1}^0 = \mathbf{q}_n + h\dot{\mathbf{q}}_n + \beta h^2\ddot{\mathbf{q}}_n$ $\dot{\mathbf{q}}_{n+1}^0 = \dot{\mathbf{q}}_n + \gamma h\ddot{\mathbf{q}}_n$
6	Prediction/time step dependent residual components: $\mathbf{r}^* = \frac{1}{\beta h^2}\mathbf{M}\mathbf{q}_{n+1}^0 + \mathbf{C}\left(\frac{\gamma}{\beta h}\mathbf{q}_{n+1}^0 - \dot{\mathbf{q}}_{n+1}^0\right)$
7	Residual evaluation: $\mathbf{r}(\mathbf{q}_{n+1}^k) = \mathbf{r}_r^* - \hat{\mathbf{S}}_{rc}\hat{\mathbf{S}}_{cc}^{-1}\mathbf{r}_c^* + \mathbf{p}_r - \hat{\mathbf{S}}_{rc}\hat{\mathbf{S}}_{cc}^{-1}\mathbf{p}_c - \hat{\mathbf{S}}_s\mathbf{q}_r^k - \mathbf{f}_r^{nl}$ If $\mathbf{r}(\mathbf{q}_{n+1}^k)$ satisfies the convergence criterion, go to step 11. Otherwise continue.
8	Calculate displacements correction: $\left(\hat{\mathbf{S}}_s + \mathbf{K}^{nl}\right)\Delta\mathbf{q}_r^k = \mathbf{r}(\mathbf{q}_{n+1}^k)$
9	Correct displacements: $\mathbf{q}_{n+1,r}^{k+1} = \mathbf{q}_{n+1,r}^k + \Delta\mathbf{q}_r^k$
10	Set $k = k + 1$ and go to step 7.
11	Compute condensed displacements: $\mathbf{q}_{n+1,c} = \hat{\mathbf{S}}_{cc}^{-1}\left(\mathbf{p}_c + \mathbf{r}_c^* - \hat{\mathbf{S}}_{cr}\mathbf{q}_{n+1,r}\right)$
12	Compute velocities and accelerations: $\ddot{\mathbf{q}}_{n+1} = \frac{1}{\beta h^2}\mathbf{q}_{n+1} - \frac{1}{\beta h^2}\mathbf{q}_{n+1}^0$ $\dot{\mathbf{q}}_{n+1} = \frac{\gamma}{\beta h}\mathbf{q}_{n+1} - \frac{\gamma}{\beta h}\mathbf{q}_{n+1}^0 + \dot{\mathbf{q}}_{n+1}^0$ Set $n = n + 1$ and go to step 3.

6 Model validation

In order to validate the finite element code written in MATLAB, a simple model is built and compared with analytically computed results. Using the shell elements that are briefly described in appendix A, a plate with simply supported boundary conditions on each side is modelled. For this purpose a simply supported plate model is taken, as the eigenfrequencies and corresponding modes of such a system can be computed analytically as well. The length of the model is 400 mm, width 200 mm and thickness 0.8 mm. These dimensions ensure that the model can be treated as being *thin-walled*. The material properties are $E = 70\,\text{GPa}$, $\rho = 2700\,\text{kg}\,\text{m}^{-3}$ and $\nu = 0.3$.

6.1 Analytical solutions of simple plate model

Analytical solutions of free vibration of rectangular plates with various boundary conditions are well known, see [25, 28] for instance. In this thesis, the MATLAB Finite Element code is compared to the analytical solution of a full simply supported plate. Said boundary conditions are chosen because it leads to the simplest and clearest eigenfrequency formula. A rectangular plate with dimensions $a \times b$ in the (x, y)-plane is considered (in this case $a = 400\,\text{mm}$ and $b = 200\,\text{mm}$).

The analytical formula assumes isotropic material and *Kirchhoff plates*. Kirchhoff's theory states that a straight line normal to the midplane remains straight and normal to the midplane in the deformed state. This is similar to the Bernouilli beam theory. Membrane strains are neglected, which is valid when studying small vibrations since membrane strains contain nonlinear contributions. Omitting proof, the governing free vibration equations are

$$m\ddot{w} + D\nabla^2\nabla^2 w = 0 \tag{6.1}$$

where $w = w(x, y, t)$ are the out-of-plane displacements. The flexural rigidity D of the plate is defined by

$$D = \frac{Eh^3}{12(1-\nu^2)} \tag{6.2}$$

Next, the displacement field is decomposed in the form

$$w(x, y, t) = W(x, y)F(t) \tag{6.3}$$

Since all four boundaries are simply supported, two conditions need to be satisfied:

1. No vertical displacement on the boundaries
2. No bending moments, i.e. the slope normal to the boundary must be zero.

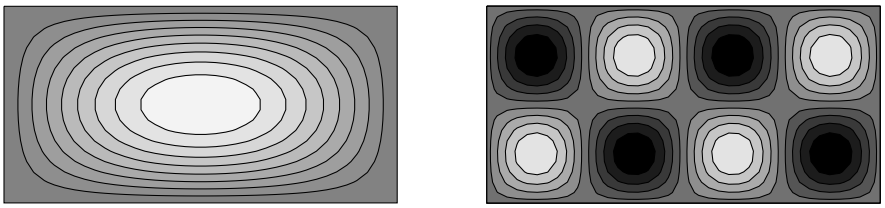

(a) $m = 1$, $n = 1$ **(b)** $m = 4$, $n = 2$

Figure 6.1: *Illustration of wavenumbers m and n in a contour plot of W_{mn} (eq. (6.5)), corresponding to the modeshapes of a simply supported plate. Black and white areas illustrate a (normalised) out-of-plane displacement of -1 and $+1$, respectively.*

Table 6.1: *Analytically computed eigenfrequencies ω_{mn} of a full simply supported rectangular plate. Units are* $\mathrm{rad\,s^{-1}}$.

		n				
		1	2	3	4	5
	1	380.2	1292.6	2813.4	4942.4	7679.7
	2	608.3	1520.7	3041.5	5170.5	7907.9
m	3	988.5	1901.0	3421.7	5550.7	8288.0
	4	1520.7	2433.2	3953.9	6083.0	8820.3
	5	2205.1	3117.5	4638.3	6767.3	9504.6

For the considered rectangular plate, this can be translated into

$$W(x=0,a)=0 \qquad W(y=0,b)=0 \qquad \frac{\partial^2 W(x=0,a)}{\partial x^2}=0 \qquad \frac{\partial^2 W(y=0,b)}{\partial y^2}=0 \tag{6.4}$$

Using these conditions and again omitting proof, the general form of the eigenmodes is

$$W_{mn}(x,y)=\sin\frac{m\pi x}{a}\sin\frac{n\pi y}{b} \qquad \text{for } m,n=1,2,\ldots \tag{6.5}$$

where m and n represent the wavenumber in x and y directions, respectively. Two arbitrary modeshapes are given in fig. 6.1. The corresponding eigenfrequencies are given by

$$\omega_{mn}=\pi^2\sqrt{\frac{D}{\rho t}}\left[\left(\frac{m}{a}\right)^2+\left(\frac{n}{b}\right)^2\right] \tag{6.6}$$

We can analytically compute the eigenfrequecies using eq. (6.6). The results for the first few eigenfrequencies are given in table 6.1.

6.2 Finite element solutions of simple plate model

Figure 6.2 displays the first five modeshapes and their corresponding frequencies, found with the MATLAB FE model of the simply supported plate. Geometry and material properties are

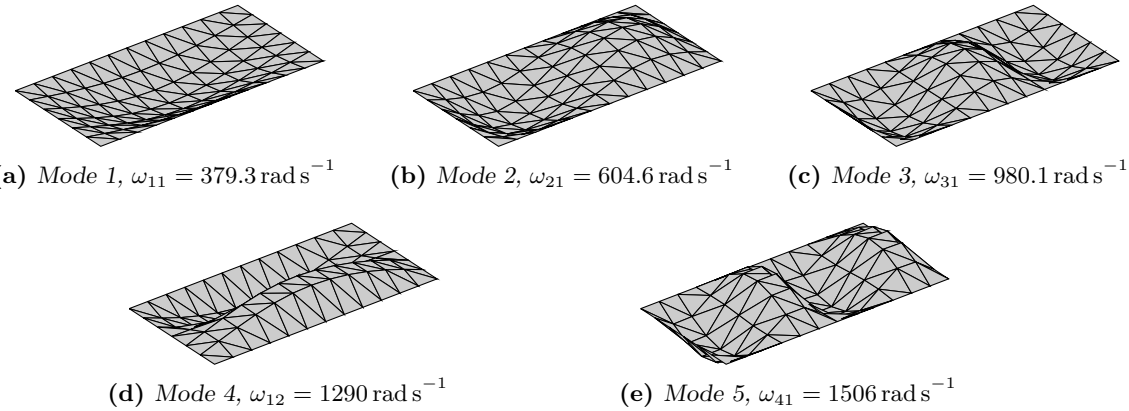

(a) *Mode 1,* $\omega_{11} = 379.3\,\mathrm{rad\,s^{-1}}$ **(b)** *Mode 2,* $\omega_{21} = 604.6\,\mathrm{rad\,s^{-1}}$ **(c)** *Mode 3,* $\omega_{31} = 980.1\,\mathrm{rad\,s^{-1}}$

(d) *Mode 4,* $\omega_{12} = 1290\,\mathrm{rad\,s^{-1}}$ **(e)** *Mode 5,* $\omega_{41} = 1506\,\mathrm{rad\,s^{-1}}$

Figure 6.2: *First five eigenmodes and their corresponding frequencies from the simply supported FE plate model.*

Table 6.2: *Comparison of eigenfrequencies* ω_{mn} *of a full simply supported rectangular plate, obtained both analytically and numerically.*

	ω_{mn}	Analytical ($\mathrm{rad\,s^{-1}}$)	FE ($\mathrm{rad\,s^{-1}}$)	Relative error $\Delta\omega$ (%)
1	ω_{11}	380.2	379.3	0.24
2	ω_{21}	608.3	604.6	0.61
3	ω_{31}	988.5	980.1	0.85
4	ω_{12}	1293	1290	0.20
5	ω_{41}	1521	1506	0.99

identical to those used in the analytical model. A comparison of the eigenfrequencies is done for the validation of the MATLAB code. By counting the number of waves is x and y direction in fig. 6.2, the numerically computed frequencies ω_{mn} may be determined. As can be seen, the first five eigenfrequencies are: ω_{11}, ω_{21}, ω_{31}, ω_{12} and ω_{41}. This sequence is expected as, due to the width/length ratio, the plate is stiffer in the width direction.

Comparing the analytically obtained frequencies listed in table 6.1 with those from the FE model is summarised in table 6.2. The relative frequency error $\Delta\omega$ is defined as:

$$\Delta\omega = \left| \frac{\omega_b - \omega_a}{\omega_b} \right| \cdot 100\% \tag{6.7}$$

where ω_b is the reference value, in this case the analytically computed frequency.

From table 6.2 it can be seen that the error increases with increasing wavenumber. This is caused by the finite element discretisation; as can be seen in the mode plots of the FE model (especially fig. 6.2e), the mode shape is not smooth any more due to the relatively coarse mesh. Nonetheless, the error $\Delta\omega$ remains small ($< 1\%$) for all compared frequencies. It is therefore concluded that the finite element code written in MATLAB is correctly describing the mechanical behaviour of thin-walled plate structures.

7 Application of nonlinear reduction methods

This chapter contains results and interpretations of response analyses of various simple FE models and one larger model on which the presented Component Mode Synthesis methods are applied. The models may contain both linearly and nonlinearly behaving components, such that the nonlinear Craig-Bampton and Rubin reduction methods described in sections 4.5 and 4.6 can be tested. The simple models, analysed in section 7.1, are designed such that the results will give insight in which reduction method can best be used in several cases. The larger FE model, see section 7.2, is of a highly flexible wing concept. Due to a large number of DOFs a nonlinear response analysis on this model is computationally heavy. Therefore, the application of CMS on this model is highly welcomed.

7.1 Numerical examples

In order to successfully perform the Component Mode Synthesis methods described in this thesis, several model requirements have been set up. First, in order to allow substructuring, multiple distinguishable components need to be present. Also, at least one component needs to be flexible enough such that the deformations, in combination with a given external load, will no longer be described by linear elasticity. Lastly, if one of the substructures is designed to behave linearly elastic it should be verified prior to the nonlinear analyses. Based on these requirements a parametric model is designed, consisting of two substructures, where the thickness of both substructures can be varied. The model is sketched in fig. 7.1a and the corresponding FE mesh is given in fig. 7.1b. The shell elements described in appendix A are used and the thickness is varied to simulate geometrically linear or nonlinear components. The model has a total number of 546 DOFs; 42 boundary DOFs and 504 internal DOFs. As was mentioned in chapter 3, the MOR step is applied to the internal DOFs only, i.e. a small set of vibration component modes (section 3.3) will be used to approximate the dynamic behaviour of all 504 internal DOFs.

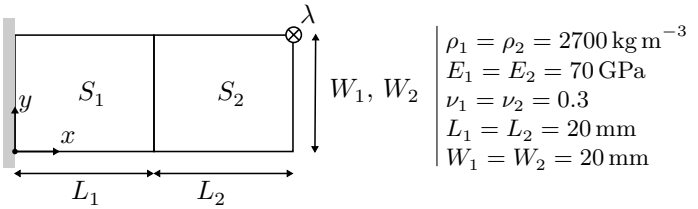

(a) *Model and material*

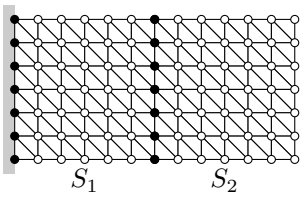

(b) *Mesh size*

Figure 7.1: *Sketch of the tested numerical example with corresponding material properties and mesh size. A load in z-direction with amplitude λ is applied on the indicated tip node. Black dots indicate boundary nodes, white dots indicate internal nodes.*

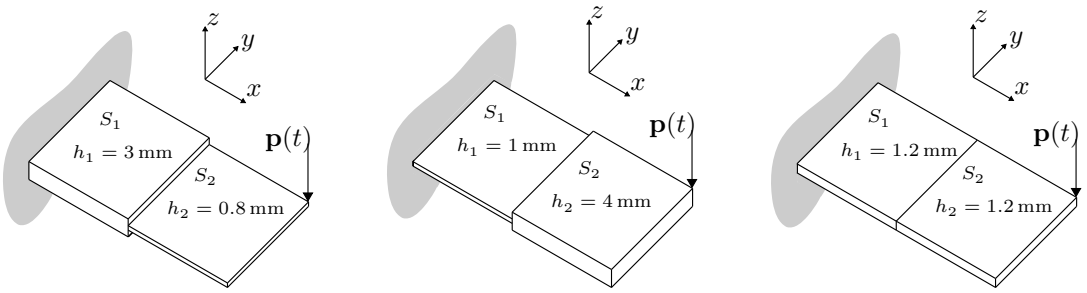

(a) `model1` **(b)** `model2` **(c)** `model3`

Figure 7.2: *Three analysed variants of the model in fig. 7.1, obtained by varying the substructure thicknesses.*

Three different models are created by varying the thicknesses of the two substructures:

Model 1 As sketched in fig. 7.2a, this model has a thick component near the clamped base and a thin part at the end. It is assumed, and later verified, that the thick part behaves linearly as it only slightly deforms. This model will be referred to as `model1`. Two load cases will be studied for `model1`; a step load $\mathbf{p}(t) = \lambda = 70\,\mathrm{N}$ and a harmonic load $\mathbf{p}(t) = \lambda \cos \omega t = 100\,\mathrm{N} \cos 15\,\mathrm{kHz}$. The excitation frequency is chosen such that it is in between the first and second natural frequency of the model.

Model 2 The second model, shown in fig. 7.2b, is the inversion of `model1`; the thin substructure is now near the base and the thick component is at the end. Although the thick substructure will not be deforming a lot, it will undergo large rotations such that it still requires a geometrically nonlinear description. This model will be referred to as `model2`. For this model, only a step load with amplitude $\lambda = 50\,\mathrm{N}$ is considered.

Model 3 The third variant is shown in fig. 7.2c. Both substructures are of equal thickness such that they both need to be treated as geometrically nonlinear; substructure S_2 will undergo both large rotations and deformations. This model will be referred to as `model3`. Again, a step load applied to this model ($\lambda = 100\,\mathrm{N}$).

Lastly, it is stressed that the dynamic responses shown in the following sections are captured at the loaded tip node, in direction u_z. We refer to the response of the full model as *full* solution and the response of the reduced model as *reduced* solution.

7.1.1 Model 1 analysis

The model is designed such that the thick component S_1 can be described by linear elasticity. This is verified first, by comparison of two responses of the *full* model; one obtained with a nonlinear Newmark integration (section 5.3) and one obtained with the substructuring scheme of Bathe (section 5.4). The difference between the fully nonlinear solution and the *substructuring*

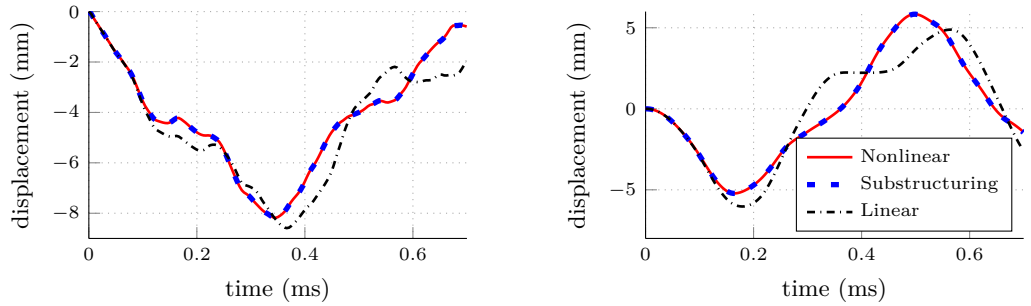

(a) *Step load* **(b)** *Harmonic load*

Figure 7.3: *Verification of assumption that S_1 in* `model1` *behaves linearly elastic, for two different load cases.*

solution may be illustrated by the following system properties:

$$\text{nonlinear:} \quad \mathbf{f}^{nl} = \begin{bmatrix} \mathbf{f}^{nl(1)} \\ \mathbf{f}^{nl(2)} \end{bmatrix}, \qquad \mathbf{K}^{nl} = \begin{bmatrix} \mathbf{K}^{nl(11)} & \mathbf{K}^{nl(21)} \\ \mathbf{K}^{nl(12)} & \mathbf{K}^{nl(22)} \end{bmatrix} \tag{7.1}$$

$$\text{substructuring:} \quad \mathbf{f}^{nl} = \begin{bmatrix} \mathbf{0} \\ \mathbf{f}^{nl(2)} \end{bmatrix}, \qquad \mathbf{K}^{nl} = \begin{bmatrix} \mathbf{0} & \mathbf{0} \\ \mathbf{0} & \mathbf{K}^{nl(22)} \end{bmatrix} \tag{7.2}$$

The matrices in eq. (7.2) contain zero block matrices for the elements that correspond to DOFs in S_1, since these are condensed and treated as linear during the substructuring integration. If S_1 indeed deforms within the linear region, the vectors and matrices in eqs. (7.1) and (7.2) are identical, since the nonlinearities corresponding to the S_1 elements will not be triggered due to the relative high stiffness of the first substructure combined with the applied load. The time responses obtained are compared in fig. 7.3. Additionally, the linear response is studied. This is done to ensure that the global model does not behave linearly, in which case the matrices in eqs. (7.1) and (7.2) would also be identical; they would all be zero. For both the step load case in fig. 7.3a and the harmonic load case in fig. 7.3b, it is concluded that only S_2 behaves nonlinearly. Hence, the substructuring time integration method presented in this contribution can effectively be subjected to `model1`.

Linear response analysis

Nonlinear dynamic analyses are performed to gain insight in the accuracy of the presented nonlinear CMS techniques, i.e. the extended Craig-Bampton and Rubin methods in sections 4.5 and 4.6, respectively. The mode selection criterion discussed in section 4.7 will be analysed as well. Let us denote the number of vibration modes in the reduction basis by M. Out of this set, a total number of $R = M(M+1)/2$ modal derivatives can be computed and an optimal set of $P < R$ modal derivatives will be taken based on the highest values for b_{ij} in eq. (4.33). Since it was found that substructure S_1 can be treated linearly, the nonlinear reduction techniques will be applied to S_2 only.

It needs to be verified that the underlying linear description of the reduced model is accurate, because the mode selection criterion is heavily based on the underlying linear dynamics. Reduced linear analyses are compared to the full solution in fig. 7.4. For both load cases and both

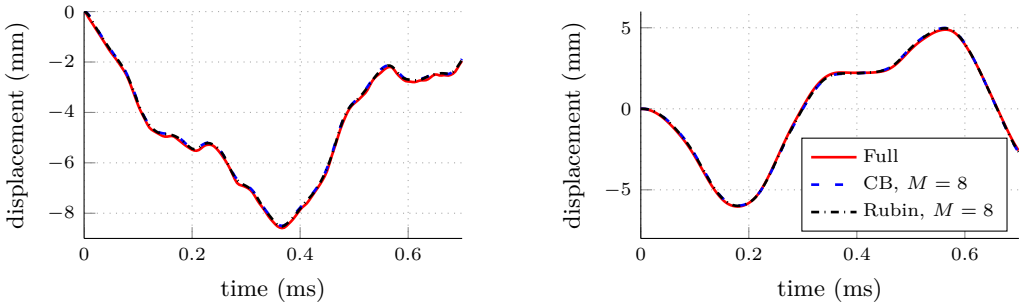

(a) *Step load* λ **(b)** *Harmonic load* $\lambda \cos \omega t$

Figure 7.4: *Linear reduced responses of* `model1` *for a step and harmonic load case, computed with both the CB and Rubin method, compared to the full linear solution.*

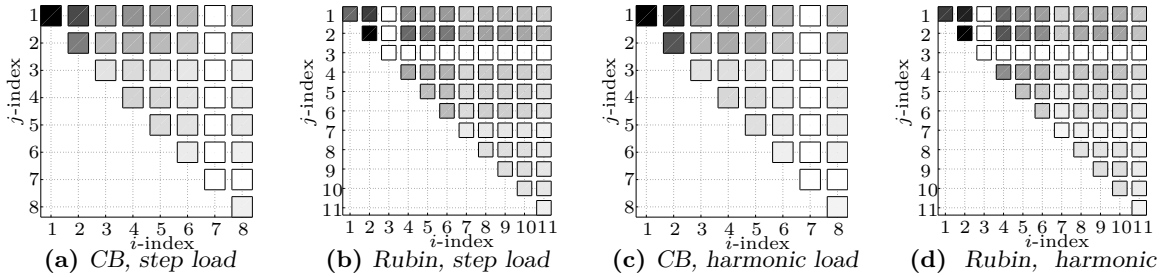

(a) *CB, step load* **(b)** *Rubin, step load* **(c)** *CB, harmonic load* **(d)** *Rubin, harmonic load*

Figure 7.5: *Mode selection coefficients for* `model1`*, raised to the power of 0.25 to better highlight the relative contribution of the terms. The lower diagonal part of the symmetric* b_{ij} *coefficients is set to zero for display purposes. Black surfaces indicate high values, white indicates zero. For (b) and (d): indices 1 to 3 indicate rotational RBMs, VM* ϕ_i *is indicated by index* $i + 3$*.*

reduction methods, it was found that a set of $M = 8$ vibration modes gave satisfying results for.

Mode selection criterion

The modal amplitudes $\boldsymbol{\eta}^{(i)}$ needed to compute the mode selection coefficients b_{ij} are obtained from the linear analyses discussed previously. For both load cases and reduction methods, the values of b_{ij} are presented in fig. 7.5. Note that although $M = 8$ vibration modes are used, the extended Rubin method also uses modal derivatives of the three rotational rigid body modes (see section 4.4). Therefore, the indices of b_{ij} go up to $8 + 3 = 11$ instead of 8; indices 1 to 3 refer to the rotational RBMs. The load case influences the coefficients only slightly. This is because both loads act on the same DOF, so approximately the same vibration modes will be excited. In the case of CB reduction, it is seen that the emphasis is on the first two modes, as well as their interaction with all the other modes. Mode 7 does not participate since it features in-plane lateral bending, a motion orthogonal to the applied loads. For the Rubin method, the contribution of the first two rigid body modes and their interaction with the rest is significant. Also, the first vibration mode (index 4) is relatively dominant. The third index in figs. 7.5b and 7.5d indicates the rotational RBM around the z-axis. This mode is orthogonal to the load,

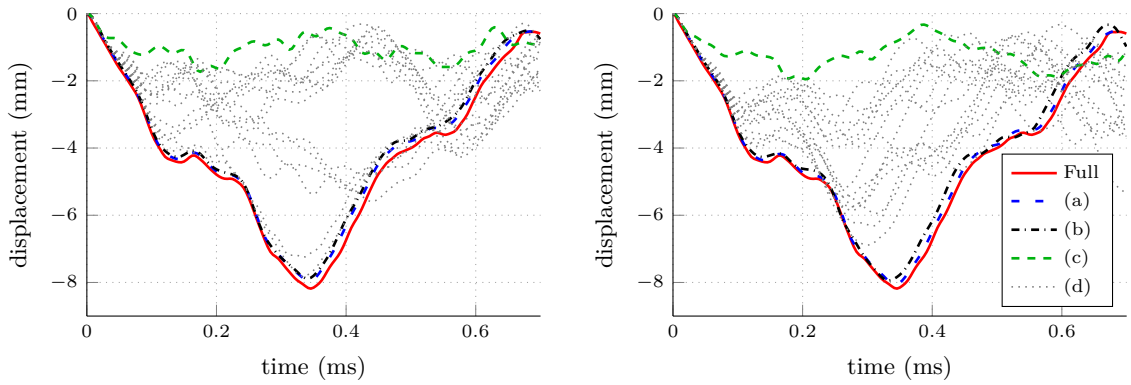

(a) *CB, step load* **(b)** *Rubin, step load*

Figure 7.6: *Nonlinear dynamic responses for a step load on* `model1`*, obtained with nonlinear CB and Rubin reduced models. MDs are only added for* S_2*. (a): basis formed with* $M = 8$ *VMs and all possible modal derivatives, i.e.* $R = 36$ *for CB and* $R = 66$ *for Rubin; (b): basis formed with* $M = 8$ *VMs and an optimal set of MDs:* $P = 14$ *for CB and* $P = 26$ *for Rubin; (c): basis formed with vibration modes only,* $M = 8, P = 0$ *for both substructures; (d): basis formed with* $M = 8$ *VMs and several random choices of* P *MDs.*

and therefore does not participate in the Rubin reduced responses.

Nonlinear response analysis

For the nonlinear response analysis, the fact that S_1 can be considered nonlinearly is exploited by applying Bathe's substructuring technique prior to the equilibrium iterations. Hence, component S_1 is first reduced with a basis of $M = 8$ vibration modes and then condensed. The nonlinear responses for the step load case are shown in fig. 7.6. The Craig-Bampton reduced model, augmented with all $R = 36$ modal derivatives, accurately describes the full response up to 0.3 ms. Thereafter the error starts to grow, but the results are still representable. Next, an optimal basis is sought for by discarding as many MDs as possible without significantly deteriorating the response. The following error measure is defined:

$$\varepsilon = \frac{\|\mathbf{u}_{red} - \mathbf{u}_{full}\|}{\|\mathbf{u}_{full}\|} \cdot 100\% \tag{7.3}$$

where $\mathbf{u}_{red} = \mathbf{R}\mathbf{q}$ is the reduced solution and $\mathbf{u}_{full}$ the full solution. A threshold of $\varepsilon \leq 5\%$ is chosen to determine the optimal basis. This basis is found by discarding one MD and checking eq. (7.3). If the error is acceptable (below 5%), another MD is discarded. This process is repeated until the optimal basis is found. The advantage of this error bound is that all DOFs are taken into account, whereas the response plots in this thesis only show one particular DOF.

Computing the error of the CB reduced response with all MDs, according to eq. (7.3), gives a value of 3.0%. The optimal basis for which the reduced solution does not exceed the error threshold of 5% is determined to include a total of $P = 14$ MDs. The corresponding response is also shown in fig. 7.6a. A total of $R - P = 14$ MDs have been discarded, without losing much accuracy. Also, a reduced analysis with the basis formed by VMs only is shown. This results in an overly stiff and poor approximation of the response; worse than the linear response.

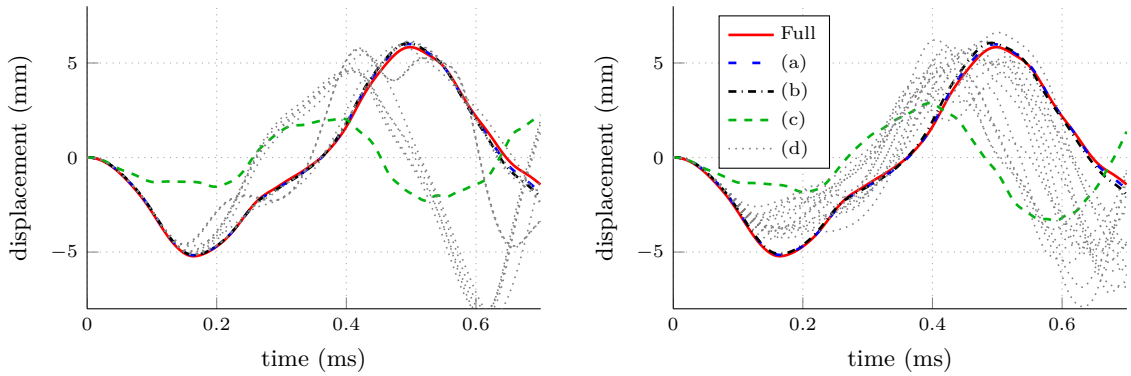

(a) *CB, harmonic load* **(b)** *Rubin, harmonic load*

Figure 7.7: *Nonlinear dynamic responses for a harmonic load on* `model1`*, obtained with nonlinear CB and Rubin reduced models. MDs are only added for* S_2*. (a): basis formed with* $M = 8$ *VMs and all possible modal derivatives, i.e.* $R = 36$ *for CB and* $R = 66$ *for Rubin; (b): basis formed with* $M = 8$ *VMs and an optimal set of MDs:* $P = 33$ *for CB and* $P = 26$ *for Rubin; (c): basis formed with vibration modes only,* $M = 8, P = 0$ *for both substructures; (d): basis formed with* $M = 8$ *VMs and several random choices of* P *MDs.*

However, it should be noted that the linear response does not show any axial contribution (only vertical displacements are shown in fig. 7.6a). Lastly, several responses obtained with randomly generated sets of $P = 14$ MDs to enrich the $M = 8$ VMs in the basis are shown. None of them approximates the response as good as the optimal set obtained with the presented selection criterion.

The reduced responses obtained with Rubin reduction bases are shown in fig. 7.6b. The nonlinear response with a basis formed with $M = 8$ VMs and all possible $R = 66$ MDs yields a better approximation of the full response than the CB response in fig. 7.6a; the error is only 1.7%. It should be noted that the Rubin response also includes MDs computed from rotational RBMs; $R = 66$ MDs can be computed whereas for the CB reduction basis only $R = 36$ MDs can be computed. Keeping the error under 5%, an optimal basis with $R = 26$ MDs is found. When adding a random selection of 26 MDs to the reduction basis, the responses are not as accurate as that of the optimal basis. Again, the mode selection criterion is able to indicate the most dominant MDs.

The harmonic load case is considered in fig. 7.7. It is seen that the deflections for this loading are around 5 mm, significantly less than for the step load. The nonlinearities, which are still present as concluded from fig. 7.3b, will therefore be weaker and it is expected that a reduction basis augmented with second-order modal derivatives will give more accurate results compared to the step load case. For both the extended CB and Rubin methods this is verified in fig. 7.7a and fig. 7.7b, respectively. The Craig-Bampton reduced model, with all possible $P = 36$ MDs included in the reduction basis, follows the full response closely ($\varepsilon = 3.3\%$). The same is observed for the Rubin reduced model; when all $P = 66$ MDs are added, the response is in good agreement with the full nonlinear solution ($\varepsilon = 1.4\%$). As for the step load, for the harmonic load case an optimal basis is sought as well. For Craig-Bampton, it is found that only 3 MDs can be discarded to keep the error $\varepsilon \leq 5\%$. In the nonlinear Rubin basis, 40 MDs can be discarded such that 26 MDs remain in the optimal basis. For both methods, the models with randomly selected MDs are less accurate than the optimal response.

Table 7.1: *Computation times of the different analyses on* `model1`*. The full model is compared to nonlinear Craig-Bampton and Rubin reduced models; one with all possible MDs in the basis and one with an optimal set of P MDs. Also, Bathe's substructuring scheme is analysed.*

(a) *Step load*

Analysis	DOFs	time (s)
Full	546	82.0
CB ($M = 8, R = 36$)	136	25.6
CB ($M = 8, P = 14$)	114	21.5
Rubin ($M = 8, R = 66$)	178	27.8
Rubin ($M = 8, P = 26$)	138	26.4
Bathe (S_1 linear)	546	29.9

(b) *Harmonic load*

Analysis	DOFs	time (s)
Full	546	80.6
CB ($M = 8, R = 36$)	136	20.5
CB ($M = 8, P = 33$)	133	19.2
Rubin ($M = 8, R = 66$)	178	22.5
Rubin ($M = 8, P = 26$)	138	18.1
Bathe (S_1 linear)	546	30.1

The computational efforts of the considered nonlinear response analyses are listed in table 7.1 for both load cases. Additionally, the substructuring technique developed by Bathe and described in section 5.4 is listed. It is seen, by comparing the full nonlinear analysis to Bathe's substructuring technique, that most savings come from the fact that the linear DOFs of S_1 are condensed prior to the equilibrium iterations. The Model Order Reduction of CB and Rubin reduce the computational efforts slightly more, but the savings are only minimal because the reduction in DOFs is rather small. A similar observation is done when comparing the modal bases with all possible MDs to the bases formed by the optimal set of P MDs; the order reduction between these cases is too small to influence the computation time significantly.

7.1.2 Model 2 analysis

The component close to the clamped base, S_1, is thin such that it will undergo large deformations and thus needs to be described nonlinearly. Substructure S_2 is relatively thick and will therefore hardly deform under the specified load conditions. However, since it's located at the end and attached to the flexible S_1 it will undergo large rotations. Therefore, this substructure needs to be considered nonlinearly as well. The substructuring technique proposed by Bathe, see section 5.4, will be exactly equal to a full nonlinear time integration since there are no linear DOFs to be condensed.

Linear response analysis

Linear responses as a result from the applied step load are shown in fig. 7.8; the full linear solution is compared to a CB and Rubin reduced response. The number of vibration modes in the reduction bases are carefully selected such that it includes the fewest number of modes needed to describe the full response. For both Craig-Bampton and Rubin, $M = 4$ vibration modes are needed.

Mode selection criterion

The modal amplitudes obtained with the linear analyses have been processed according to eq. (4.33) to find the b_{ij} coefficients. The results for both reduction techniques are illustrated in fig. 7.9. For both substructures, the 4 VMs of the Craig-Bampton reduction basis result in $R = 10$ unique MDs. From fig. 7.9a it seems that the fourth VM in the CB reduction basis, the

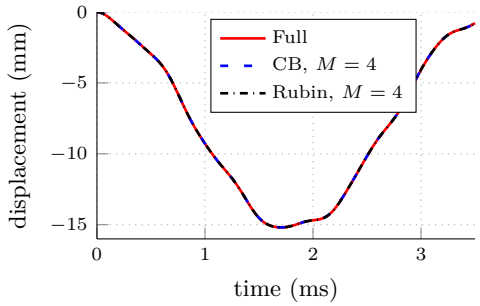

Figure 7.8: *Linear reduced responses of* `model2` *for a step load, computed with both the CB and Rubin method, compared to the full linear solution.*

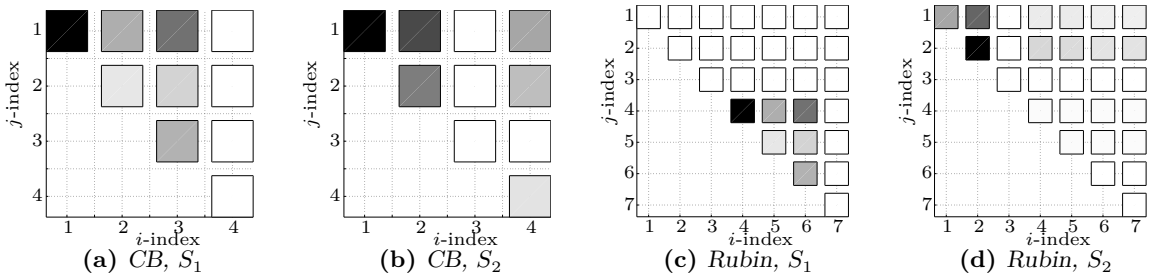

(a) *CB,* S_1 **(b)** *CB,* S_2 **(c)** *Rubin,* S_1 **(d)** *Rubin,* S_2

Figure 7.9: *Mode selection coefficients for* `model2`*, raised to the power of 0.25 to better highlight the relative contribution of the terms. The lower diagonal part of the symmetric* b_{ij} *coefficients is set to zero for display purposes. Black surfaces indicate high values, white indicates zero. For (c) and (d): indices 1 to 3 indicate rotational RBMs, VM* ϕ_i *is indicated by index* $i + 3$*.*

second bending mode, is not participating in the response. However it is found that although the participation is small, it's not (numerically) zero. The third mode in S_2 represents in-plane lateral bending, which is orthogonal to the applied load and therefore produces numerically zero b_{ij} coefficients (see fig. 7.9b).

The Rubin method includes $M = 4$ VMs as well as 3 rotational RBMs from which modal derivatives can be computed. Hence, a total number of $R = 28$ MDs can be computed. Analyzing the b_{ij} coefficients for S_1 in fig. 7.9c, it is found that the first VM (index 4) is dominant. This mode describes symmetric torsion about both x and y axes. The edges, i.e. the interface nodes, remain in a straight line whereas the interface deflects for the other 3 vibration modes in the reduction basis. Since `model2` is designed such that S_2 moves rigidly, it is logical that this first vibration mode is excited most by the interface forces coming from S_2. The coefficients for S_2 in fig. 7.9d show zero values for index 3 and its interaction with the other modes. This is because this mode describes the rigid body rotation about the z axis and is therefore orthogonal to the applied load. Furthermore it is observed that the first two RBMs and their interaction are dominant. Since this substructure moves rather rigidly under the given load case, the coefficients corresponding to the VMs are relatively small in value.

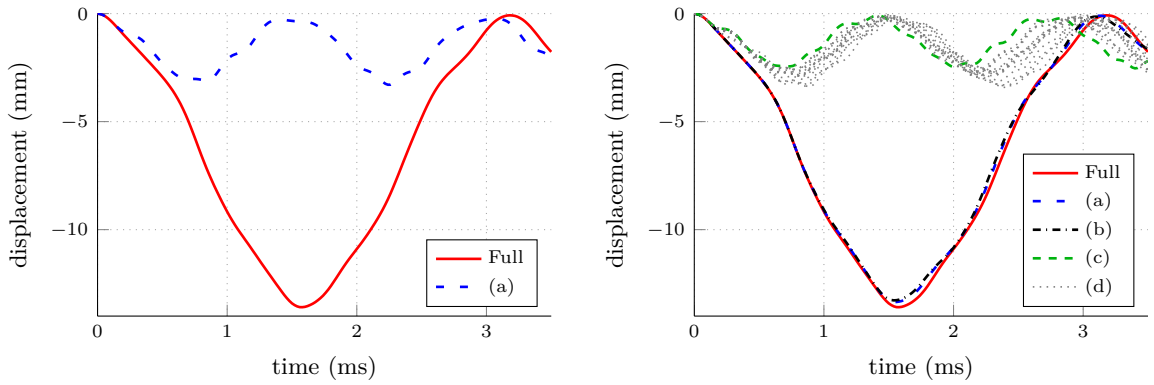

(a) *CB* **(b)** *Rubin*

Figure 7.10: *Nonlinear dynamic responses for a step load on* `model2`*, obtained with nonlinear CB and Rubin reduced models. (a): basis formed with $M = 4$ VMs and all possible modal derivatives, i.e. $R = 10$ for CB and $R = 28$ for Rubin; (b): basis formed with $M = 4$ VMs and an optimal set of $P_1 = 20$ MDs and $P_2 = 3$ MDs; (c): basis formed with vibration modes only, $M = 4, P_1 = P_2 = 0$; (d): basis formed with $M = 4$ VMs and several random choices of P_1 MDs for S_1 and P_2 MDs for S_2.*

Nonlinear response analysis

The reduced nonlinear response obtained with a Craig-Bampton reduction basis of $M = 4$ VMs augmented with all possible $R = 10$ MDs is shown in fig. 7.10a. It is clearly seen that the reduced response is a poor approximation of the fully nonlinear solution. This is due to fact that S_2 undergoes large rotations. These large rotations are described by rigid body derivatives (section 4.4), which are not included in a CB reduction basis. The RBMs in a CB basis are covered by the constraint modes. Due to this observation, this reduction basis will not be investigated any further.

The responses of the Rubin reduced model are shown in fig. 7.10b. When the basis is augmented with all $R = 28$ MDs, the reduced response is in good agreement with the full nonlinear solution; the error is $\varepsilon = 1.9\%$ according to eq. (7.3). An optimal reduction basis is found by truncating the set of MDs, where we denote P_1 and P_2 as the number of MDs in S_1 and S_2 respectively. By including the fewest number of modes without deteriorating the response significantly ($\varepsilon \leq 5\%$), an optimal basis formed by $P_1 = 20$ and $P_2 = 3$ was found. The three modal derivatives included in S_2 are $\boldsymbol{\theta}_{11}$, $\boldsymbol{\theta}_{22}$ and $\boldsymbol{\theta}_{12}$, as shown in fig. 7.9d. Because this component is only undergoing large rotations without deforming a lot, the inclusion of MDs coming from rigid body modes is enough for a good approximation of the full response. Hence, 25 out of 28 MDs are discarded for S_2. Lastly it is noted that fig. 7.10b also shows that the randomly selected reduction bases are not as accurate as the optimal basis selected with the presented mode selection criterion.

The computational savings with the presented nonlinear reduction methods are listed in table 7.2. Note that the Craig-Bampton reduced model is not listed, as the response in fig. 7.10a showed that using this method is not acceptable. It is found that the effect of MOR on the computation times is significant; the Rubin method saved 45% for the basis with all possible $R = 28$ MDs, while the resulting response was found to be in good agreement with the response of the full model. Discarding a total of 32 MDs to obtain the optimal Rubin basis does not

Table 7.2: *Computation times of the different analyses on* `model2`*. The full model is compared to the nonlinear Rubin reduced models; one with all possible MDs in the basis and one with an optimal set of* $P_1 = 20$ *and* $P_2 = 3$ *MDs.*

Analysis	DOFs	time (s)
Full	546	140.7
Rubin ($M = 4, R = 28$)	160	77.4
Rubin ($M = 4, P_1 = 18, P_2 = 3$)	125	74.0

influence the computational effort significantly; the order difference between both reduction bases is too small.

7.1.3 Model 3 analysis

The third model, referred to as `model3`, consists of two thin, flexible substructures. In this design, S_2 will not only undergo large rotations but large deformations as well. This geometry, combined with the applied step load, leads to a fully nonlinear model so Bathe's substructuring technique will be the same as a full nonlinear time integration. Note that this is the case for `model2` as well.

Linear response analysis

First, a suitable linear basis for the CB and Rubin reduction methods needs to be found. It is found that the first $M = 6$ vibration modes accurately describe the linear response for both reduction methods, see fig. 7.11. The reduced linear responses show good agreement with the full linear response. The first $M = 6$ VMs will thus be used to compute the modal derivatives to describe the nonlinear response. For the Rubin method, additional modal derivatives are computed from the three rotational rigid body modes. The total amount of modal derivatives for the CB reduced model is $R = 21$ and for the Rubin reduced model $R = 45$.

Mode selection criterion

The mode selection coefficients b_{ij}, obtained from the linear analyses and with eq. (4.33), are shown in fig. 7.12. For the Craig-Bampton reduction basis of S_1 it is seen in fig. 7.12a that

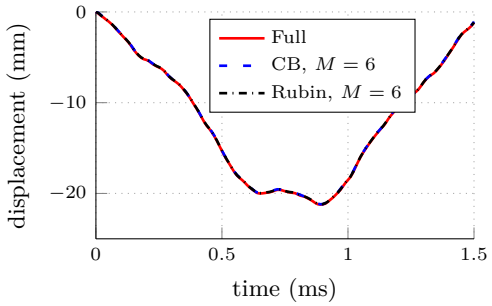

Figure 7.11: *Linear reduced responses of* `model3` *for a step load, computed with both the CB and Rubin method, compared to the full linear solution.*

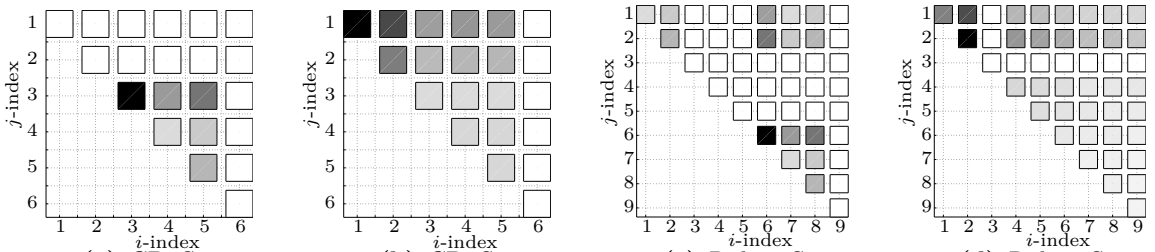

(a) *CB, S_1* **(b)** *CB, S_2* **(c)** *Rubin, S_1* **(d)** *Rubin, S_2*

Figure 7.12: *Mode selection coefficients for* `model3`*, raised to the power of 0.25 to better highlight the relative contribution of the terms. The lower diagonal part of the symmetric b_{ij} coefficients is set to zero for display purposes. Black surfaces indicate high values, white indicates zero. For (c) and (d): indices 1 to 3 indicate rotational RBMs, VM ϕ_i is indicated by index $i + 3$.*

vibration modes 1, 2 and 6 show little participation. For the second substructure, fig. 7.12b reveals that only the sixth VM is not participating in the response. This is, as found for the other models as well, because this mode describes lateral bending motion which is orthogonal to the direction of the applied load.

In fig. 7.12c, the mode selection coefficients for S_1 of the Rubin reduced model show similar behaviour. The modes indicated with 4, 5 and 9 correspond to the first, second and sixth VMs and show little participation to the response. Additionally, the participation of the mode with index 3 and its interaction with the other modes is zero. As found earlier, this mode is the rotational rigid body motion about the z axis and is thus orthogonal to the load as well. For the second substructure, we find in fig. 7.12d that this RBM is again not participating in the response.

Nonlinear response analysis

For the model reduced with Craig-Bampton and enriched with all possible $R = 21$ modal derivatives, the nonlinear response is shown in fig. 7.13a. It is seen that the approximation of reduced response is poor, similar to what was found for `model2`. Again, this is due to the fact that no rigid body derivatives are added to the CB basis. This reduction basis will therefore not be investigated any further.

The approximated responses obtained with the Rubin reduced model are shown in fig. 7.13b. The most accurate case, where all possible $R = 45$ model derivatives are added to the Rubin basis, shows a good agreement with the full response ($\varepsilon = 3.1\%$). An optimal reduction basis is found by truncating the set of MDs until the resulting error surpasses the threshold of 5%. The optimal basis is formed by $P_1 = 24$ and $P_2 = 8$ MDs. Hence 21 and 37 MDs are discarded for S_1 and S_2, respectively. For the bases with randomly selected MDs the same observation as for the other models is done; none of the response approximate the full solution as good as the model with the optimal basis.

The computational efforts for the presented reduction methods, compared to the full nonlinear analysis, are listed in table 7.3. Note that the CB analysis is not listed, as the resulting response is poor. From the table it follows that the computational advantage of the reduction methods is rather small; the Rubin reduction basis augmented with all possible MDs results in a computation time reduction of 10%.

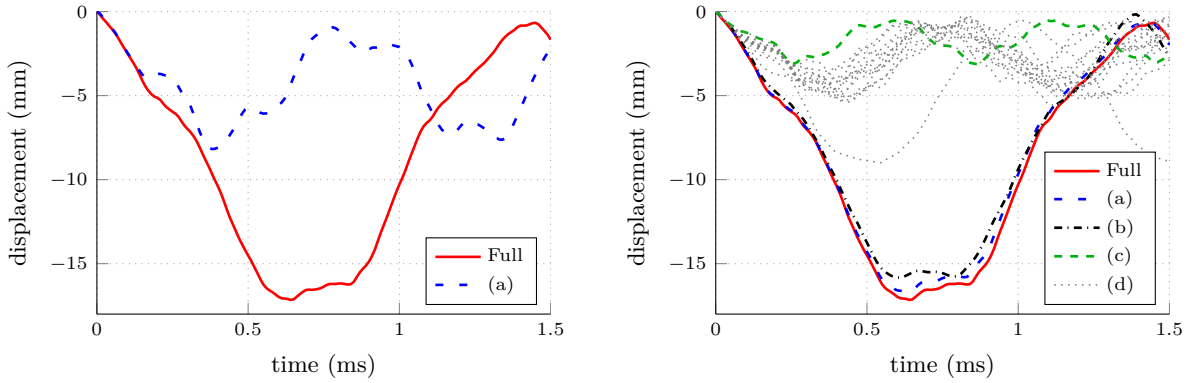

(a) *CB* **(b)** *Rubin*

Figure 7.13: *Nonlinear dynamic responses for a step load case on* `model3`*, obtained with nonlinear CB and Rubin reduced models. The u_z component of the loaded node is shown. (a): basis formed with $M = 6$ VMs and all possible modal derivatives, i.e. $R = 21$ for CB and $R = 45$ for Rubin; (b): basis formed with $M = 6$ VMs and an optimal set of $P_1 = 24$ and $P_2 = 8$ MDs; (c): basis formed with vibration modes only, $M = 6, P_1 = P_2 = 0$; (d): basis formed with $M = 6$ VMs and several random choices of P_1 MDs for S_1 and P_2 MDs for S_2.*

Table 7.3: *Computation times of the different analyses on* `model3`*. The full model is compared to the nonlinear Rubin reduced models; one with all possible MDs in the basis and one with an optimal set of $P = 25$ MDs for S_1 and $P = 10$ MDs for S_2.*

Analysis	DOFs	time (s)
Full	546	84.0
Rubin ($M = 6, R = 45$)	198	56.3
Rubin ($M = 6, P_1 = 25, P_2 = 10$)	143	55.4

7.2 Joined Wing analysis

The Joined Wing (JW) concept is a nonplanar airplane wing structure, as shown in fig. 7.14. It has a diamond shape for both top and front views. JW designs show a horizontal wing that is swept forward and joined with the main wing, forming a strut. The tail is then in compression, reducing the bending moments in the wing. The concept of closed wings was originally proposed by Dr. Julian Wolkovitch [39] and has been subject of aerodynamic, structural and design optimisations studies for 30 years. It is also studied by Boeing as a radar platform and by NASA for application to medium range transporters. Promising aerodynamic and mechanical characteristics, such as lowering drag and lighter weight combined with a higher stiffness, of this non-conventional wing concept could positively influence fuel consumption and manoeuvrability. Because the decrease in fuel consumption is not very high, the financial benefits of JWs are minor for commercial use.

Computer models (FE models) of the Joined Wing concept are inherently nonlinear due to the highly flexible wings. FE simulations of the structure introduces too many DOFs to solve for the nonlinear response within a reasonable amount of time. Therefore, the application of Model Order Reduction in such a model is highly welcomed [13]. Nonlinear MOR on JW

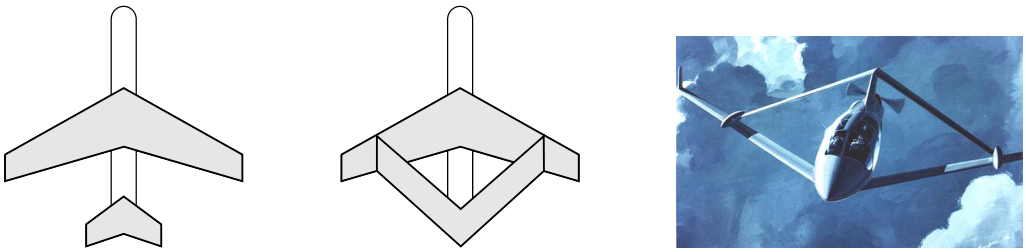

(a) *Conventional wing* **(b)** *JW concept* **(c)** *Artistic impression*

Figure 7.14: *The Joined Wing concept.*

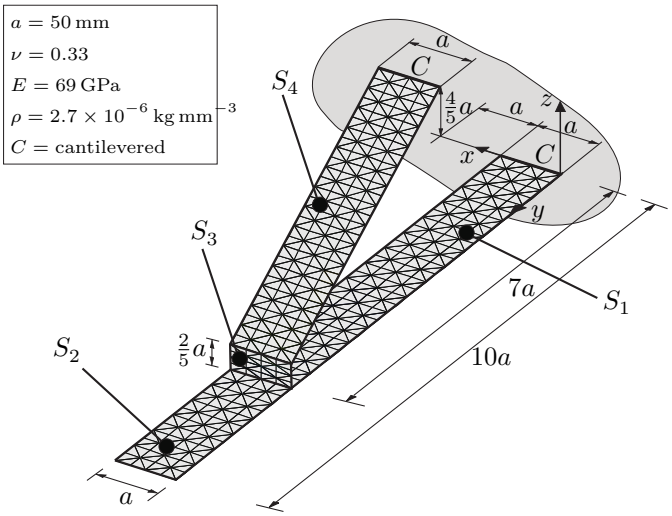

Figure 7.15: *FE model sketch of the Joined Wing structure. Joint (S_3) located at 70% of the wing span.* $h_1 = h_2 = h_3 = 2\,\text{mm}$; $h_4 = 0.5\,\text{mm}$.

models has been studied earlier (e.g. [12, 30]), with promising results. However, substructuring (or CMS) methods have not been applied to the JW concept yet. This will be done in this research.

7.2.1 Joined Wing model description

A simplified FE model, introduced in [13], represents the Joined Wing structure that will be studied in this research. A model sketch is given in fig. 7.15. The model's material properties are the same for all four substructures; with density $\rho = 2.7 \times 10^{-6}\,\text{kg mm}^{-3}$, Young's modulus $E = 69\,\text{GPa}$ and Poisson's ratio $\nu = 0.33$ it is based on aluminium. This model has previously been studied for nonlinear reduced analysis in [13, 30]. The FE model consists of the same triangular shell elements as used in the numerical examples in section 7.1 and described in appendix A. The number of elements and DOFs for each of the four substructures and the assembled model are listed in table 7.4. Note that the sum of the number of boundary DOFs of the individual substructures does not equal the number of boundary DOFs in the assembled model, due to the way of assembly (primal assembly, see section 3.6).

In the original FE model, a uniform pressure of $p = 551.25\,\text{N m}^{-2}$ in the vertical direction

Table 7.4: *Element and node properties of the Joined Wing FE model.*

Substructure	Elements	DOFs	Boundary DOFs	Internal DOFs
1	224	870	60	810
2	96	390	30	360
3	32	150	60	90
4	224	870	60	810
Assembled	576	2190	120	2070

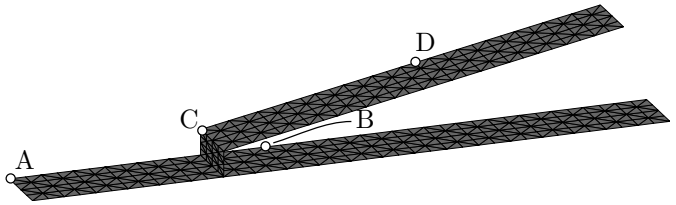

Figure 7.16: *The vertical displacement of the four nodes* $A = (50, 300, 0)$, $B = (50, 500, 0)$, $C = (50, 350, 20)$, *and* $D = (103.57, 162.50, 30.71)$ *is monitored.*

$(+z)$ was applied to the top surfaces of substructures S_1, S_2 and S_4. This static loading corresponds to a dynamic pressure on the wings for a speed of $V_\infty = 30\,\mathrm{m\,s^{-1}}$. For dynamic analyses as done in this research, a pressure load of 5% of the nominal value is applied as a step load. The model is free of any damping. Four nodes are studied to monitor the response, as indicated in fig. 7.16. The response plots will show the u_z components of the indicated nodes. Figure 7.17 shows the significant difference in the dynamic response between a linear and a nonlinear analysis of the full FE model.

As was mentioned earlier, all substructures in the JW model behave geometrically nonlinear. Therefore, Bathe's substructuring time integration scheme will not provide any benefits for this case (see section 5.4). The conventional nonlinear Newmark scheme described in section 5.3 is used for the nonlinear response analyses.

7.2.2 Wing response analysis

For the reduced nonlinear analysis, the underlying linear dynamics of the reduced model should be in good agreement with the full linear model. For both the CB and Rubin method, a linear basis with $M = 8$ VMs per substructure was found to be sufficient to accurately describe the full linear response. From, fig. 7.18, it is seen that the difference between the full and reduced responses is insignificant. For both methods, the error measure in eq. (7.3) gave a value under 0.2%. Based on the number of vibration modes, the Craig-Bampton reduction basis can be augmented with $R = 36$ MDs and the Rubin basis with $R = 66$ MDs.

Nonlinear response analysis

First, the nonlinear response of the full model is compared with the response obtained with a CB reduced model. The results for all considered nodes are shown in fig. 7.19. To indicate the importance of MDs in the reduction basis, the responses where only VMs are included are also shown. For the Rubin reduced model, the same responses are shown in fig. 7.20.

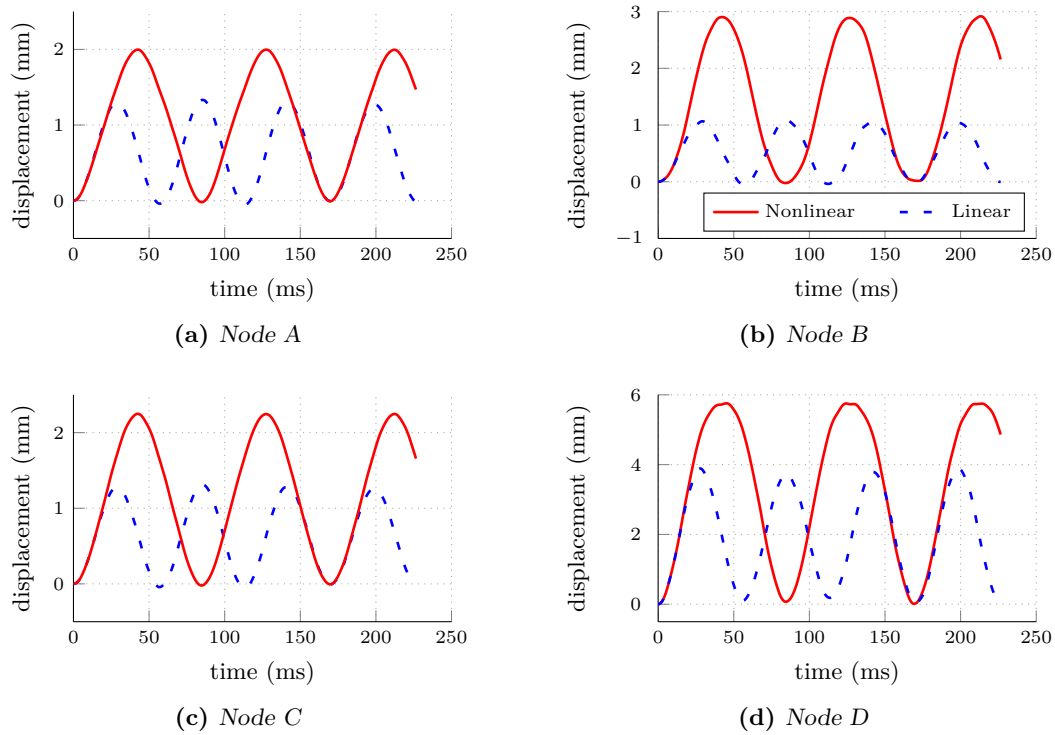

(a) *Node A* **(b)** *Node B*

(c) *Node C* **(d)** *Node D*

Figure 7.17: *Comparison between linear and nonlinear response analysis on the (full) JW model.*

The reduced responses show slightly smaller deflections and shorter periods of vibration. These two observations indicate a higher stiffness for the reduced model. This is expected as a total of 2190 DOFs are approximated by a generalised set of 296 and 440 DOFs for CB and Rubin, respectively. When no MDs are included, the reduced responses are a poor representation of the full response; this indicates the importance of MDs. None of the substructures, under the considered load conditions, undergo large rotations; see the displacement amplitudes in the response plots. Therefore, the nonlinear CB reduction method works for this problem. This was not the case in the last two test models analysed in section 7.1. In fig. 7.21, both the augmented reduction methods (CB and Rubin) are compared directly. It is seen that for all four responses the Craig-Bampton method approaches the full solution better, but the differences are only minor. The CB reduction basis is augmented with 120 constraint modes, together with 8 VMs and 36 MDs per substructure. The CB reduced system therefore has 296 generalised DOFs. The reduction basis for the Rubin method contains 120 residual attachment modes, together with 6 RBMs, 8 VMs and 66 MDs per substructure. This results in a reduced system with 440 generalised DOFs.

Mode selection criterion

Based on the geometry and material properties of the FE model, the engineer should be able to approximate whether or not the contribution of certain MDs will be negligible. The first substructure, S_1, is rather long but clamped on one side and interacting with two other substructures on the other side. Also, it is four times thicker than S_4. Therefore, S_1 is less

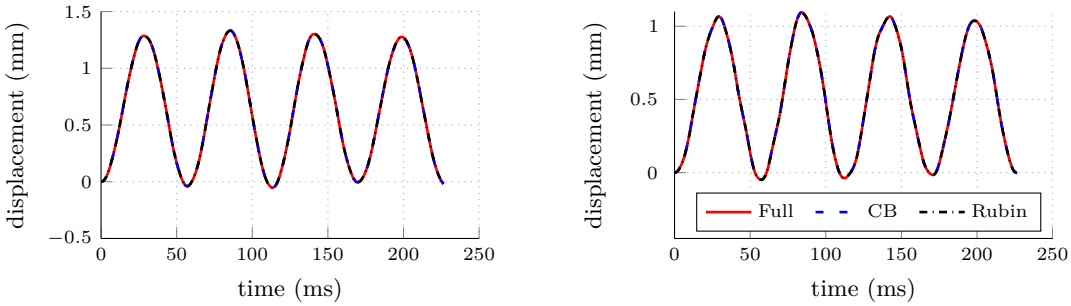

(a) *Node A*

(b) *Node B*

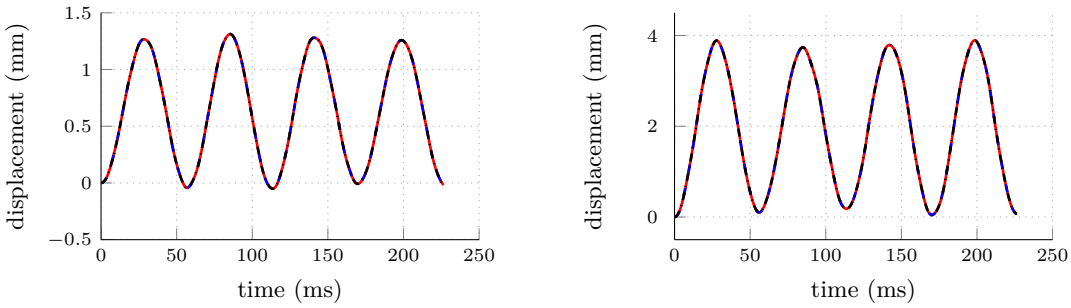

(c) *Node C*

(d) *Node D*

Figure 7.18: *Linear reduced responses of the JW model, computed with the Rubin and CB method, compared to the full linear solution. Both the Rubin and CB reduction bases include $M = 8$ VMs.*

flexible than S_4 but more than S_2 and S_3. The second substructure has intermediate length and a large thickness. However, it is free on one side which improves flexibility. The third substructure acts as a strut between the lower and upper parts of the wing. It relatively large thickness, short length and interaction with substructures on both sides restrict the internal flexibility of this component. It is assumed that S_3 is almost only undergoing rigid body motion. S_4 is the most flexible component, due to its length and small thickness. This component will therefore be deflecting a lot and therefore more MDs are assumed to be needed to describe its motion.

From linear analyses, modal amplitudes are computed and the mode selection coefficients b_{ij} are obtained. For the Craig-Bampton method, the values of b_{ij} are presented in fig. 7.22. For substructures S_2 and S_4 it is seen that the first vibration mode and its interaction with the other modes dominate the response. For S_1, the second vibration mode also shows some significance. The third substructure seems to show dominance of the first four modes. However, this substructure moves rather rigidly during the analysed response time. When comparing the maximum value in fig. 7.24c for S_3 to that of the other three substructures, it is found that it is six orders lower. Although it is not possible to discard MDs based on the presented mode selection criterion, this may indicate that none or only a few MDs are needed to describe the nonlinear response of S_3. With the indications given by the coefficients in fig. 7.22 an optimal basis is form by trial-and-error. The response error is evaluated and a threshold is set at $\varepsilon \leq 10\%$. In fig. 7.23, the resulting responses are compared to the full solution and the reduced solution with all MDs included. For the four substructures respectively, it was found

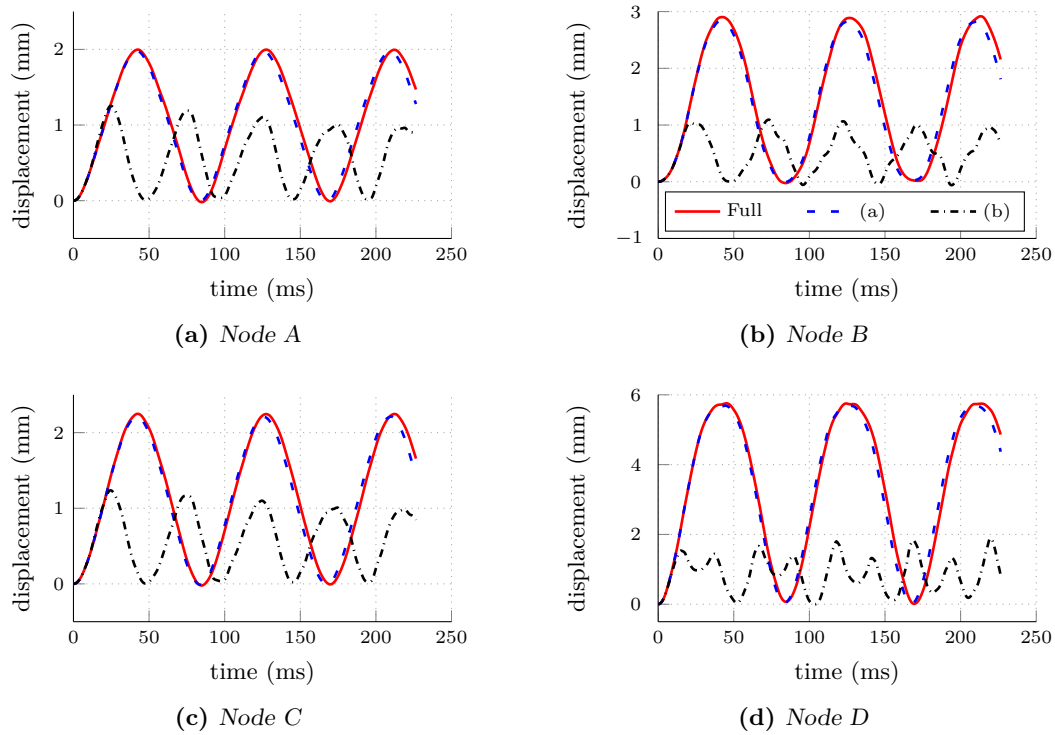

(a) *Node A* **(b)** *Node B*

(c) *Node C* **(d)** *Node D*

Figure 7.19: *Nonlinear dynamic responses on the JW model, obtained with a full model and a nonlinear Craig-Bampton reduced model. (a): basis formed with $M = 8$ VMs and all $R = 36$ modal derivatives for every substructure; (b): basis formed with $M = 8$ VMs only.*

that $P_1 = 13$, $P_2 = 5$, $P_3 = 2$ and $P_4 = 20$. The order of the model with the optimal basis is 192, which was 296 for the reduced model with all MDs included; 104 MDs are discarded.

The mode selection coefficients for the Rubin method are shown in fig. 7.24. The most significant coefficient for all four substructures is b_{11}, i.e. the first rotational rigid body mode (rotation about the x-axis) displaced with its own shape. S_1 and S_4 also show some significant vibration modes, while for the other two substructures the influence of the vibration modes is significantly less than that of the rigid body modes. Vibration mode shapes are important for the first and fourth substructure since these two are the most flexible components of the JW model. Based on the information obtained from the coefficients in fig. 7.24, as many MDs as possible are discarded by means of trial-and-error (again, $\varepsilon \leq 10\%$). It is found that a basis formed with $P_1 = 8$, $P_2 = 5$, $P_3 = 2$ and $P_4 = 48$ satisfies the criterion. This is shown in fig. 7.25. The order of the model is reduced from 440 to 239, by discarding 201 MDs.

Computational savings

The computational efforts of the different time integrations performed on the JW model are compared to find the effect of the presented CMS techniques on a large FE model. The computation times and model orders of the studied JW models are shown in table 7.5. A nonlinear time integration of the non-reduced model took over 2000 s, which is a considerable amount of time (more than 30 min). Reducing the model with Craig-Bampton, augmented with all possible MDs, reduces the order of the model from 2190 to 296 and saves over 1000 s; a

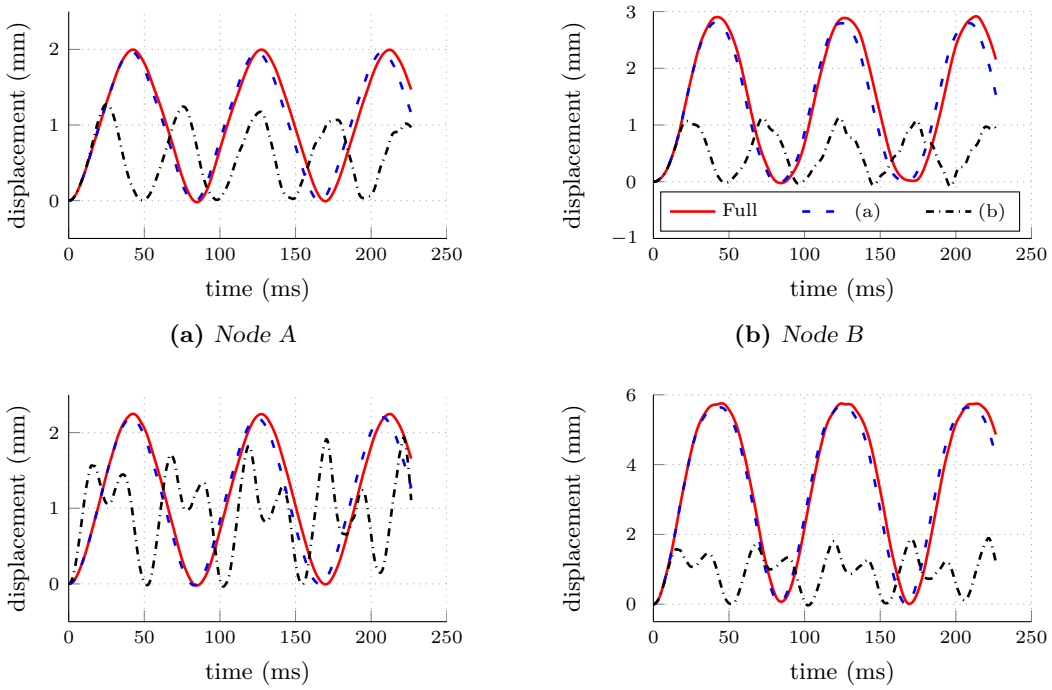

(a) *Node A* **(b)** *Node B*

(c) *Node C* **(d)** *Node D*

Figure 7.20: *Nonlinear dynamic responses on the JW model, obtained with a full model and a nonlinear Rubin reduced model. (a): basis formed with $M = 8$ VMs and all $R = 66$ modal derivatives for every substructure; (b): basis formed with $M = 8$ VMs only.*

Table 7.5: *Computation times of the different analyses on the JW model. The full model is compared to nonlinear Craig-Bampton and Rubin reduced models; one with all possible MDs in the basis and one with an optimal set of MDs.*

Method	Basis	DOFs	time (s)
Full	–	2190	2068.4
CB	$M = 8, R = 36$	296	986.0
CB	$M = 8, P_1 = 13, P_2 = 5, P_3 = 2, P_4 = 20$	192	822.8
Rubin	$M = 8, R = 66$	440	1057.3
Rubin	$M = 8, P_1 = 8, P_2 = 5, P_3 = 2, P_4 = 48$	239	952.2

reduction of 52%. When the number of MDs is further truncated to the optimal set, the model order becomes 192 and the computation time is reduced by 60%. The computational savings for the Rubin method are 48% and 54% when all MDs or an optimal set is included, respectively.

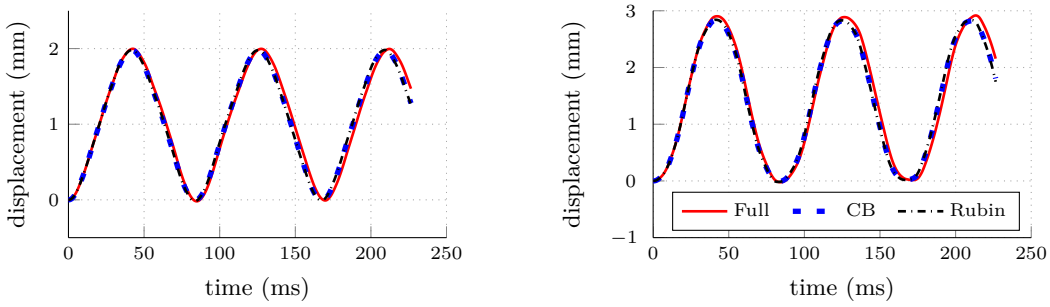

(a) *Node A* **(b)** *Node B*

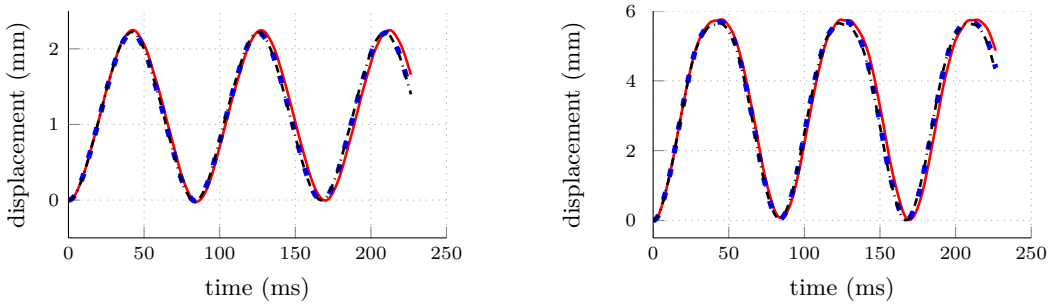

(c) *Node C* **(d)** *Node D*

Figure 7.21: *Nonlinear dynamic responses on the JW model, comparing the augmented Craig-Bampton and Rubin methods to the full solution. The reduced bases are formed with $M = 8$ VMs and all possible modal derivatives, i.e. $R = 36$ for CB and $R = 66$ for Rubin.*

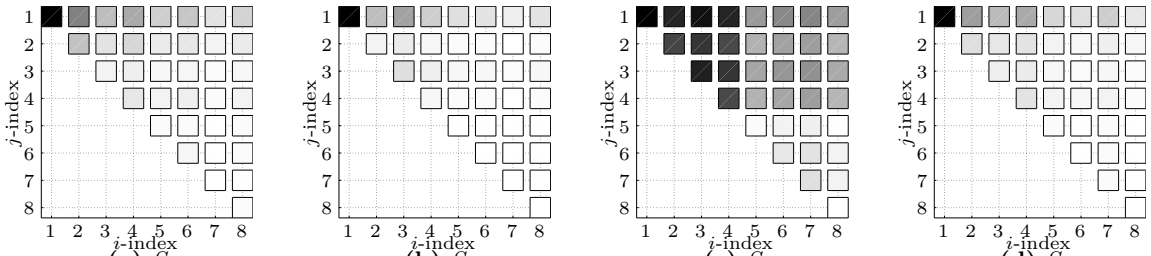

(a) S_1 **(b)** S_2 **(c)** S_3 **(d)** S_4

Figure 7.22: *Mode selection coefficients for the Craig-Bampton reduced JW model, raised to the power of 0.25 to better highlight the relative contribution of the terms. The lower diagonal part of the symmetric b_{ij} coefficients is set to zero for display purposes. Black surfaces indicate high values, white indicates zero.*

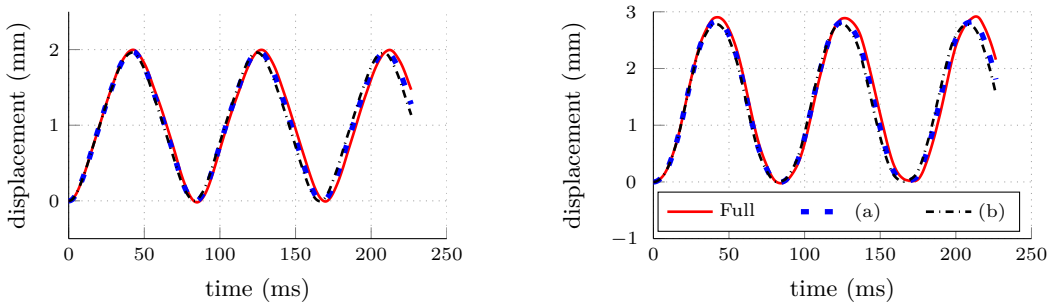

(a) *Node A* **(b)** *Node B*

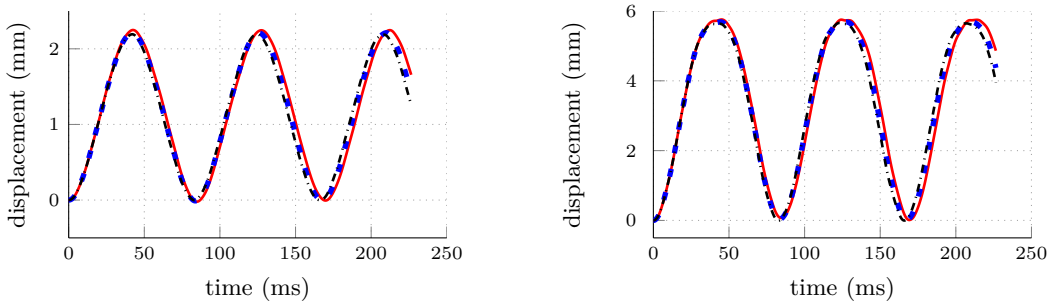

(c) *Node C* **(d)** *Node D*

Figure 7.23: *Nonlinear dynamic responses on the JW model, comparing the full model to two augmented Craig-Bampton models. (a): CB reduction basis with $M = 8$ VMs and all possible MDs. (b): CB reduction basis with $M = 8$ VMs and an optimal set of MDs; $P_1 = 13$, $P_2 = 5$, $P_3 = 2$, $P_4 = 20$.*

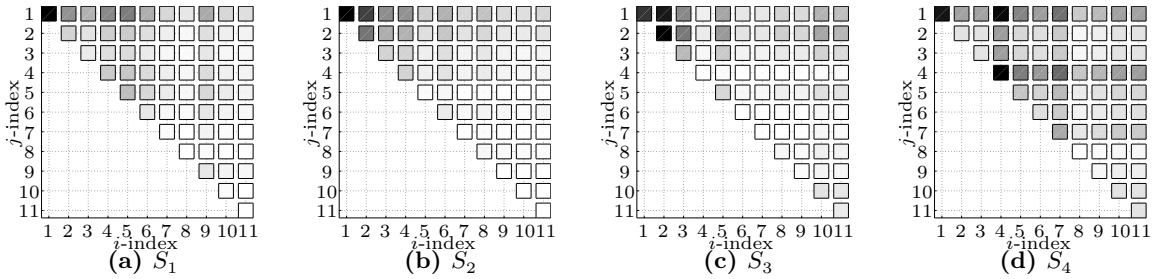

(a) S_1 **(b)** S_2 **(c)** S_3 **(d)** S_4

Figure 7.24: *Mode selection coefficients for the Rubin reduced JW model, raised to the power of 0.25 to better highlight the relative contribution of the terms. The lower diagonal part of the symmetric b_{ij} coefficients is set to zero for display purposes. Black surfaces indicate high values, white indicates zero. Indices 1 to 3 indicate rotational RBMs, VM ϕ_i is indicated by index $i + 3$.*

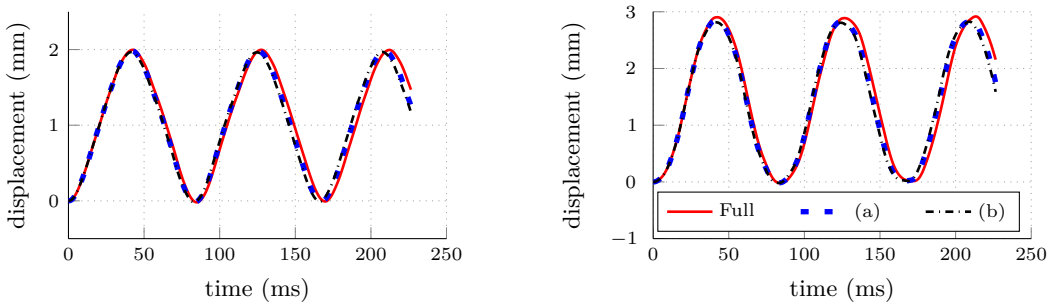

(a) *Node A*

(b) *Node B*

(c) *Node C*

(d) *Node D*

Figure 7.25: *Nonlinear dynamic responses on the JW model, comparing the full model to two augmented Rubin models. (a): Rubin reduction basis with $M = 8$ VMs and all possible MDs. (b): Rubin reduction basis with $M = 8$ VMs and an optimal set of MDs; $P_1 = 8$, $P_2 = 5$, $P_3 = 2$, $P_4 = 48$.*

8 Conclusions and recommendations

8.1 Conclusions

In this work, two Component Mode Synthesis techniques for geometrically nonlinear structural dynamics problems have been developed and tested. The methods are based on the conventional Craig-Bampton and Rubin techniques, which have shown to be effective methods for linear problems. By inclusion of modal derivatives in the reduction basis, the reduced systems are able to capture geometrical nonlinearities up to a certain extend. The number of modal derivatives that can be generated is quadratic with respect to the number of vibration modes in the reduction basis. In order to select an optimal set and keep the reduction basis as small as possible, a mode selection criterion is presented. The methods are tested on three relatively small problems to gain insight in their strengths and weaknesses. Thereafter, the techniques are used on a large FE model of the Joined Wing structure.

Based on the analysed nonlinear responses presented in sections 7.1.1 to 7.1.3, the accuracy and usability of both the Craig-Bampton and Rubin reduction methods augmented with modal derivatives is determined. Comparing the two methods, the first difference that is to be noted is that the (linear) Rubin basis includes rigid body modes. For the same number of *flexible* vibration modes, the Rubin reduction basis is enriched with three translational and three rotational RBMs. Compared to a CB basis of order M, this means that the reduction basis of a Rubin reduced model is $M + 6$. This increase in order is negligible for linear analyses. For nonlinear analyses however, the three rotational RBMs should also be accounted for in the computation of the MDs; these *rigid body derivatives* describe large nonlinear rotations. For a CB basis with M internal vibration modes, $R = M(M+1)/2$ unique MDs can be computed. A similar Rubin basis would include M free vibration modes and 6 rigid body modes. For a Rubin basis of order $M + 6$, a maximum of $R = (M^2 + 7M + 12)/2$ unique MDs can be computed. Hence, for the augmented Rubin method an additional number of $3M + 6$ modal derivatives can be accounted for. For growing linear reduction bases, this number increases rapidly.

From the previous paragraph it may be concluded that an augmented Craig-Bampton basis is preferable. However, as the nonlinear responses of `model2` (fig. 7.10a) and `model3` (fig. 7.13a) show, the CB reduced models approximate the full solution unacceptably poor in certain cases. This is because the substructures S_2 in these models undergo large rigid body rotations. These large rotations cause nonlinearities, which are not described by the nonlinear CB basis. In order to describe these large rotations, modal derivatives of rigid body modes should be taken into account. Unlike Rubin, the rigid body motions in the CB basis are covered by the constraint modes. No modal derivatives for these modes are computed since this could lead to a large and even over-defined modal basis (i.e. more modal DOFs than physical DOFs). This problem is more elaborated in section 8.2.1.

In contrast to the augmented Craig-Bampton method, adding MDs to the Rubin reduction basis proved to be an accurate way to approximate nonlinear responses. For all three considered

Table 8.1: *Overview of the computational savings obtained when using the presented nonlinear CB and Rubin methods on the numerical examples and Joined Wing model.*

	`model1` (step)		`model1` (harm.)		`model2`		`model3`		Joined Wing	
	CB	Rubin	CB	Rubin	CB	Rubin	CB	Rubin	CB	Rubin
all MDs	69%	66%	75%	72%	–	45%	–	33%	52%	48%
optimal set of MDs	–	68%	76%	78%	–	47%	–	34%	60%	54%

models, the Rubin reduced nonlinear responses where the basis was augmented with all possible MDs showed good agreement with the full solution. Rubin approximates the response better than CB due to two main reasons. The first is because MDs of rotational RBMs are taken into account; at the cost of an additional number of $3M + 6$ MDs in the modal basis. For `model2`, where S_2 only undergoes large rotations and hardly deforms, it was found that adding the MDs corresponding to the rotatioanl RBMs only was enough. This is up to the engineers experience. In order to eliminate this human factor, the presented mode selection criterion should be modified such that it is able to predict the number of MDs needed. At this stage, it only indicates which MDs are dominant in the response but the optimal number of MDs still needs to be found by trial and error. The second reason why Rubin shows better performance lies in the nature of the modes that are included in the reduction basis. Both the free vibration modes and their corresponding modal derivatives arise from a free floating problem, i.e. the boundary DOFs are let free instead of fixed as is the case for Craig-Bampton. Therefore, the modal derivatives corresponding to free vibration modes also describe geometrically nonlinear behaviour of the boundaries of the structure.

The computational savings obtained with the presented reduction methods are listed in table 8.1 and vary for the three models between 78% and 33%. A great reduction in computation time is obtained when one or more substructures can be considered linearly (`model1`). Then, by using Bathe's substructuring technique to condense the linear DOFs combined with MOR, the size of the system on which equilibrium iterations are performed is significantly decreased. The difference in savings between a reduced model with all possible MDs in the reduction basis and a model with an truncated optimal set is small. As long as no proper selection criterion and error measure is developed, it is questionable whether the search for an optimal set is worth the extra time this takes.

The methods are also tested on a large FE model, described in section 7.2. As none of the components in this model undergo large rotations, the augmented CB method also works on this model. For a linear basis with $M = 8$ vibration modes and all possible MDs, the CB reduced model showed slightly better results. The differences with the nonlinear Rubin model however are only minor. Finding an optimal basis allowed us to discard 104 MDs from the CB basis and 201 MDs from the Rubin basis. As was concluded in the previous section, it is arguable if it's worth finding an optimal basis with the current mode selection criterion. When using all MDs in the reduction basis, CB and Rubin resulted in computational savings of 52% and 48% respectively. This is a significant amount of computation time, saving more than 15 min for both methods.

It may be concluded that the Rubin method is generally better suitable to be implemented for nonlinear Component Mode Synthesis, due to the more flexible nature of the component modes in the reduction basis. The augmented Rubin method shows good results for all tested

models, whether components undergo nonlinear rotations or not. The nonlinear Craig-Bampton method lacks the information to describe these rotations and is therefore not usable in certain situations. In order to overcome this problem, a suggestion is worked out in section 8.2.1.

8.2 Recommendations

Sections 7.1 and 7.2 showed that using the presented CMS techniques for geometrically nonlinear structural dynamics problems saves a considerable amount of computation time without introducing significant errors. However, there are still many things that need to be studied within the scope of the present work. The following important problems that were found during this research will be discussed next:

1. The Craig-Bampton does not work when one or more substructures undergo large rotations. This problem is found in sections 7.1.2 and 7.1.3. An indication of the weakness of the augmented CB basis has been found and will be elaborated below.

2. The presented mode selection criterion, see section 4.7, only indicates the dominance of modal derivatives relative to each other. It does not indicate how many MDs can be left out of the reduction basis without significant loss of accuracy. An alternative method for finding an optimal reduction basis will be proposed next.

8.2.1 Nonlinear Craig-Bampton in case of large rotations

In contrast to the Rubin reduction basis, rigid body modes are not *explicitly* present in the Craig-Bampton reduction basis. However, these modes may be described by a superposition of the constraint modes. For linear problems, this does not pose a problem. For geometrically nonlinear systems that are analysed using the presented CB method however, no rigid body derivatives can be computed as the RBMs are hidden in the constraint modes. The nonlinear CB basis that was presented in section 4.5 only includes MDs of internal vibration modes. Therefore no information on nonlinearities of the boundary DOFs is stored in the reduction basis.

An attempt to gain insight and solve this weakness is done during this research and will be presented next. In order to overcome the problem that the CB reduction basis does not include rigid body derivatives, rigid body modes are computed geometrically according to section 3.3.3. These modes are not stored in the reduction basis, is this would produce a singular reduced system[1]. Instead, we introduce a matrix $\bar{\mathbf{\Phi}}$:

$$\bar{\mathbf{\Phi}} = \begin{bmatrix} \mathbf{I} & \mathbf{0} & \bar{\mathbf{\Phi}}_{r,b} \\ \mathbf{\Psi}_c & \mathbf{\Phi} & \bar{\mathbf{\Phi}}_{r,i} \end{bmatrix} \tag{8.1}$$

where subscript r indicates rigid body modes and b and i indicate boundary and internal DOFs, respectively. Note that the constraint modes, internal vibration modes and rigid body modes are stored in this matrix. Also, note that the portion of the internal vibration modes corresponding to the boundary DOFs is zero by definition. From this set of mode shapes, modal derivatives can be computed according to eq. (4.13). Because the resulting set does

[1] Rigid body motion is also described by the constraint modes. Including geometrically computed RBMs would lead to linear dependent columns in the reduction matrix.

not only consist of *fixed-interface* MDs, the resulting set of MDs $\bar{\mathbf{\Theta}}$ may have nonzero terms corresponding to boundary DOFs. The CB reduction basis will then have the following form:

$$\begin{bmatrix} \mathbf{u}_b \\ \mathbf{u}_i \end{bmatrix} = \begin{bmatrix} \mathbf{I} & \mathbf{0} & \bar{\mathbf{\Theta}}_b \\ \mathbf{\Psi}_c & \mathbf{\Phi} & \bar{\mathbf{\Theta}}_i \end{bmatrix} \begin{bmatrix} \mathbf{q}_b \\ \boldsymbol{\eta} \\ \boldsymbol{\xi} \end{bmatrix} = \mathbf{R}\mathbf{q} \tag{8.2}$$

This expression states $\mathbf{q}_b \neq \mathbf{u}_b$, so a second coordinate transformation is needed in order to maintain the boundary compatibility condition. From the first row in eq. (8.2), we obtain

$$\mathbf{q}_b = \mathbf{u}_b - \bar{\mathbf{\Theta}}_b \boldsymbol{\xi}. \tag{8.3}$$

This gives us the second coordinate transformation matrix:

$$\begin{bmatrix} \mathbf{q}_b \\ \boldsymbol{\eta} \\ \boldsymbol{\xi} \end{bmatrix} = \begin{bmatrix} \mathbf{I} & \mathbf{0} & \bar{\mathbf{\Theta}}_b \\ \mathbf{0} & \mathbf{I} & \mathbf{0} \\ \mathbf{0} & \mathbf{0} & \mathbf{I} \end{bmatrix} \begin{bmatrix} \mathbf{u}_b \\ \boldsymbol{\eta} \\ \boldsymbol{\xi} \end{bmatrix} = \mathbf{R}_2 \bar{\mathbf{q}} \tag{8.4}$$

Substitution of eq. (8.4) in eq. (8.2) gives an expression in a form desired for CMS methods:

$$\mathbf{u} = \mathbf{R}\mathbf{R}_2\bar{\mathbf{q}} \qquad \Rightarrow \qquad \begin{bmatrix} \mathbf{u}_b \\ \mathbf{u}_i \end{bmatrix} \approx \begin{bmatrix} \mathbf{I} & \mathbf{0} & \mathbf{0} \\ \mathbf{\Psi}_c & \mathbf{\Phi} & \bar{\mathbf{\Theta}}_i - \mathbf{\Psi}_c \bar{\mathbf{\Theta}}_b \end{bmatrix} \begin{bmatrix} \mathbf{u}_b \\ \boldsymbol{\eta} \\ \boldsymbol{\xi} \end{bmatrix} \tag{8.5}$$

The reduction method is implemented in MATLAB and compared to the conventional CB and Rubin methods for `model2` and `model3` (see fig. 7.2). Note that in sections 7.1.2 and 7.1.3 it was found that the CB method did not work for these models, because of the large rotation it undergoes. The results of this comparison are shown in fig. 8.1. It is found that including RBDs only is not enough to describe the nonlinear response. Hence, the limitation of the augmented CB basis is not only the lack of RBDs but also the fact that nonlinear deformations of the boundaries is not described. These nonlinearities can be described by *constraint modal derivatives* (CMDs), i.e. MDs of the constraint modes. Similar to eq. (8.5), CMDs can be included in the reduction basis as well. The results are added to fig. 8.1. Note that not all possible modal derivatives are included in the reduction basis, for reasons that are discussed at the end of this section. For both models, it is found that augmenting the existing nonlinear reduction basis with 100 constraint modal derivatives per substructure is not enough to approximate the full solution as well as the nonlinear Rubin method does. When augmenting the basis with 150 constraint modal derivatives, the full solution is represented exactly. Hence, using CMDs to describe the nonlinear deformations of the boundaries results in a slowly converging reduced model.

A few remarks corresponding to this potential fix of the nonlinear CB method are:

- The number of constraint modes is usually large, leading to a large amount of possible modal derivatives that can be computed. To give an indication, the small numerical examples in section 7.1 contain 42 boundary DOFs per substructure and thus 42 constraint modes. From these modes, 903 MDs can be computed. Computing all MDs introduces two problems. Firstly, the purpose of MOR is to reduce the order of systems such that the number of generalised DOFs is significantly less than the number of physical DOFs. Secondly, when the number of generalised DOFs exceeds the number of physical DOFs, the reduction basis will contain redundant information.

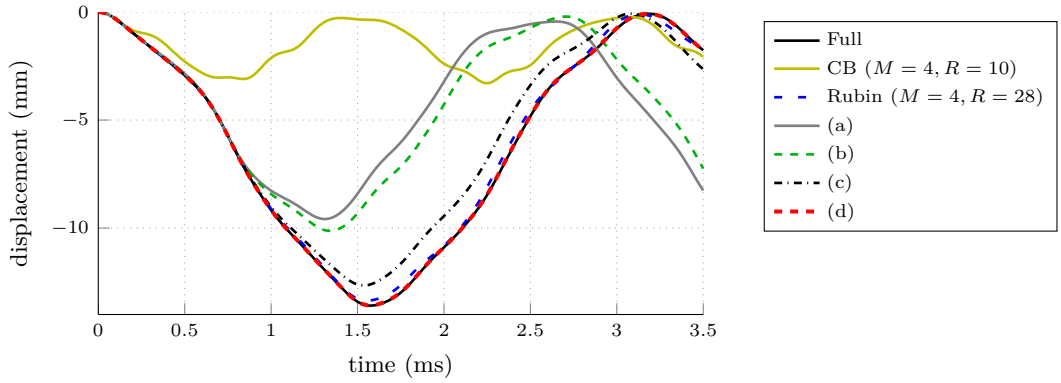

(a) `model2`

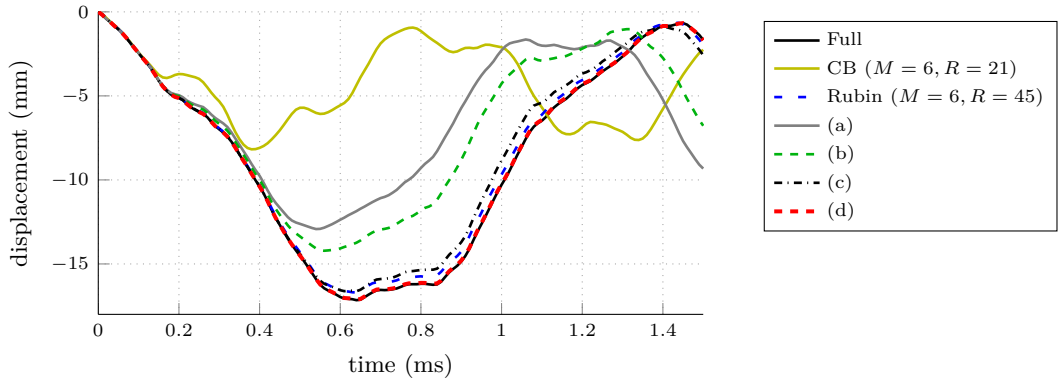

(b) `model3`

Figure 8.1: *Nonlinear dynamic responses for* `model2` *and* `model3`*. The u_z component of the loaded node is shown. The presented nonlinear CB method with constraint modal derivatives is compared to the results of figs. 7.10 and 7.13. (a): basis augmented with rigid body derivatives only; (b): basis augmented with rigid body derivatives and* 20 *constraint modal derivatives; (c): basis augmented with rigid body derivatives and* 100 *constraint modal derivatives; (d): basis augmented with rigid body derivatives and* 150 *constraint modal derivatives.*

- The presented mode selection criterion, see section 4.7, does not work for this technique in case of constrained substructures. If a boundary is clamped, the linear analysis will give zero modal amplitudes for the corresponding boundary DOFs. From eq. (4.33), it then follows that the mode selection coefficients b_{ij} are zero as well. As will be presented next the modal derivatives of constraint modes are required, but the mode selection criterion tells otherwise with the zero coefficients.

- Because all mode selection coefficients for S_1 are zero for the tested models, it is not known if the included constraint modal derivatives are the optimal set.

8.2.2 Mode selection criterion improvements

As long as spatial and spectral convergence is satisfied, discussed in section 4.7.1, it is found in section 7.1 for the numerical examples that the underlying linear dynamics are sufficient to determine the most dominant MDs. Since the mode selection coefficients b_{ij} are computed

from a linear response analysis, it is computationally cheap. However, the mode selection has its weaknesses. The criterion only indicates the relative importance of MDs compared to other MDs within the considered substructure. It is highly desired to develop a criterion that automatically discards modal derivatives that are not contributing significantly to the reduced response.

An optimisation algorithm could be developed to iteratively find an optimal set of MDs. For this purpose, a *greedy algorithm* is suggested here [7]. Let us recall the following approximation of the displacement field:

$$\mathbf{u}(t) \approx \mathbf{R}\mathbf{q}(t) \tag{8.6}$$

If a nonlinear analysis is started with a reduction basis that only includes (linear) vibration modes and the displacement approximation is substituted into the nonlinear equilibrium equations, an error will be introduced as the VMs are not able to describe nonlinear behaviour:

$$\mathbf{M}\mathbf{R}\ddot{\mathbf{q}}(t) + \mathbf{f}\left(\mathbf{R}\mathbf{q}(t)\right) = \mathbf{p}(t) + \mathbf{r}(t) \tag{8.7}$$

where the residual error $\mathbf{r}$ represents the unbalance between the internal and external forces. Note that the residual is a time-dependent vector. If we denote the residual at time step t_i as $\mathbf{r}_i$, we can create the following array:

$$\mathbf{E} = [\mathbf{r}_1, \mathbf{r}_2, \ldots, \mathbf{r}_{n_s}] \tag{8.8}$$

The most dominant residual can be selected from $\mathbf{E}$ by means of singular value decomposition (SVD); $\mathbf{E} = \mathbf{W}\mathbf{\Sigma}\mathbf{V}^T$, where $\mathbf{\Sigma} = \text{diag}(\sigma_1, \ldots, \sigma_r)$, $\sigma_1 > \ldots > \sigma_r > 0$. Since the residual error represents a force, the related displacement field can be computed through the (linear) stiffness matrix. If we denote the most dominant residual as $\mathbf{r}_{\sigma_1}$, we can write

$$\mathbf{u}_{\sigma_1} = \mathbf{K}^{-1}\mathbf{r}_{\sigma_1} \tag{8.9}$$

Next, a basis of MDs could be established that span a space that is as close as possible as the space spanned by the error displacement field $\mathbf{u}_{\sigma_1}$. If this process is performed iteratively (i.e. adding the MDs to $\mathbf{R}$ in eq. (8.6) and solving the new reduced problem in eq. (8.7)) until the residual is below a specified threshold, a optimal basis of MDs can be established. The greedy algorithm is summarised in table 8.2.

Table 8.2: *Greedy algorithm for finding an optimal reduction basis.*

1	Start with linear reduction basis: $\mathbf{u} \approx \mathbf{Rq}$
2	Solve nonlinear reduced problem: $\mathbf{MR\ddot{q}} + \mathbf{f}(\mathbf{Rq}) = \mathbf{p} + \mathbf{r}$
3	If the residual satisfies the convergence criterion, stop. Otherwise continue.
4	Store snapshots of residuals: $\mathbf{E} = [\mathbf{r}_1, \ldots, \mathbf{r}_{n_s}]$
5	Find largest error using SVD: $\mathbf{E} = \mathbf{W\Sigma V}^T$
6	Compute displacements corresponding to largest residual: $\mathbf{u}_{\sigma_1} = \mathbf{K}^{-1}\mathbf{r}_{\sigma_1}$
7	Form basis of MDs that spans $\mathbf{u}_{\sigma_1}$ as good as possible.
8	Update reduction basis $\mathbf{R}$ and got to step 2.

Bibliography

[1] D. J. Allman. "A simple cubic displacement element for plate bending". In: *International Journal for Numerical Methods in Engineering* 10.2 (1976), pp. 263–281.

[2] D. J. Allman. "Evaluation of the constant strain triangle with drilling rotations". In: *International Journal for Numerical Methods in Engineering* 26.12 (1988), pp. 2645–2655.

[3] K.-J. Bathe and S. Gracewski. "On nonlinear dynamic analysis using substructuring and mode superposition". In: *Computers & Structures* 13.5–6 (1981), pp. 699–707.

[4] T. Belytschko, B. Moran, and W. K. Liu. *Nonlinear finite element analysis for continua and structures*. Vol. 1. Wiley, 1999.

[5] P. G. Bergan and C. A. Felippa. "A triangular membrane element with rotational degrees of freedom". In: *Computer Methods in Applied Mechanics and Engineering* 50.1 (July 1985), pp. 25–69.

[6] R. D. Cook et al. *Concepts and applications of finite element analysis*. Fourth. John Wiley and Sons. Inc., 2002.

[7] T. Cormen et al. *Introduction To Algorithms*. MIT Press, 2001. ISBN: 9780262032933.

[8] R. R. Craig and M. C. C. Bampton. "Coupling of substructures for dynamic analysis". In: *AIAA journal* 6.7 (1968), pp. 1313–1319.

[9] R. R. Craig and C.-J. Chang. "A review of substructure coupling methods for dynamic analysis". In: *NASA. Langley Res. Center Advan. in Eng. Sci* 2 (1976).

[10] R. R. Craig and C.-J. Chang. "On the use of attachment modes in substructure coupling for dynamic analysis". In: *18th Structures, Structural Dynamics and Material Conference*. 77-405. AIAA. 1977, pp. 89–99.

[11] R. R. Craig and A. J. Kurdila. *Fundamentals of Structural Dynamics*. Wiley, 2006. ISBN: 9780471430445.

[12] L. Demasi and E. Livne. "The structural order reduction challenge in the case of geometrically nonlinear joined-wing configurations". In: *48th AIAA Structures, Structural Dynamics and Materials Conference, Honolulu, HI*. 2007.

[13] L. Demasi and A. Palacios. "A reduced order nonlinear aeroelastic analysis of joined wings based on the proper orthogonal decomposition". In: *51st AIAA Structures, Structural Dynamics and Materials Conference, Orlando, FL*. 2010.

[14] C. Farhat and M. Géradin. "On the general solution by a direct method of a large-scale singular system of linear equations: application to the analysis of floating structures". In: *International Journal for Numerical Methods in Engineering* 41.4 (1998), pp. 675–696. ISSN: 1097-0207.

[15] C. A. Felippa. *Introduction to Finite Element Methods*. Department of Aerospace Engineering Sciences. University of Colorado at Boulder, 2012.

[16] M. Géradin and D. Rixen. *Mechanical vibrations: theory and application to structural dynamics*. Ed. by 2. Chichester: John Wiley, 1997.

[17] A. Girard and N. Roy. *Structural Dynamics in Industry*. ISTE. Wiley, 2010. ISBN: 9780470393499.

[18] R. Guyan. "Reduction of stiffness and mass matrices". In: *AIAA journal* 3.2 (1965), p. 380.

[19] W. Hurty. "Dynamic analysis of structural systems using component modes". In: *AIAA journal* 3.4 (1965), pp. 678–685.

[20] W. Hurty. “Vibrations of structural systems by component mode synthesis”. In: *Proceedings of the American Society of Civil Engineers* 85.4 (1960), pp. 51–69.

[21] S. R. Idelsohn and A. Cardona. “A load-dependent basis for reduced nonlinear structural dynamics”. In: *Computers & Structures* 20.1–3 (1985), pp. 203–210.

[22] S. R. Idelsohn and A. Cardona. “A reduction method for nonlinear structural dynamic analysis”. In: *Computer Methods in Applied Mechanics and Engineering* 49.3 (June 1985), pp. 253–279.

[23] B. Irons. “Structural eigenvalue problems - elimination of unwanted variables”. In: *AIAA Journal* 3.5 (1965), pp. 961–962.

[24] D. de Klerk, D. J. Rixen, and S. N. Voormeeren. “General framework for dynamic substructuring: history, review and classification of techniques”. In: *AIAA journal* 46.5 (2008), pp. 1169–1181.

[25] A. W. Leissa. *Vibration of plates*. NASA SP. Scientific, Technical Information Division, National Aeronautics, and Space Administration; [for sale by the Supt. of Docs., U.S. Govt. Print. Off.], 1969.

[26] R. MacNeal. “A hybrid method of component mode synthesis”. In: *Computers & Structures* 1.4 (1971), pp. 581–601.

[27] N. M. Newmark. “A Method of Computation for Structural Dynamics”. In: *Proc. ASCE* 85.3 (1959), pp. 67–94.

[28] A. Preumont. *Twelve Lectures on Structural Dynamics*. Universite Libre de Bruxelles. 2012.

[29] Z.-Q. Qu. *Model Order Reduction Techniques: With Applications in Finite Element Analysis*. Springer, 2004. ISBN: 9781852338077.

[30] G. Riahi. “Model Order Reduction for a Nonlinear Finite Element Model of a Joined Wing Structure”. MA thesis. Delft University of Technology, 2012.

[31] D. Rixen. “A dual Craig–Bampton method for dynamic substructuring”. In: *Journal of Computational and applied mathematics* 168.1 (2004), pp. 383–391.

[32] D. Rixen. “Interface Reduction in the Dual Craig-Bampton method based on dual interface modes”. In: *Linking Models and Experiments*. Ed. by T. Proulx. Vol. 2. Conference Proceedings of the Society for Experimental Mechanics Series. Springer New York, 2011, pp. 311–328.

[33] S. Rubin. “Improved component-mode representation for structural dynamic analysis”. In: *AIAA journal* 13.8 (1974).

[34] P. M. A. Slaats, J. de Jongh, and A. A. H. J. Sauren. “Model reduction tools for nonlinear structural dynamics”. In: *Computers & Structures* 54.6 (Mar. 1995), pp. 1155–1171.

[35] P. Tiso. “Finite Element Based Reduction Methods for Static and Dynamic Analysis of Thin-Walled Structures”. PhD thesis. Delft University of Technology, 2006.

[36] P. Tiso. “Optimal second order reduction basis selection for nonlinear transient analysis”. In: *Modal Analysis Topics, Volume 3*. Springer, 2011, pp. 27–39.

[37] P. Van Der Valk. “Model Reduction & Interface Modeling in Dynamic Substructuring”. MA thesis. Delft University of Technology, 2010.

[38] S. Voormeeren. “Dynamic Substructuring Methodologies for Integrated Dynamic Analysis of Wind Turbines”. PhD thesis. Delft University of Technology, 2012.

[39] J. Wolkovitch. “The joined wing-An overview”. In: *Journal of Aircraft* 23.3 (1986), pp. 161–178.

Triangular shell element

A

A.1 General description

Tiso implemented a triangular three-noded shell element in MATLAB [35]. Each node includes six degrees of freedom; three translations and three rotations. The set of degrees of freedom can be divided into a membrane and a bending part, as formulated by Allman in [2] and [1] respectively. This is illustrated in appendix A.1.

The element DOFs are organised as follows:

$$\mathbf{q} = \begin{bmatrix} \mathbf{q}_1 & \mathbf{q}_2 & \mathbf{q}_3 \end{bmatrix}^T \tag{A.1}$$

where

$$\mathbf{q}_i = \begin{bmatrix} u_i & v_i & w_i & \theta_{xi} & \theta_{yi} & \theta_{zi} \end{bmatrix} \qquad i = 1, 2, 3 \tag{A.2}$$

For ease of notation, the following geometric quantities associated to the element vertices are defined:

$$\begin{aligned} x_{ij} &= x_i - x_j \\ y_{ij} &= y_i - y_j \end{aligned} \tag{A.3}$$

The physical, Cartesian coordinates xyz are mapped on a local, isoparameteric coordinate system $\xi_1\xi_2\xi_3$. These can be interpreted as area coordinates. As illustrated in fig. A.2, an arbitrary point P on the element divides the triangle into three smaller triangles with areas A_1, A_2 and A_3. The local coordinates are defined as:

$$\xi_i = \frac{A_i}{A} \qquad i = 1, 2, 3 \tag{A.4}$$

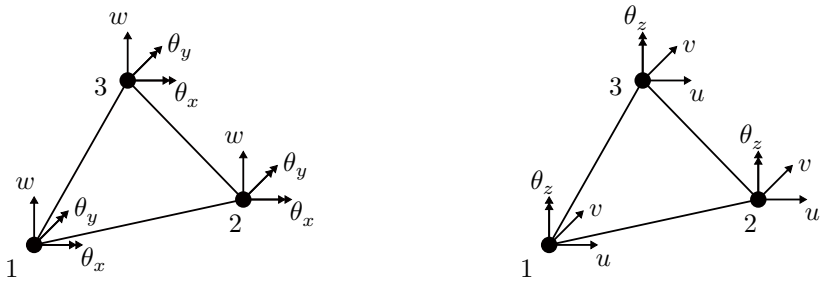

(a) *Bending DOFs* **(b)** *Membrane DOFs*

Figure A.1: *Triangular shell element where bending (out-of-plane) and membrane (in-plane) degrees of freedom are distinguished. Double arrows denote a (drilling) rotation about the depicted axis.*

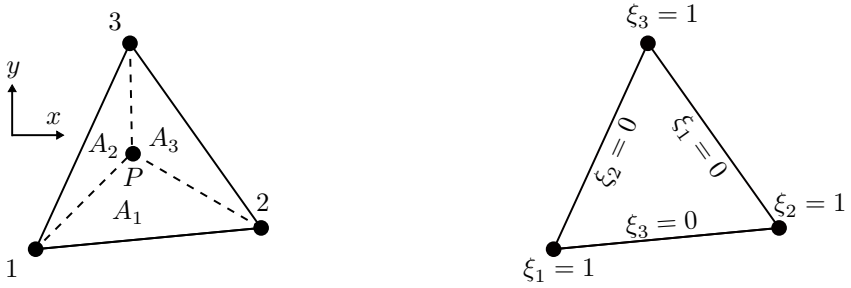

(a) *Area coordinates* **(b)** *Coordinate values*

Figure A.2: *Isoparametric area coordinates $\xi_1\xi_2\xi_3$ in a triangular element*

where A is the total area of the element. Because $A_1 + A_2 + A_3 = A$, the following constraint equation makes coordinates ξ_i dependent:

$$\xi_1 + \xi_2 + \xi_3 = 1 \tag{A.5}$$

Expressing area in terms of Cartesian coordinates gives:

$$\begin{aligned} x &= \xi_1 x_1 + \xi_2 x_2 + \xi_3 x_3 \\ y &= \xi_1 y_1 + \xi_2 y_2 + \xi_3 y_3 \end{aligned} \tag{A.6}$$

From eqs. (A.5) and (A.6) we can write the following matrix form:

$$\begin{bmatrix} 1 \\ x \\ y \end{bmatrix} = \begin{bmatrix} 1 & 1 & 1 \\ x_1 & x_2 & x_3 \\ y_1 & y_2 & y_3 \end{bmatrix} \begin{bmatrix} \xi_1 \\ \xi_2 \\ \xi_3 \end{bmatrix} \tag{A.7}$$

From which the link between the partial derivatives of the two coordinate systems can be deduced [15, Ch.15]:

$$\begin{bmatrix} \frac{\partial}{\partial x} \\ \frac{\partial}{\partial y} \end{bmatrix} = \begin{bmatrix} \mathbf{T}_x \\ \mathbf{T}_y \end{bmatrix} \begin{bmatrix} \frac{\partial}{\partial \xi_1} \\ \frac{\partial}{\partial \xi_2} \end{bmatrix} = \frac{1}{2A} \begin{bmatrix} y_{23} & y_{31} & y_{12} \\ x_{32} & x_{13} & x_{21} \end{bmatrix} \begin{bmatrix} \frac{\partial}{\partial \xi_1} \\ \frac{\partial}{\partial \xi_2} \end{bmatrix} \tag{A.8}$$

where A is the surface area of each element:

$$A = \frac{y_{12}x_{13} - x_{12}y_{13}}{2} \tag{A.9}$$

A.2 Strain matrices formulation

Only the in-plane (membrane) strain components contain quadratic contributions. These strain components are organised as:

$$\boldsymbol{\varepsilon} = \begin{bmatrix} \varepsilon_x & \varepsilon_y & \varepsilon_{xy} \end{bmatrix}^T \tag{A.10}$$

The Green-Lagrange strain relation can be formulated in matrix form as follows:

$$\boldsymbol{\varepsilon} = \mathbf{B}_L \mathbf{q} + \frac{1}{2}\mathbf{B}_{NL}(\mathbf{q})\mathbf{q} \tag{A.11}$$

where $\mathbf{B}_L$ and $\mathbf{B}_{NL} \in \mathbb{R}^{6\times 18}$ denote the linear and nonlinear element strain matrix, respectively. This matrix is defined by Felippa in [5]. The result is given here:

$$\mathbf{B}_L = \begin{bmatrix} \mathbf{B}_{L1} & \mathbf{B}_{L2} & \mathbf{B}_{L3} \end{bmatrix} \tag{A.12}$$

where

$$\mathbf{B}_{L1} = \begin{bmatrix} y_{23} & 0 & & x_{32} \\ 0 & x_{32} & [\mathbf{0}]_{3\times 3} & y_{23} \\ \frac{y_{23}(y_{13}-y_{21})}{6} & \frac{x_{32}(x_{31}-x_{12})}{6} & & \frac{x_{31}y_{13}-x_{12}y_{21}}{3} \end{bmatrix} \tag{A.13}$$

$$\mathbf{B}_{L2} = \begin{bmatrix} y_{31} & 0 & & x_{13} \\ 0 & x_{13} & [\mathbf{0}]_{3\times 3} & y_{31} \\ \frac{y_{31}(y_{21}-y_{32})}{6} & \frac{x_{13}(x_{12}-x_{23})}{6} & & \frac{x_{12}y_{21}-x_{23}y_{32}}{3} \end{bmatrix} \tag{A.14}$$

$$\mathbf{B}_{L3} = \begin{bmatrix} y_{12} & 0 & & x_{13} \\ 0 & x_{13} & [\mathbf{0}]_{3\times 3} & y_{12} \\ \frac{y_{12}(y_{32}-y_{13})}{6} & \frac{x_{21}(x_{23}-x_{31})}{6} & & \frac{x_{23}y_{32}-x_{31}y_{13}}{3} \end{bmatrix} \tag{A.15}$$

In order to form the nonlinear strain matrix, the displacements u, v and w are approximated using linear shape functions:

$$\begin{bmatrix} u \\ v \\ w \end{bmatrix} = \begin{bmatrix} \xi_1 & 0 & 0 & & \xi_2 & 0 & 0 & & \xi_3 & 0 & 0 & \\ 0 & \xi_1 & 0 & [\mathbf{0}]_{3\times 3} & 0 & \xi_2 & 0 & [\mathbf{0}]_{3\times 3} & 0 & \xi_3 & 0 & [\mathbf{0}]_{3\times 3} \\ 0 & 0 & \xi_1 & & 0 & 0 & \xi_2 & & 0 & 0 & \xi_3 & \end{bmatrix} \mathbf{q} \tag{A.16}$$

The nonlinear strain matrix $\mathbf{B}_{NL}$ in eq. (A.11) is equal to

$$\mathbf{B}_{NL} = \begin{bmatrix} \mathbf{q}^T\mathbf{K}_{xx} & \mathbf{q}^T\mathbf{K}_{yy} & \mathbf{q}^T\mathbf{K}_{xy} & \mathbf{0} & \mathbf{0} & \mathbf{0} \end{bmatrix}^T \tag{A.17}$$

where the constant matrices $\mathbf{K}_{xx}$, $\mathbf{K}_{yy}$ and $\mathbf{K}_{xy}$, not to be confused with stiffness matrices, containing derivatives of the interpolation polynomial functions in eq. (A.8) are determined by

$$\begin{aligned} \mathbf{K}_{xx} &= \mathbf{B}_w^T\mathbf{T}_x^T\mathbf{T}_x\mathbf{B}_w + \mathbf{B}_v^T\mathbf{T}_x^T\mathbf{T}_x\mathbf{B}_v \\ \mathbf{K}_{yy} &= \mathbf{B}_w^T\mathbf{T}_y^T\mathbf{T}_y\mathbf{B}_w + \mathbf{B}_u^T\mathbf{T}_x^T\mathbf{T}_x\mathbf{B}_u \\ \mathbf{K}_{xy} &= \mathbf{B}_w^T(\mathbf{T}_x^T\mathbf{T}_y + \mathbf{T}_y^T\mathbf{T}_x)\mathbf{B}_u \end{aligned} \tag{A.18}$$

where $\mathbf{B}_u, \mathbf{B}_v, \mathbf{B}_w \in \mathbb{R}^{3\times 18}$ are boolean matrices linking derivatives in $\mathbf{T}_x$ and $\mathbf{T}_y$ to the correct degrees of freedom. The matrices contain zeros except for the following indices:

$$B_{u(1,1)} = B_{u(2,7)} = B_{u(3,13)} = 1 \tag{A.19}$$

$$B_{v(1,2)} = B_{v(2,8)} = B_{v(3,14)} = 1 \tag{A.20}$$

$$B_{w(1,3)} = B_{w(2,9)} = B_{w(3,15)} = 1 \tag{A.21}$$

The stress-strain relation is based on the assumption of isotropic material:

$$\boldsymbol{\sigma} = \mathbf{H}\boldsymbol{\varepsilon} \tag{A.22}$$

where $\mathbf{H}$ is the linear elastic or Hookean matrix defined as

$$\mathbf{H} = \frac{Eh}{1-\nu^2}\begin{bmatrix} 1 & \nu & 0 \\ \nu & 1 & 0 \\ 0 & 0 & \frac{1-\nu}{2} \end{bmatrix} \tag{A.23}$$

B

Illustration of modal derivatives

In this chapter, illustrations of the second-order modes present in the augmented Craig-Bampton and Rubin bases are shown. Figure B.1 illustrates modal derivatives of the first two internal vibration modes of a rectangular plate. Figure B.2 illustrates the Rubin modes, i.e. modal derivatives of free vibration modes as well as rigid body derivatives, of the same plate.

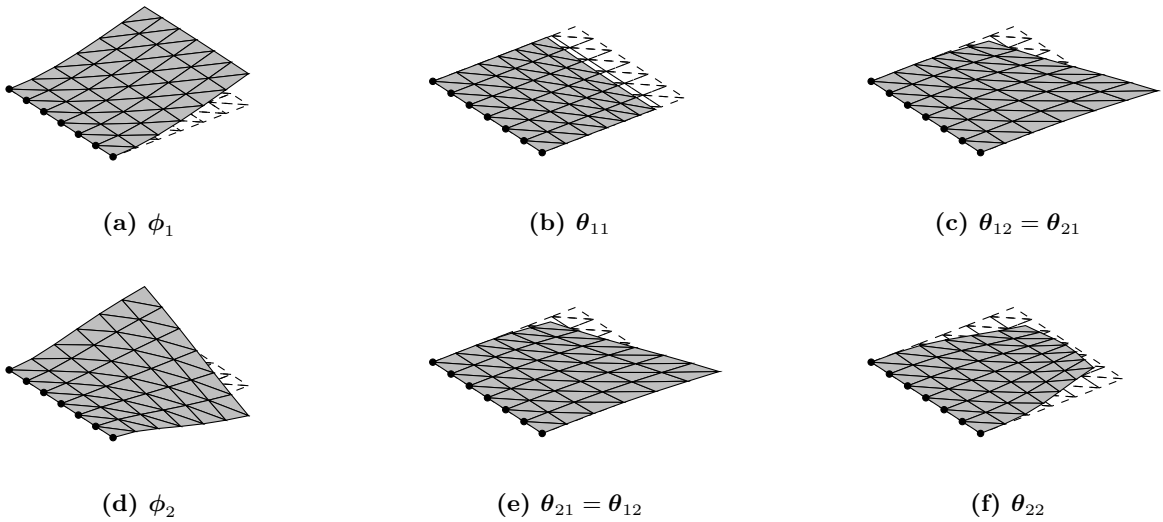

(a) ϕ_1 **(b)** θ_{11} **(c)** $\theta_{12} = \theta_{21}$

(d) ϕ_2 **(e)** $\theta_{21} = \theta_{12}$ **(f)** θ_{22}

Figure B.1: *Dynamic component modes in a Craig-Bampton reduction basis for a square plate model with left edge boundary nodes (black dots). (a,d) First two internal vibration modes; (b,c,e,f) Modal derivatives corresponding to the internal VMs (all in-plane).*

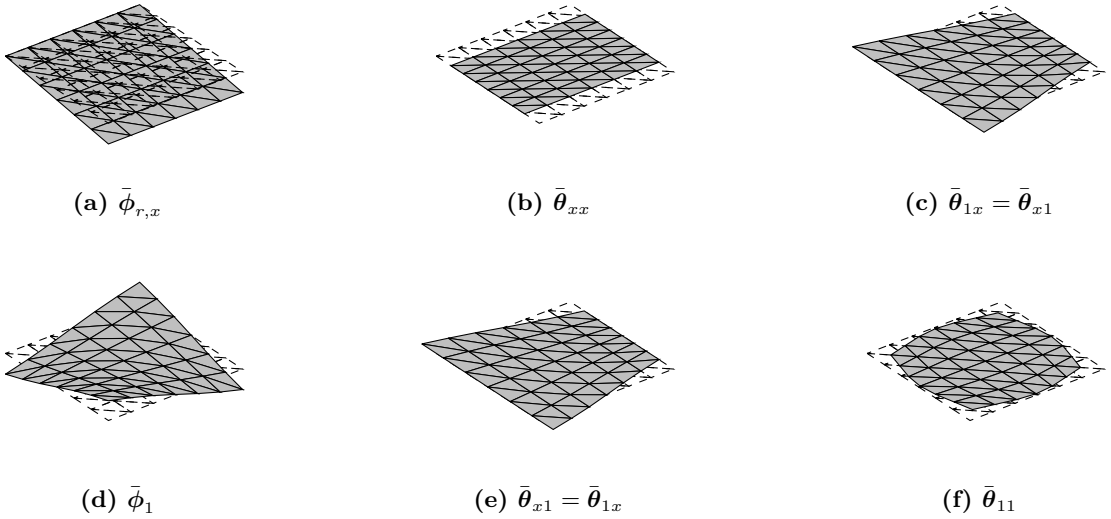

(a) $\bar{\phi}_{r,x}$ **(b)** $\bar{\boldsymbol{\theta}}_{xx}$ **(c)** $\bar{\boldsymbol{\theta}}_{1x} = \bar{\boldsymbol{\theta}}_{x1}$

(d) $\bar{\phi}_1$ **(e)** $\bar{\boldsymbol{\theta}}_{x1} = \bar{\boldsymbol{\theta}}_{1x}$ **(f)** $\bar{\boldsymbol{\theta}}_{11}$

Figure B.2: *Dynamic component modes in a Rubin reduction basis for a square plate model clamped. (a) Rotational rigid body mode about the longitudinal x axis; (d) First free vibration mode; (b,c,e,f) Modal derivatives corresponding to the RBM and free VM (all in-plane).*


TU Delft
Delft
University of
Technology